

**ENDOSCOPIC IMAGING ELASTIC SCATTERING SPECTROSCOPY  
FOR *IN VIVO* DETECTION OF LUNG CANCER**

by

**Erik Herbert Lindsley**

B.S., Computer Science, University Of Kansas, 1994

M.S., Electrical Engineering, University of Kansas, 1997

Submitted to the Graduate Faculty of the

School of Engineering in partial fulfillment

of the requirements for the degree of

Doctor of Philosophy

University of Pittsburgh

2005

UNIVERSITY OF PITTSBURGH  
SCHOOL OF ENGINEERING

This dissertation was presented

by

Erik H. Lindsley

It was defended on

April 1<sup>st</sup> 2004

and approved by

Irving Bigio, Ph.D.

Professor, Departments of Bioengineering, and Electrical and Computer Engineering, Boston  
University

Harvey S. Borovetz, Ph.D.

Professor and Chairman, Department of Bioengineering and  
Professor, Department of Surgery, University of Pittsburgh

Takeo Kanade, Ph.D.

University Professor, School of Computer Science, Carnegie Mellon University, Pittsburgh

George Stetten, M.D., Ph.D.

Associate Professor, Department of Bioengineering, University of Pittsburgh

Elliot Wachman, Ph.D., Chief Scientist, ChromoDynamics, Inc.

Dissertation Director: Daniel L. Farkas, Ph.D.

Vice-Chairman and Professor, Department of Surgery, Cedars-Sinai Medical Center and  
Adjunct Professor, Robotics Institute, School of Computer Science, Carnegie Mellon University

## ABSTRACT

### ENDOSCOPIC IMAGING ELASTIC SCATTERING SPECTROSCOPY FOR *IN VIVO* DETECTION OF LUNG CANCER

Erik Herbert Lindsley, PhD

University of Pittsburgh, 2005

Elastic Scattering Spectroscopy is a promising *in vivo* technique for estimating the size of nuclei in epithelial tissues. Since increased nuclear size is a major morphopathologic sign of tissue progression towards cancer, this technique has been pursued by researchers who demonstrated cancer detection using it in an endoscopic point-test modality. For clear practical reasons related to future clinical use, we proposed and undertook expanding this spectroscopic tool into a true two-dimensional imaging modality. The overall objective of the research presented in this dissertation was to transform a promising spectroscopic test for early cancer detection in epithelial tissues into an *in vivo*/intrasurgical diagnostic imaging method, with lung cancer detection as the first application. The first specific aim was to develop an imaging system conceptually similar to the point-test one, but capable of rapidly acquiring a spectral *image* datacube. This was achieved, using novel hardware, software and optical design; all relevant performance parameters were met or exceeded. The second specific aim was the construction of a mathematical model for image content prediction, parameter evaluation, and optimization. This was also accomplished, and the intermediate (one-dimensional) results are consistent with the literature. The third specific aim was to verify the model against known targets (*in vitro* phantoms). This work was partially successful, and helped identify additional experimental

parameters that needed attention when building the imaging system. The fourth specific aim was use of the newly constructed system with consenting patients, in clinical procedures. In the first of these studies (30 patients), results were inconclusive because of all-negative biopsies, but functionality, operating room compatibility and adoption were demonstrated. In the second study, still ongoing, our imaging system was used to guide biopsies (21 patients), and results are currently being analyzed and compared to histopathology. Finally, since the initial system did not take into account all key parameters revealed during the progress of this dissertation, an improved next-generation system is specifically outlined. Overall, this work underscores the usefulness of advanced engineering in general and optical imaging in particular in constructing a new clinical diagnostic system aimed at early detection of cancer without use of contrast agents.

## TABLE OF CONTENTS

1.0	INTRODUCTION .....	1
2.0	BACKGROUND .....	2
2.1	MOTIVATIONS.....	2
2.2	LUNG CANCER .....	7
2.3	HISTOLOGY OF LUNG CANCERS.....	9
2.4	SPECTRAL APPROACHES.....	17
2.5	DATA ANALYSIS.....	20
2.5.1	Spectral Analysis .....	23
2.5.2	Other types of light-based analysis in biological and medical applications .....	26
2.6	MIE THEORY .....	29
2.6.1	Light (classical optics).....	29
2.6.2	Introduction to Mie Theory for dielectric spheres .....	31
3.0	METHODS .....	39
3.1	HARDWARE DEVELOPMENT.....	39
3.1.1	Custom Fiber.....	43
3.1.2	Design and Implementation .....	44
3.1.3	Imaging Components .....	46
3.1.4	Additional System Components .....	46
3.2	EXPERIMENTAL VALIDATION (MODEL) SYSTEMS .....	47

3.2.1	Cuvette-based Model System Development.....	47
3.2.2	Tissue Phantom Development .....	48
3.2.2.1	Formulation.....	49
3.2.2.2	Verification.....	53
3.3	SIMULATION DEVELOPMENT .....	54
3.3.1	Summary of relevant prior work.....	54
3.3.2	Mie Scattering Calculation Code.....	56
3.3.3	Ray simulation .....	56
3.4	CLINICAL TRIALS.....	57
4.0	RESULTS AND DISCUSSION.....	59
4.1	PARTICLE SUSPENSIONS.....	59
4.1.1	Construction and test setup.....	59
4.1.2	Results.....	60
4.2	BEAD-BASED TISSUE PHANTOMS.....	72
4.2.1	Construction.....	72
4.2.2	Microscopic Imaging of Tissue Phantom to Verify Known Structure .....	73
4.2.3	HSIE Verification .....	73
4.3	SIMULATION OF HSIE.....	83
4.4	CLINICAL WORK.....	92
5.0	SUMMARY AND FUTURE WORK .....	97
5.1	SUMMARY .....	97
5.2	NEXT GENERATION SYSTEM .....	98
5.2.1	Next Generation System Parameters .....	99

5.2.2	New Design #1.....	100
5.2.3	New Design #2.....	102
5.2.4	New Design #3.....	104
APPENDIX A.....		107
CIRCUIT DIAGRAM AND PROTOCOL OF SEQUENCER.....		107
APPENDIX B.....		114
INTERNAL REVIEW BOARD (IRB) DOCUMENT.....		114
APPENDIX C.....		128
MATLAB MIE LIBRARY CODE.....		128
BIBLIOGRAPHY.....		135

## LIST OF TABLES

Table 1: Epithelial Cancer Summary (adapted from Damjanov, 1996) .....	8
Table 2: Some sizes of Major and Minor (mammalian) cell organelles.....	16
Table 3: Cell sizes and non-mamalian organelles.....	17
Table 4: Patient racial and gender breakdown.....	93

## LIST OF FIGURES

Figure 1: Upper respiratory tract.....	10
Figure 2: Lower respiratory tract (from Hole, 1989).....	11
Figure 3: Lung Alveolus (from Hole, 1989).....	12
Figure 4: Bronchial Epithelial Tissue (from Hole, 1989).....	13
Figure 5: “Basic” Types of Epithelial Tissue .....	14
Figure 6: Lung Epithelia, with (A) lumen, (B) epithelial cells, and (C) cilia, (D) connective tissue .....	15
Figure 7: Hemoglobin Absorption Spectra (Adapted from S. Prahl) .....	22
Figure 8: Brightfield image (left) and pixel unmixed (right, pseudo-colored with 5 identified spectral components of interest) .....	26
Figure 9: Sphere optical path .....	31
Figure 10: Example radiation pattern as a function of angle .....	33
Figure 11: Key Mie parameters .....	34
Figure 12: Radiation pattern variation as X changes .....	35
Figure 13: Example Q vs P plot (M=1.33, X increasing) .....	36
Figure 14: Two spheres differing only in diameter (by a factor of two) .....	38
Figure 15: Block diagram of the HSIE .....	40
Figure 16: Hyper-spectral imaging endoscope components.....	42
Figure 17: Fiber tip (left) and camera view (right).....	43
Figure 18: Master Synchronizer, Version 1 .....	45

Figure 19: Master Synchronizer, Version 2.....	45
Figure 20: H&E stain of Lung lumen (left) and phantom diagram (right).....	48
Figure 21: Bottom layer constructed.....	51
Figure 22: Bottom+Top Layer (note the dots on the surface) .....	51
Figure 23: Quality-check slide.....	52
Figure 24: Black, 96-well plate.....	53
Figure 25: Cuvette data acquisition setup.....	60
Figure 26: comparison of H <sub>2</sub> O+beads at two concentrations .....	61
Figure 27: S1 signal for H <sub>2</sub> O+beads at 1:50 dilution.....	62
Figure 28: S2 signal for H <sub>2</sub> O+beads at 1:50 dilution .....	63
Figure 29: S1 signal for H <sub>2</sub> O+beads at 1:100 dilutions.....	63
Figure 30: S2 signal for H <sub>2</sub> O+beads at 1:100 dilutions.....	64
Figure 31: Comparison of beads and either Agarose or H <sub>2</sub> O at 1:100 dilution.....	65
Figure 32: S1 signal for Agarose+beads at 1:100 dilutions.....	66
Figure 33: S2 signal for Agarose+beads at 1:100 dilutions.....	67
Figure 34: S1 signals for tissue phantoms at 1:100 bead dilutions.....	68
Figure 35: New S2 signal for H <sub>2</sub> O+beads at 1:50 dilutions .....	69
Figure 36: New S1 signal for H <sub>2</sub> O+beads at 1:100 dilutions .....	70
Figure 37: New S1 signal for H <sub>2</sub> O+beads at 1:50 dilutions .....	70
Figure 38: New S1 signal for Agarose+beads at 1:100 dilutions .....	71
Figure 39: Microscopic image of the top layer of a 10um-bead phantom (with one “diploid”) ..	72
Figure 40: Side view of a 10um phantom.....	73
Figure 41: Bead layer concentration test grid.....	74

Figure 42: Top (bead) layer titration signals showing White normalized signals vs. Wavelength(nm) .....	74
Figure 43: Comparison of top (bead) layer signals by bead size .....	75
Figure 44: Comparison of top (bead) layer signal deviation of fit .....	76
Figure 45: Bottom layer concentration test grid .....	77
Figure 46: Bottom layer titration signals .....	77
Figure 47: Comparison of signals by bead size .....	78
Figure 48: Comparison of bead signal deviation of fit for a given bottom layer.....	79
Figure 49: "C" test pattern .....	80
Figure 50: Test for Z classification.....	81
Figure 51: Test for X classification .....	81
Figure 52: 2x1 grid classification .....	82
Figure 53: 4x4 classification.....	82
Figure 54: Ideal HSIE view for 1.0 $\mu$ m (intermediate result).....	84
Figure 55: 10 $\mu$ m scatters, with a 10 nm illumination bandwidth and uniform sampling of the spectra .....	85
Figure 56: Wavelength-angle topology for 0.5 $\mu$ m (90-180 degrees) .....	86
Figure 57: Wavelength-angle topology for 1.0 $\mu$ m (90-180 degrees) .....	87
Figure 58: Power and autocorrelation vs. angle.....	88
Figure 59: Signature comparison at 173 degrees.....	89
Figure 60: Model prediction vs. real data comparison .....	90
Figure 61: Dr. Christie and his group using the HSIE in the operating room .....	92
Figure 62: Same bronchoscopic biopsy-derived tissue sample imaged in three modes (Hematoxylin-eosin stained pathology slide, imaged directly in transmitted light; Hyper-	

spectral segmentation/classification of the same slide, based on a microscopically acquired image cube and auto-fluorescence image of the same area, excited at 390nm and detected at 430.....	96
Figure 63: New Fiber design #1.....	101
Figure 64: New Fiber design #2.....	103
Figure 65: New fiber/endoscope design #3 .....	104
Figure 66: Bench-to-bedside translational continuum.....	106

## 1.0 INTRODUCTION

The detection, especially non-invasively, of cancer is a very ambitious goal - if it were easy, the decades of research already spent on it by numerous, dedicated scientists would have achieved more than partial success by now. Over the years, cancer has been studied at many levels: biologists have learned the telltale molecular/biochemical signs for various types of cancer; pathologists learned to recognize it at the tissue structural level; physicists and radiologists learned to locate more advanced stages of it using CT, X-rays, MRI, and PET scanners. Physicians learned to recognize physiological symptoms of a body suffering from advanced cancer. Each of these techniques identifies and attacks cancer at a given organization level and size scale (Molecular, Cellular, Tissue, , Organ, and Organism/Patient), yet almost none of them try to explicitly bridge any two or more of these scales. This dissertation is aimed at advancing this bridging idea by using light to discern microscopic properties (pathology) of bulk tissue *in vivo*/intraoperatively. The emphasis is on the theoretical, technological and application advances needed to image cancer early, non-invasively, and using no contrast agents. As the first foray into this approach, we focus specifically on early detection of lung cancer.

## 2.0 BACKGROUND

Cancer has just overtaken heart disease as the leading cause of death in the United States. Half of all men and one-third of all women in the U.S. will develop cancer during their lifetimes ([www.cancer.org](http://www.cancer.org)), and it is estimated that in 2005 cancer will kill 570,280 Americans -- more than 1,500 a day. Even if a fast, painless, and complete cure were found tomorrow, early detection would still be essential to treatment. Current methods revolve around inspection of biopsied tissues by a trained pathologist in a lab, not in the operating room or at the bedside (LaCroix *et al.*). Recent investigations into the application of optical imaging of tissue have focused around the so-called “optical biopsy,” which is a bit of a misnomer since the intent is not to remove tissue but to gain as much information as possible without actually performing tissue removal biopsy. In a more practical sense, compared to traditional biopsies, which only sample a few select areas, optical biopsies allow one to non-destructively “sample” much (if not all) of the surface layers in the tissue of interest. Additionally, an optical biopsy does not preclude the use of a more traditional biopsy—in fact, it can be used to guide this.

## 2.1 MOTIVATIONS

The “gold standard” for the diagnosis of cancer for many years has been the removal of suspicious tissue that is in turn analyzed by a trained pathologist, who then ranks the cancer

based on a variety of histological features and informs the physician, who then recommends any further treatment to the patient. There are several aspects to this “standard” that are undesirable, for a variety of reasons. For example, the site of the traditional biopsy is a single restricted area. A small cancerous lesion could lie 2mm away from the biopsy site and may in fact not be discovered for a long time. Selection of the site is often based on visible changes, and these changes often occur only after the cancer has reached a sizeable foothold in the body. In some cases, visual indicators are the only signs of possible cancer, and thus are not in themselves definitive. In these situations, with extremely aggressive cancers it is not unusual to prescribe preventive, “prophylactic” removal of the entire area despite the fact that there is a reasonable chance that such a procedure is unnecessary. Another undesirable aspect is that a piece of tissue must be removed to be analyzed—something one cannot do too often without destroying the surrounding tissue. This fact limits how often and for what medical reasons the procedure is performed.

Focusing on the results themselves, the analysis that the pathologist performs is time-consuming, often done at a remote location, and involves toxic chemicals. Furthermore, there is a disturbing lack of consistency of analytical results among pathologists (interobserver variations), and even between the same pathologist’s calls at different times (intraobserver variations). In the pursuit of a better quality of care, it would be desirable to improve upon the current “gold standard” to make it more objective and accurate in determining a given patient’s risk, in a timely fashion. The issues raised above can be grouped into four distinct areas that need improvement:

- *In Vitro* (in the lab)

- Microscopic

Improvements in this group are either indirect aids to the pathologist (such as automatic staining and specimen preparation machines), or direct aids to the pathologist (such as automated analysis software).

- Macroscopic

Using surgically removed tissue, automated systems using a variety of mechanisms try to localize suspicious areas for subsequent microscopic evaluation. Usually, the methods employed are optical in nature, as other approaches rarely have the spatial resolution of optical techniques.

- *In vivo* (in animals in preclinical models, and in the patient in clinical applications)

Moving the site of analysis to the patient can radically reduce the round-trip time for getting the desired results. This may also allow the physician to do more exploratory types of examinations or surgery or even guide the physician to suspicious areas which can then be more closely examined, biopsied and, ultimately, treated.

This dissertation focuses on elastic scattering spectroscopy (ESS). It proposes to transform ESS, showing promising results *in vitro* and *in vivo*, when utilized as a point-test diagnostic modality (references), into a true diagnostic *imaging* modality. The use of this technique in an imaging modality is quite relevant to modern medicine, but, to my knowledge, has not been previously used for clinical purposes. In the case of lung cancer, the current standard-of-care calls for follow-up endoscopic procedures to check for a recurrence of the cancer after treatment. A device which aids the surgeon in his exploration of a patient's lungs would be of great assistance

in advancing the standard-of-care. It even opens up the possibility that if the cancer recurrence is caught at a very early stage, a trivial lumpectomy could be performed through the endoscope, thus potentially saving the patient the pain and suffering associated with further cancer treatments such as chemotherapy.

While *in vitro* work is essential, fundamental research, all too often it fails to make the transition to *in vivo*. Moving from one to another entails many challenges:

- Active biological processes that confound detection
  - Blood perfusion
  - Blood intrinsic
  - Normal cell division
  - Scarring
  - Cellular repair mechanisms
  - Tissue trauma
- Light-matter interaction effects
  - Chromophore exhaustion (bleaching)
  - Mass-transport limits (quenching)
  - Scattering of photons in highly turbid media (regardless of source)
  - Reactions with other biological molecules present in the cell
- Toxicology
  - Energy exposure limits (“cooking” the cells)
  - Contrast enhancer or other chemical marker toxicity limits (cells will only tolerate so much of a given chemical before normal cellular processes are disrupted)

- Long-term degradation or removal of any materials introduced into the cells (in some instances, the contrast agents have undesirable, long-term reactions with the cell processes).
- Speed of data acquisition
  - Faster acquisition can minimize motion artifacts (since target is no longer fixed in place)
  - There is a limit to human patience (few people will wait minutes while the system collects data)
  - System noise (increases as speed increases)

Additionally, there are a few challenges associated with simply moving from the laboratory to an operating room with real patients:

- General engineering challenges
  - Device portability
  - Device resistance to normal “wear and tear”
  - Operating room regulations regarding aspects of the device (electrical isolation, kill switches, etc.)
  - Resistance to chemicals normally found in an operating room environment
  - Cleaning/Sterilization (device must be able to be sterilized between patients)
- Analysis of the data (detection process)
  - Timeliness of results (data processing must be prompt, or even real-time if possible)
  - Intuitive representation of results for non-scientists (physicians are not comfortable making a diagnosis from just a sheet of numbers)

- Integration with existing medical practices
  - General resistance to change (new technique must yield more data or clearly better results than the old technique; simply because it is faster and cheaper will not mean quick acceptance)
  - Flexibility in deployment and usage (left versus right handedness, etc.)
  - Physician psychology
  - Internal Review Board approvals
  - Honoring patient privacy issues

Many of these challenges were addressed by the work described in this dissertation, most were surmounted, but a few proved to be too resilient (see below). For a couple of these challenges, no contrast enhancers were used in order to avoid the associated toxicology challenges.

## **2.2 LUNG CANCER**

For many years lung cancer has been, and continues to be, the most common fatal cancer in men and women in the United States and the rest of the world. One reason is due in large part to the prevalence of smoking in our societies, but this is by no means the sole reason. Lung cancer has many varieties, and their peculiarities will affect several aspects of this research. The areas from which primary lung cancer can arise are the epithelia, the soft tissues (parenchyma), and the pleura. Benign tumors are rare in lungs, and there is also the possibility that another cancer in the body can metastasize to the lung, but the frequency of both these types is relatively low when compared to the primary cancers. Cancers usually peak in the age range of 50-70 years, but

rarely occur at an age earlier than 40 years. There are a few that strike children, but these are special cases and are not the same cancers that strike adults. Most malignant tumors of the lung are called “bronchogenic carcinomas” because they originate in the bronchi, which is the part of the lung that occurs earliest in the branching pattern of airways. Bronchi are usually larger than 2mm, but in practice few endoscopes can penetrate far enough into the lung to reach the end of the bronchi (this is true for HSIE, described later in this dissertation). Since the vast majority of the lung cancers of interest here are bronchogenic carcinomas of the epithelial type, discussing the subtypes of epithelial cancers in more detail will be useful.

**Table 1: Epithelial Cancer Summary (adapted from Damjanov, 1996)**

Subtype	Freq. (%)	Central Loc. (%)	Cell				Macro-Visible
			Nucleus (µm)	Volume	Scatt.	Density	
Adenocarcinoma	30	<10	4-7	Unch.	Unch.	Unch.	Varies
Adenosquamous	1-3	<10	4-7	Unch.	Unch.	Decr.	Varies
Carcinoids (child)	<1	80	4-7	Unch.	Incr.	Incr.	Yes
Large Cell (Undiff)	7-15	50	~12	Incr.	Decr.	Unch.	Low
Small Cell	15-20	>99	10-12	Unch.	Incr.	Incr.	High
Squamous cell	20-35	66	4-7	Unch.	Unch.	Decr.	Varies

The above table summarizes the following: subtype, its frequency among epithelial cancers, the chance that it will occur in the central part of the lung as opposed to the periphery, expected cell nucleus size, changes in the cell volume caused by the cancer, changes in the optical scattering of the cell, changes in the cell/collagen density, and whether the tumor causes macroscopic changes clearly visible to the naked eye. Combining all the above statistical information, it is worth noting that only about 22-35% of the lung epithelial cancers result in a dysplastic (enlarged) nucleus. Furthermore, the most frequent cancer (Squamous cell) is distinctive only in that it

forms keratinized cell groups (cells surrounded by excessive amounts of collagen, with subsequent reduction in the numbers of cells per volume of collagen). Macroscopically, keratinization is almost indistinguishable from scar tissue. It is also worth noting that modern endoscopes have trouble accessing more than about 10 branches into the lung by going in through the throat (or trachea). Thus, this research is inherently limited to cancers occurring in the central lung and hence is most applicable to large cell, small cell, squamous cell, and the rare carcinoid subtypes.

### **2.3 HISTOLOGY OF LUNG CANCERS**

The human body can be investigated at various levels of complexity and size: Molecules, Organelles, Cells, Tissues, Organs, and Systems. For properly framing our research, it is important to outline the anatomy and physiology of the lung. It is part of the cardio-pulmonary System, and is an Organ made up of the four basic types of Tissues:

- **Connective:** Underlies or surrounds other tissue, and normally has a role in structurally supporting other tissues. This tissue can have occasional cells trapped within it (e.g. migrating immune cells or matrix-building cells), but is normally dominated by a non-cellular protein (collagen/elastin bundles) or mineral (ossified bone) matrix.
- **Epithelial:** covers the body surface (skin/digestive tract, etc.), and lines all cavities inside the body (ducts, blood vessels, outer surface of organs)
- **Muscle:** Contractile cells responsible for all types of movement in the body (locomotion, prehension, blood and air flow regulation, etc.)

- Neural: Receives, processes, and transmits information to control the various activities of the body (at all organization levels)

The human lung is comprised of each of these four types of tissue in varying amounts, but given that our work is limited to areas that can be accessed by an endoscope, only the Epithelial tissue will constitute our focus; since most lung cancers arise from the lung epithelial tissue, this is certainly not too great of a limitation.

### **Systems and Organs**

The pulmonary system is comprised of the upper and lower respiratory tract. The upper respiratory tract (Figure 1) includes the nose (which cleans the breathed air, warms and moistens it, and filters large dust particles), the mouth (which only cleans and moistens the air), the pharynx (junction of the nose and mouth), and the larynx (which houses the vocal cords).

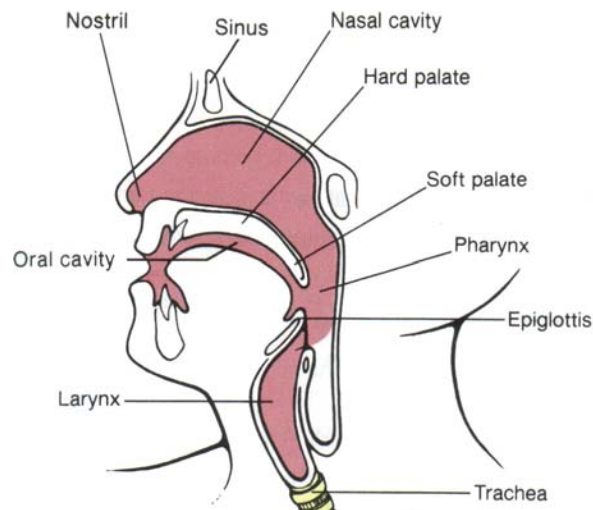


**Figure 1: Upper respiratory tract\***

---

\* Taken from “Essentials of Human Anatomy and Physiology, 3<sup>rd</sup> ed”, by John Hole, copyright 1989 William C. Brown Publishers. Reproduced with permission of The McGraw-Hill Companies.

The lower respiratory tract (Figure 2) includes the trachea (which connects the larynx to the bronchi), the tree-like network of bronchi, and the alveoli (at the ends of the bronchi, where the actual gas exchange between the blood and the air occurs – see below).

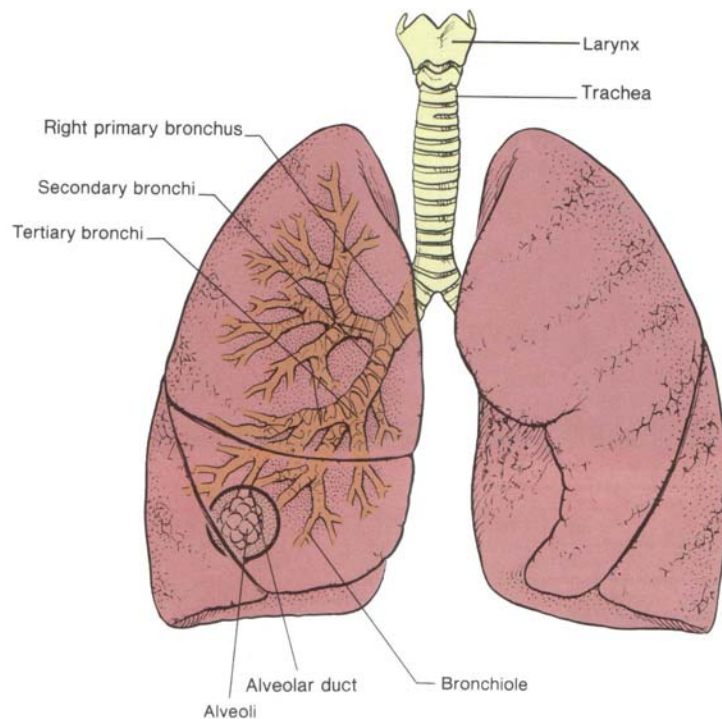


**Figure 2: Lower respiratory tract (from Hole, 1989)**

The lung is filled with a network of passageways, ever decreasing in size, that carry outside air to a blood-gas exchange structure known as an alveolus (Figure 3). The larger passageways are called “bronchi” (“bronchus” being the singular form), and the smaller ones are called “bronchioles”. There are two main lobes of the lung commonly referred to as the “right lung” and the “left lung”, though some people have one of the lobes divided into two smaller lobes (with an extra secondary bronchi to connect them). Not shown in Figure 2 are the ribs, and the pleural cavity between the lung lobes and the ribs. Each of the lung lobes is surrounded by a membrane (the visceral pleura) that forms one side of the pleural cavity. The other side is formed

by a second membrane (the parietal pleura) that is connected (indirectly) to the ribs that form the thoracic cavity that the entire lung (as an organ) resides in. Each of these membranes secretes a fluid that, through surface tension, causes them to stick together but still be able to slide back and forth as needed. This arrangement allows for the fine structures of the lung to be dynamically supported by the ribs and other thoracic structures as it expands and contracts during normal breathing.

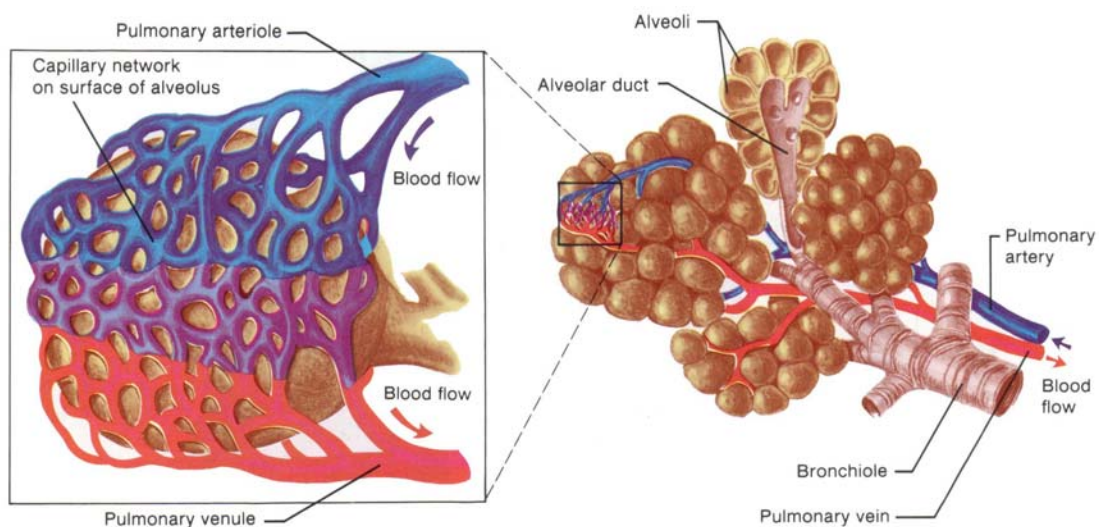


**Figure 3: Lung Alveolus (from Hole, 1989)**

These passageways of the bronchi and alveoli are completely lined with epithelial tissue. However, the bronchial epithelial tissue (mostly) has small hairs (or cilia), while the epithelia in the alveolus do not. One of the jobs of the epithelia in the alveolus is to secrete a mixture of lipoproteins that disrupt the surface tension of water so that the alveolus doesn't collapse (and stick together like the membranes of the pleural cavity do). In the case of the bronchial epithelial tissue, some the cells (called "goblet cells") produce the mucus (or phlegm) in large amounts, as shown in Figure 4.

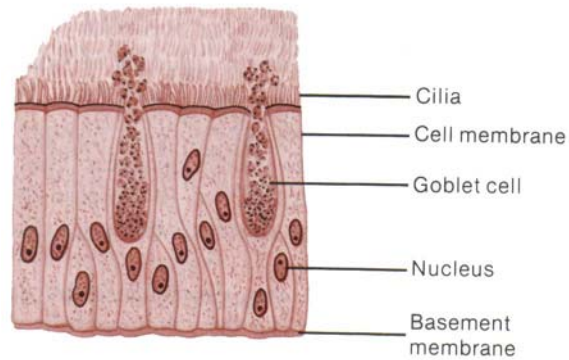


**Figure 4: Bronchial Epithelial Tissue (from Hole, 1989)**

In this figure, the “basement membrane” is where the cells connect to the underlying support tissues, and the cilia are exposed to the air. The cells shown here are two subtypes of “columnar epithelial cells”, which will be explained in greater detail in the following paragraphs.

### **Tissue (Epithelial)**

*In vivo*, cells are normally found in the company of other cells. While there are many different types of tissues in the human body, this thesis will be focusing on epithelial tissue. Epithelial tissue is found throughout the body, usually where there is a need to isolate one part of the body from either another tissue for biological reasons (excretory ducts), or from the outside world (skin, lung, intestine, etc). Simple epithelial tissue consists of one or more layers of epithelial cells, backed by connective tissues that provide structural integrity and a blood supply. Epithelial tissue may have more than one layer of epithelial cells, such as in the skin or the urinary bladder. In this multi-layer (“stratified”) case (rarely more than 7 layers), the epithelial cells undergo a maturation process by which the young cells push the older cells away from the connective tissues. “Stratified” epithelial cells have the capacity to maintain the isolation despite a large amount of stretching or distension, and so are commonly found in parts of the body such as the

urinary tract. Based on their shape, epithelial cells (and, by extension, the tissue) are classified as squamous (flat), cuboidal (cube-shaped), or columnar (cylindrical), as shown in Figure 5.

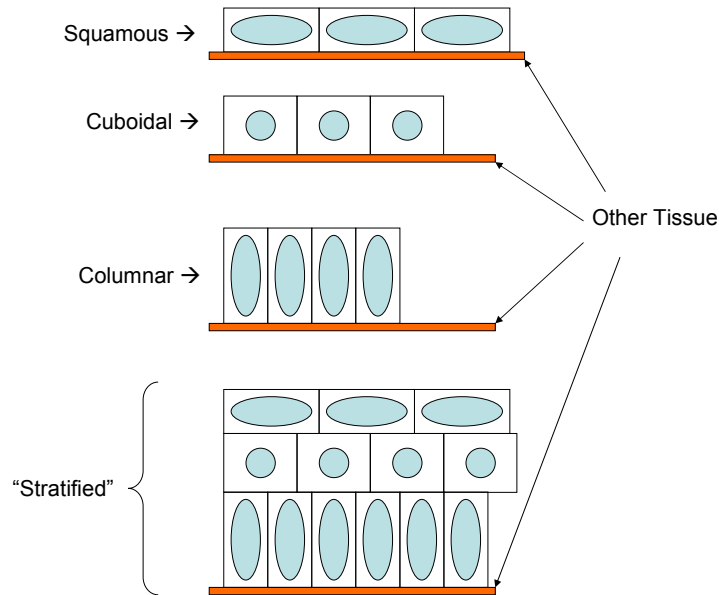


**Figure 5: “Basic” Types of Epithelial Tissue**

Epithelial cells may have ancillary structures on their lumen surface (away from the connective tissue), such as microvilli (in the intestine) or cilia (in the lung). The tissue that supports the epithelial layer is normally a collagen matrix (connective tissue) filled with a variety of non-epithelial cells (muscle tissue, immune cells, etc.). Technically, in the stratified case, there can be “Transitional” cells that are changing from one type to another, as in the case of the 7-layer “Stratified” epithelial tissue of the bladder. Figure 6 shows an example of lung epithelial tissue with certain areas labeled. In the case of the lung, the epithelial cells of the bronchi have cilia “sweepers” to move small particles back towards the mouth out of the lung. Particles that cannot be moved (or accumulations of fluid) can collect and impair the function of the alveoli, leading to a variety of medical problems or possibly even death.

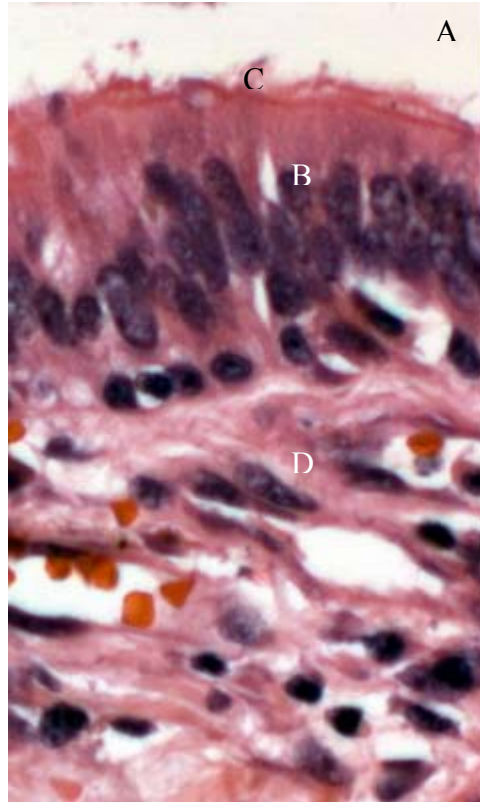


**Figure 6: Lung Epithelia, with (A) lumen, (B) epithelial cells, and (C) cilia, (D) connective tissue<sup>†</sup>**

### **Cells and Organelles**

While there have been over 200 types of cells identified in the human body, all are bounded by a phospholipid bilayer called the “plasmalemma” of 8.5-10 nm in thickness, containing proteins embedded in both the inner and outer surface. These proteins extend as much as 10 nm from either surface of the plasmalemma. The interior of the cell is normally divided into the nucleus and its surrounding cytoplasm. Inside each of these volumes, many organelles and substructures reside. The following table (adapted from Campbell, 1993 and from Perelman *et al.*, 2002) gives a sense of the types and sizes of these structures. The number of each of the structures varies

---

<sup>†</sup> Nikon E800, Applied Spectral Imaging system

with the type, health, and life-cycle stage of the cell. The spectral, absorptive, and scattering characteristics of a given cell depend heavily on the relative numbers of its (size-wise) major (>1000 nm) and minor (<1000 nm) structures. For example, mostly passive cells have only a few mitochondria, while highly active ones, such as high secretion (liver) or muscle cells (heart), have more than a thousand. In such highly active cells, the cumulative effect of the “minor” structures often outweighs the influence of the “major” ones.

**Table 2: Some sizes of Major and Minor (mammalian) cell organelles**

<b>Cell Organelle</b>	<b>Sub-Structures</b>	<b>Typical Shape</b>	<b>Diameter (nm)</b>
Nucleus		Spheroid	1000 - 5000
	Nuclear pores		100
	Prenuclear cisterna		20 - 40
	Ribosomes (on membrane)		20 - 25
	Heterochromatin (clump)		500 - 2000
	Heterochromatin (filament)		30
	Heterochromatin (nucleosomes)		4
	Nucleolus		500 - 1000
	Ribonucleoprotein particles		15
	Fibrillar centers		80
Mitochondria		Spheroid	200 - 800
	Inner Membrane		6
	Outer Membrane		7
	Space Between Membranes		10 - 20
	Cristae (outer membrane)		15
Endoplasmic Reticulum		Tubes, Sheets	(cytoplasm)
	Tubules		30 - 100
	Ribosomes (attached)		20 - 25
Golgi Aparatus		Cisterne	100 - 400
Lysosomes		Irregular	250 - 800
	Embedded granules		20 - 100
Peroxiomes			150 - 1200
Cytoskeleton		Filaments	(cytoplasm)
	Microtubules (0.2-2.5µm long)		25
	Intermediate filaments		8 - 12
	Microfilaments		7
	Cilia (2-20µm long)		250
	Flagella (10-200µm long)		250
Inclusions	Lipids, glycogen, etc.	None	20 - 500

As a point of comparison, the following table (summarized from Campbell, 1993) gives size information for some more general cell types found in biology, plus a few noteworthy organelles not found in mammalian cells.

**Table 3: Cell sizes and non-mamalian organelles**

Cell	Organelle	Typical Shape	Diameter (nm)
Typical Plant Eukaryote		Varies	
	Vacuole (+ Tonoplasts)		5000 - 8000
	Cell Wall	Flat	100 - 5000
Typical Bacteria		Varies	1000 - 10000
Typical Animal Eukaryote		Varies	10000 - 100000
Mycoplasmas		Sphere/spheroid	100 - 1000
Prokaryotes		Varies	1000 - 5000
Chloroplasts	Thylakoids, stroma		2000 - 5000

## 2.4 SPECTRAL APPROACHES

While there are several avenues for characterizing cancerous tissue that are now being actively used and/or explored, optical imaging - in comparison to techniques like ultrasound or X-rays, relying on single contrast mechanisms - holds the promise of several contrast mechanisms for observing pathological changes in tissue. These optical contrast mechanisms can broadly be classified into three types: absorptive, reflective/scattering, and fluorescent.

- *Absorption* is the process by which photons are attenuated by the materials they pass through. The absorptive process is frequency/wavelength dependent, and thus, known materials can often be distinguished by how much each frequency is absorbed. Because of the severe attenuation in passing through several centimeters of human tissue, this

mechanism is often coupled with some sort of reflectance or scattering imaging. Additionally, the heat generated by the absorption of energy can be used to determine some bulk characteristics (Dark *et al.*, 2000).

- *Reflectance/Scattering* occurs when (1) light passes through a significant index of refraction change or (2) impacts on a scattering body. Depending on which direction the photons deflect, various geometric and light interference patterns can be observed and used to determine various bulk qualities. Examples of this are “back-scattering” (Utzinger *et al.*), and Mie scattering (Mie, 1908; Backman *et al.*, 1999). In some cases, a situation can be set up to give additional characteristics to the backscattered light, such as in Raman spectroscopy (Kneipp *et al.*, 1998); while photon use is inefficient in this case, the information content is high and chemical signatures are obtainable.
- *Fluorescence* can either originate from intrinsic or extrinsic chromophores (Hellwig *et al.*). This process usually radiates photons in random directions, and thus image quality depends on collecting the radiated photons and on ascertaining when and where a given photon actually originated. Auto-Fluorescence Imaging is the use of intrinsic chromophores (Periasamy *et al.*, 2001), whereas conventional Fluorescent Imaging adds additional (possibly targeted) chromophores to the tissue, such as molecular “beacons” or “tags” (Kricka *et al.*, 1999, Li *et al.*, 2001) or protein analogs (Giuliano *et al.*, 1995) .

The photon emissions are usually in response to direct-photon excitation via lasers or broad-spectrum lamps (technically, the photons that excite are not the same as the ones emitted), though the emission can be influenced by various factors, such as chemical environment or photon density. Furthermore, it is possible to add agents that affect more than one type of contrast mechanism simultaneously (Vargas *et al.*, 2001). It is even possible to take the

coherence of the backscattered light to account (Wax *et al.*, 2002), similarly to Optical Coherence Tomography (OCT) approaches. Finally, one can take any of the above contrast mechanisms and track how they change in time for additional information, such as dose delivery (Mourant *et al.*, 1999).

No matter which of these types of imaging and data analysis are considered, one of the key means of quantification is to obtain a spectral signature. This signature can have a variety of features, such as patterns in the amounts of light observed at different frequencies, changes to the original source light, and/or changes over time, and can be the result of complex interactions of molecules (such as energy transfer). It is well known that certain materials absorb or emit (when stimulated) in particular set of frequencies (Kricka *et al.*, 1999). A collection of such characteristic frequencies associated with a single substance is called a “spectral fingerprint.” To date, investigations into the inherent spectral properties of cancerous tissue have tended to concentrate on the more bulk Spectral Response, but because of the highly scattering nature of human tissues (Kolarova *et al.*, 1999), what emanates from the tissue is not easily interpreted. Past and current approaches can usually be grouped into the following:

- Simple Reflectance (and Scattering): Shining “white” or monochromatic light on the tissue, and then detecting in the same frequency or frequencies. An extension of this is Scattering. In highly scattering media such as tissue, the resulting scatter-patterns can be analyzed to determine bulk properties (Backman *et al.*, 2001, Hielscher *et al.*, 1997).
- Fluorescence: Shining light on the tissue at one wavelength, and then detecting in another wavelength (or simultaneously a set of wavelengths, see Andersson-Engels *et al.*, 2000).

This can be repeated for sequentially for additional frequencies for additional information gain (Vaidyanathan *et al.*, 2000).

The two groups are normally limited to gathering information from less than 1 mm thickness of tissue. This limitation notwithstanding, for many conditions such approaches can aid diagnosis considerably. Many investigators have shown that there is a correspondence between changes in the spectral fingerprints obtained and morphological changes in the cells, though the exact correspondences are often unclear (Kwong *et al.* (2001), Brewer *et al.* (2001), and Coghlan *et al.* (2001)). While examples of these first two groups have been around for more than two decades, new scattering-based techniques have been introduced relatively recently. In particular, the elastic-scattering spectroscopy (ESS) proposed by Dr. Irving Bigio is quite promising. Variations of this approach have been investigated separately by Dr. Michael Feld (*et al.*) and by Dr. Rebecca Richards-Kortum (*et al.*), with similarly promising results, including cancer diagnosis. However, until now, ESS was applied only as a point-analysis method, not as an imaging modality.

## 2.5 DATA ANALYSIS

Investigators in optical diagnostics often take either a modeling-based or an empirical approach to analyzing their data. The modeling approach tries to simulate light-tissue interactions using photonic propagation models (Welch *et al.*). These models are usually heavily physics-based, requiring a deep understanding of the mechanisms involved, and take a long time to generate results. The empirical approach usually consists of simply shining light on the tissue, recording the resulting spectrum and then trying to find discriminating patterns in what is seen.

Deconstructing the resulting spectral response back into its constituent fingerprints has proven to be very difficult. Some investigators have taken a more constructive approach where specific signatures are determined in isolation, searched for in the resulting spectrum, and then adjusted according to some model. Chief among these is oxy-hemoglobin and deoxy-hemoglobin spectroscopy, since blood is an omnipresent constituent in animal and human systems. More generally, the current challenges in spectral imaging of *in vivo* tissue are as follows:

#### I. Tissue Intrinsic

A) Interference from blood absorption: Oxy-hemoglobin has two strong peaks around 540nm and 580nm, and this overlaps completely with Deoxy-hemoglobin, which has a peak around 550nm. Both generally absorb strongly between 500 and 600 nm (Palmer *et al.*). However, there are some frequencies where the absorption is the same for both, and are called isosbestic points.

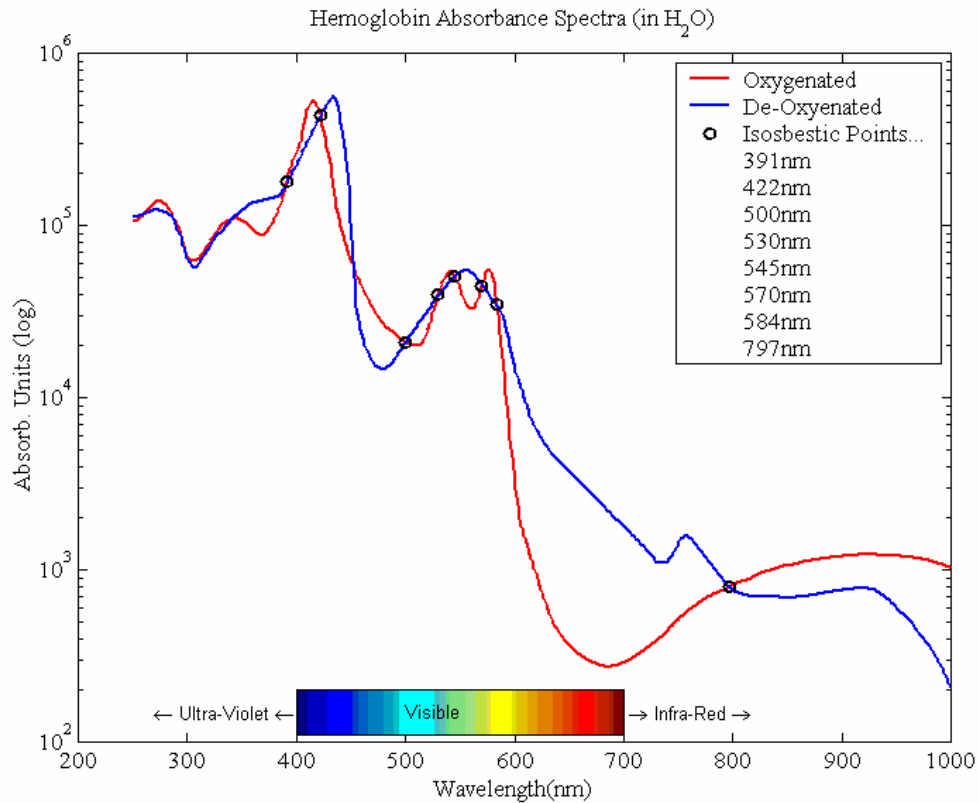


**Figure 7: Hemoglobin Absorption Spectra (Adapted from S. Prahl)**

B) Variations due to blood perfusion: Tissue under examination ebbs and flows mechanically with blood pumped by the heart. This causes variations in spectral amplitudes from the changes in oxy-deoxy ratios and total volume.

C) Many scattering bodies: Many of the larger intracellular organelles (in addition to the nuclei, such as mitochondria) readily scatter light because of index of refraction changes, and thus the resulting tissues become highly scattering, anisotropic media (Bigio *et al.*, 1997).

D) Changes to cellular processes induced by light: In some cases, long term exposure to light levels insufficient to kill a cell outright can have long-term effects (Sroka *et al.*,

1999), though keeping exposure times very short (sub-millisecond) seems to alleviate this problem.

E) Chromophore bleaching: Depending on the chromophore, the observed autofluorescence emission can become weaker with the length of exposure to the excitation frequencies, and with cellular chemistry changes (Brooks *et al.*, 1999).

F) Overlapping absorption/emissions patterns: Separating out the components that make up a spectrum (in the presence of noise) can be very difficult, but some techniques to do this exist such as Chemometrics (Brereton, 1999), or Stokes/Excitation-Emission Shift Spectroscopy (Alfano, 2003).

## II. Intra-subject Variability

A) Racial and age differences (melanin content of skin)

B) Internal organs that normally are never exposed to daylight, such as the cervix (Brookner, *et al.*).

All of the above will affect the resulting spectrum gathered by optical instruments. On top of this, the instrument itself may have its own “absorptive fingerprint,” though this can usually be fully characterized and compensated for well in advance of data collection.

### 2.5.1 Spectral Analysis

Analyzing spectral imaging data is not new—the military has been doing it for years with satellite reconnaissance imagery. But while those algorithms are very good at finding similar pixels, they are not very good at attaching meaning to the observed spectral responses. These spectral responses can be recorded in an imaging mode using a variety of tools, such as Acousto-

Optical Tunable Filters, gratings, Fabry-Perot interferometers, Fourier Transform Spectroscopy, Liquid Crystal Tunable Filters, prisms, interference filters, etc. Data can be acquired either one frequency band at a time (band-sequential), or all the frequency bands for some sub-part of the image space (space-sequential). Regardless of how the spectral information is acquired, it then must be analyzed and converted into some form that emphasizes the items of interest in a perceptible way. Spectral analysis of several of the possible contrast mechanisms have already been applied with some success to the diagnosis of cancerous tissues:

Bladder: Arendt *et al.*, 1997 (Auto-fluorescence)

Breast: Li *et al.*, 2001 (Markers)

Bladder: Mourant *et al.*, 1995 (Elastic Scattering)

Cervix: Brookner *et al.*, 1999 (Auto-Fluorescence)

Collagen: Tang *et al.*, 2000 (Auto-Fluorescence)

Colon: Rava *et al.*, 1990 (Auto-Fluorescence)

Epithelial cells: Backman *et al.*, 1999 (Mie scattering)

Head and neck cancer: Betz *et al.*, 1999 (Auto-fluorescence)

Lung: Shibuya *et al.*, 2003 (Auto-fluorescence), Huang *et al.*, 2003 (Raman)

MS-2 Fibrosarcoma: Colasanti *et al.*, 2001 (Auto-Fluorescence)

Nose (Nasopharyngeal): Qu *et al.*, 2000 (Auto-Fluorescence)

Ovaries: Brewer *et al.*, 2001 (Auto-Fluorescence, multiple)

Stomach: Chwirot *et al.*, 1997 (Auto-fluorescence)

Most of the above investigations of spectral “fingerprints” have taken an approach whereby the spectrum (which contains many fingerprints all lumped together) is obtained, and then analyzed *en masse*. Examples of this analysis are:

- Simple Correlations
  - Emission-Excitation matrices (EEM): Monochromatic light is scanned across a range of frequencies (X-axis), and the obtained values (Z-axis) for each frequency (Y-axis) are plotted. Contours in the Z-plane (correlation) are then calculated and the peaks chosen as significant and used for further study.
  - Wavelength ratio matrices (WRM): Similar to the EEM above, the individual frequencies of the Y-axis are replaced by pairs of frequencies, whose value (Z-axis) is the one divided by the other. Contours and peaks are chosen for further study.
- Advanced Approaches
  - Principal Component Analysis (PCA): This is a multivariate procedure that essentially transforms a set of correlated variables into an uncorrelated set, and then selecting the variables with the greatest variability. This process reduces the dimensionality of the data set while retaining as much information as possible. PCA makes few assumptions about what is being analyzed, and this makes it a good general technique. However, often the resulting components have no easily ascribed physical meaning.
  - Pixel un-mixing (linear de-combinations): Given a set of “ideal” or assumed-to-be-representative signatures, each pixel is classified as a linear combination of the ideal signatures. This classification can be “all or nothing,” but usually each signature is assigned a pseudo-color. (See Figure 8 for an illustration).
  - Clustering: Spectra are grouped together based on a ground truth, then the groups are used to make future predictions/classifications

- Fourier/Wavelet transforms: A set of basis functions are used to match against the signal, and the resulting set of correlations is then analyzed for significant patterns.

More recent investigations have focused on pixel un-mixing, in spite of its limitation that the “ideal” signatures to be compared must be known *a priori*. Using a library of a few “ideal” curves, the picture can be pseudo-colored with intensities of a given color reflecting how much each of the curves contributes to the given pixel. Figure 8 illustrates the results of this process, starting with a spectral cube.

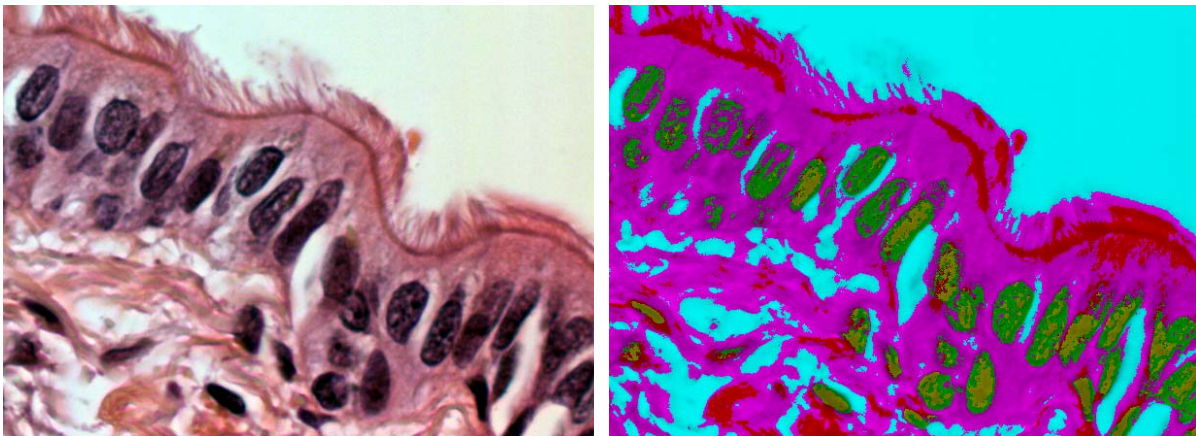


**Figure 8: Brightfield image (left) and pixel unmixed (right, pseudo-colored with 5 identified spectral components of interest)**

### **2.5.2 Other types of light-based analysis in biological and medical applications**

There are many other types of imaging used in biological and medical applications that do not depend on spectral approaches. Without an attempt to artificially classify these, a list of the more broadly used methods is as follows:

- Optical Coherence Tomography (OCT): Using a distance reference, backscattered photons which travel more or less than the distance (hence deeper or shallower than the desired penetration depth) are ignored. This allows an image to be formed (ideally) from only the photons that have backscattered off of things at the desired depth. Morphometric information is derived from refractive index inhomogeneities, and 3-D images can be generated by scanning.
- Second Harmonic (SH): Because of molecule anisotropy and localized electric field effects, this second-order effect causes some of the incident light energy to be scattered at twice the original frequency (Campagnola *et al.*, 2003)
- Raman Scattering (Raman): The perturbed electron may not return to its original energy state, thus gaining or losing a small amount of energy in this process. Statistically this occurs very infrequently, and results in an emitted photon that is not exactly the same wavelength as the original one. The resulting changes (originating in photon-phonon interactions) are based on - and therefore able to probe - the molecular structure of the material. The scattering is termed Anti-Stokes Raman Scattering (in the case of a higher resulting energy state, but no charge shift) for the electron, and Stokes Raman Scattering (in the case of a lesser energy state).
- Multi-Photon Excitation (MPE): In this technique, two (or more) photons striking the molecule nearly simultaneously, and this situation only occurs with sufficient photon flux density, at the focal point of a (microscope) lens. The energy of the MPE photons are combined in a non-linear way, having the effect of “adding together” the energy of the photons and thus being equivalent to the arrival of a photon with twice the energy (= half

the wavelength). Since this effect is usually confined to just the focal point of a lens, this allows for imaging very small volumes (~100 atto-liters; Webb, 2003).

- Fluorescence (or Forster) Resonance Energy Transfer (FRET): Photonic energy is absorbed by the target molecule and is then transferred (non-radiatively, in a dipole-dipole interaction) from this donor to a nearby (or bound) molecule (acceptor). The observed fluorescent signal is then generated by the energy recipient.
- Fluorescence In-Situ Hybridization (FISH): When the target fluorescent molecule binds with another molecule, the binding physically changes the fluorescing part of the target molecule and thus causing a change in the observed fluorescent signal. This technique is commonly found in DNA assays, where the binding action of molecules targeting specific DNA sequences turns on the fluorescent signal, indicating the presence of that sequence.
- Fluorescence Lifetime Imaging Microscopy (FLIM): The target molecule is first excited with a brief (laser) pulse. The energy remaining in the molecule will continue to be converted to a fluorescent signal, but will fade with time in a manner influenced by the various mechanisms present in the molecule for storing and transforming the energy and its environment.
- Fluorescence Recovery After Photo-bleaching (FRAP): The target molecule(s) fluorescence signal is extinguished (bleached), and time to signal recovery is measured, effectively providing a concentration diffusion measurement.
- Fluorescence Correlation Spectroscopy (FCS): Based on the fluctuations in the intensity over time (due to changes in the quantum yield or to the diffusion of molecules), it

becomes possible to estimate the number (or ratio) of molecules under observation, and to estimate the translational diffusion coefficient of a given fluorescent molecule.

It should be noted that it is possible to effectively mix two or more approaches together for additional information. For example, MPE with either FLIM or FRAP. It is also possible to give some directionality to the fluorescent photons, or alter a given molecule's fluorescent characteristics, by the introduction of nearby metal structures; this is commonly referred to as Radiative Decay Engineering (Lakowicz, 2001). The Mie scattering which will be covered in the next section is another example of a "perturbation" signal.

## **2.6 MIE THEORY**

Fundamentally, Mie theory (Mie, 1908) is a mathematical expression of the interaction of Light and spherical scatterers. Mie theory covers both metal and dielectric spheres, both absorbing and non-absorbing. However, for the purposes of this dissertation, this discussion will be limited only to dielectric spheres, either absorbing or non-absorbing, but some details about mathematically representing light need to be covered first.

### **2.6.1 Light (classical optics)**

According to classical optics, light can be expressed as an oscillating electric field ( $E$ ) of two components ( $E_x$  and  $E_y$ ) at right angles to each other. Fundamentally, both of these (sinusoidal) fields have the same amplitude ( $A$ ) and frequency ( $\omega$ ). However, the two fields may not be in-

phase relative to each other, and this difference in phase is called polarization ( $\phi$ ).  
Mathematically,

$$\begin{aligned} E_x &= A_x \cos(\omega t + \phi_1) \\ E_y &= A_y \cos(\omega t + \phi_2) \\ \phi &= \phi_1 - \phi_2 \end{aligned}$$

Note that it is also possible to instead write  $\phi$  as a change in the amplitudes  $A_x$  and  $A_y$  (and reflecting that change in the equations which follow), but for this discussion we will not use this option. The results, however, would be the same.

For the purpose of this discussion, one can define the “phase lag” ( $\tau$ ) between two electric fields (i. e.  $R_1$  &  $R_2$ ) that have the same frequency, commonly the incident light and either a reflected or refracted component. Mathematically,

$$\begin{aligned} R_1 &= \begin{cases} E_{1x} = A_{1x} \cos(\omega t) \\ E_{1y} = A_{1y} \cos(\omega t + \phi_1) \end{cases} \\ R_2 &= \begin{cases} E_{2x} = A_{2x} \cos(\omega t) \\ E_{2y} = A_{2y} \cos(\omega t + \phi_2) \end{cases} \\ \tau &= \phi_1 - \phi_2 \end{aligned}$$

When light transitions from one substance (air, for example) into a dielectric substance (water, for example), some of the light is reflected (light that does not pass through the interface) and some is refracted (passes through the interface). How much light is reflected and refracted is dependent on the fundamental frequency of the dielectric, the angle of incidence, and the polarization of the light. Technically, the reflected light has its polarization rotated by 180 degrees, but this is normally not important. The angle of the refracted light is determined by the phase lag between the incident light and the refracted light, and is otherwise known as the “refraction index” of “Snell’s Law.” A key thing to note is that it is possible to minimize the amount of light reflected for either the  $E_x$  or the  $E_y$  component (but not both at the same time) by

carefully selecting the angle of incidence. In some cases it is possible to minimize one of the components to have zero reflected energy at a certain angle, and this angle is commonly known as Brewster's Angle. There is no angle for which all the energy (both components together) in the light passes through unaffected by the interface.

This dissertation will assume that all planar electromagnetic wave-fronts ("light rays") are linearly polarized, and that two wave-fronts have "parallel" polarization if they share the same polarization angle or differ by 180 degrees. Likewise, two wave-fronts that differ by 90 or 270 degrees will be considered "perpendicular." While polarizations that are not multiples of 90 are possible, such details are beyond the scope of this analysis. For convenience, all "incident" wave-fronts will be considered to have a polarization of zero degrees.

### 2.6.2 Introduction to Mie Theory for dielectric spheres

Consider a non-absorbing dielectric sphere that allows a significant amount of light to pass through it, and is observed at a distance of several times the wavelength of the incident light (in the "far field"). When light (a planar, electromagnetic wave-front) strikes the sphere (point A, Figure 9), some light is reflected off and some passes into the sphere.

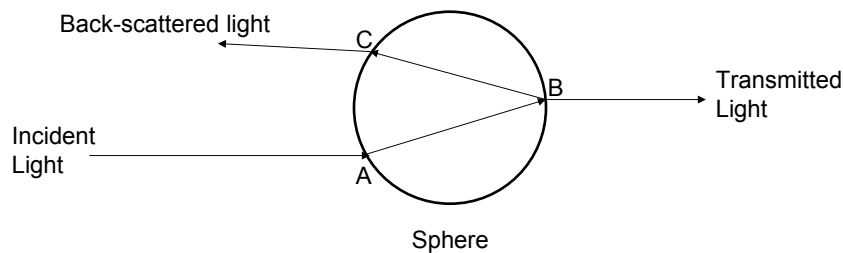


**Figure 9: Sphere optical path**

When the light leaves, again some light is reflected off the interface (point B, Figure 9) and some passes through. The reflected light continues back to the first interface, (point C, Figure 9), and again some light passes through and some is reflected. The resulting "backscattered" light is much weaker than the original incident light, and because it has passed through a different medium there is a phase lag between it and the original incident light. This phase lag is based on the length of the path through the bead, and so the phase lag is dominated by the diameter of the sphere. If the diameter of the sphere is much larger than the wavelength of light, then the phase lag will become too large and the clear correlation between the incident and backscattered light will be lost, making the detection of this phase lag nearly impossible (usually appearing as "random" noise at the detector). If the diameter of the sphere is much smaller than the wavelength of light, the phase lag will become too small to be effectively measured (again, becoming "random" noise). However, for a given sphere diameter, there will be a range of wavelengths for which the lag is neither too short nor too long. This is the situation that Mie scattering focuses on.

The path that the light takes traversing the sphere is not a constant, and this variation translates to a spatially dependent phase lag around the sphere, relative to the incident light. Mathematically speaking, the relation between the incident wavefront ( $E_i$ ) and the scattered wavefront ( $E_s$ ) in the far field can be expressed in terms of a scattering amplitude matrix  $S$ , which is a simplified form of a Mueller matrix that relates the corresponding Stokes vectors:

$$\begin{pmatrix} E_{sx} \\ E_{sy} \end{pmatrix} = \frac{e^{-i(\vec{k}\vec{r}-\omega t)}}{i\vec{k}\vec{r}} \begin{pmatrix} S_1 & S_3 \\ S_4 & S_2 \end{pmatrix} \begin{pmatrix} E_{ix} \\ E_{iy} \end{pmatrix}$$

where  $k$  is the wave vector,  $\omega$  is the frequency, and  $r$  is the direction of propagation of the scattered wavefront (in the spherical system of reference associated with the sphere).

In the case of a perfect sphere, both  $S_3$  and  $S_4$  can be assumed to be zero. It has been shown by Gustaf Mie that  $S_1$  and  $S_2$  are expressed as an infinite series of Bessel Functions based on the wavenumber, the diameter of the sphere, and the relative refractive index (more discussion on this to follow).

The scattered light pattern as a function of angle is shown for  $S_1$  and  $S_2$  in Figure 10.

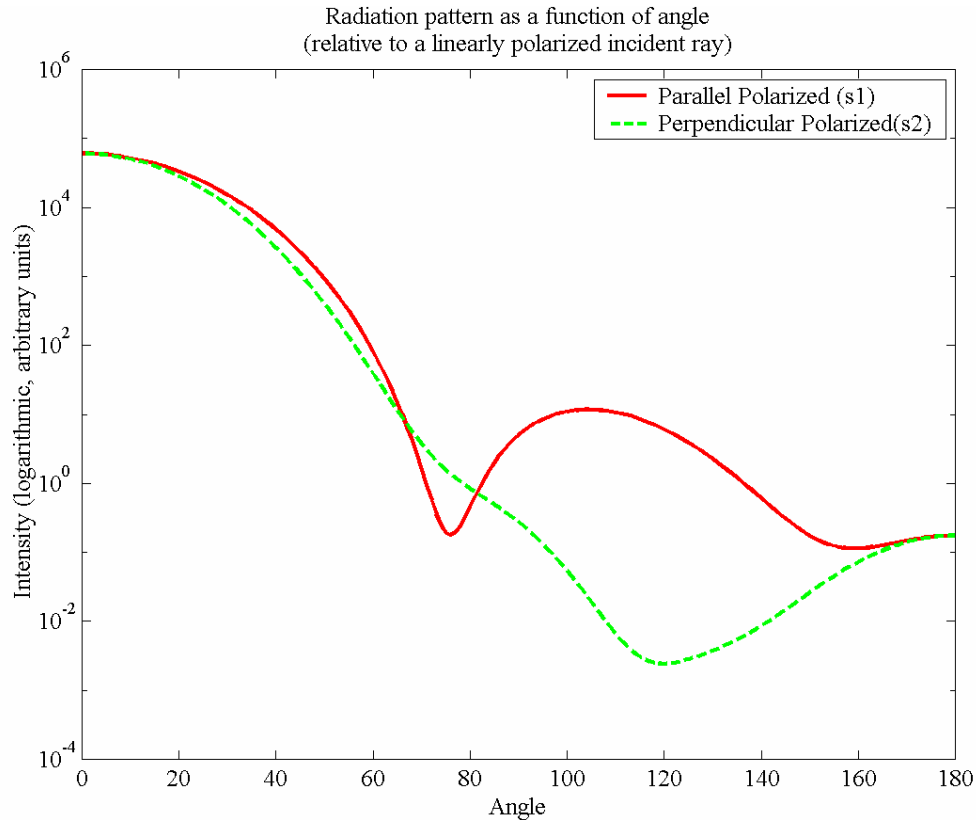


**Figure 10: Example radiation pattern as a function of angle**

Assuming that the wavelength of light is on the same order as the diameter of the sphere, the pattern is controlled by two basic parameters. The first parameter is the ratio of the index of refraction of the outside medium to the bead material. The second parameter is the ratio of the Size of bead to the wavelength of the light in the medium.

$$M = \frac{REF_{bead}}{REF_{medium}}$$

$$X = \frac{\pi(diameter_{bead})}{\lambda \cdot REF_{medium}}$$

**Figure 11: Key Mie parameters**

These dimensionless parameters control the radiance pattern given the previous assumptions (bead diameter is similar in magnitude to wavelength). Non-absorbing spheres have real refractive indices, while absorbing spheres add an imaginary term to  $REF_{bead}$ . If three of the above variables are known, the radiation pattern can be used to empirically determine what the fourth must be. For example, Figure 12 shows the resulting patterns for several example values of  $X$  as a function of angle assuming  $M=1.33$ . Dotted lines are  $S_2$  terms of the scattered light, and the solid lines are the  $S_1$  terms of the scattered light.

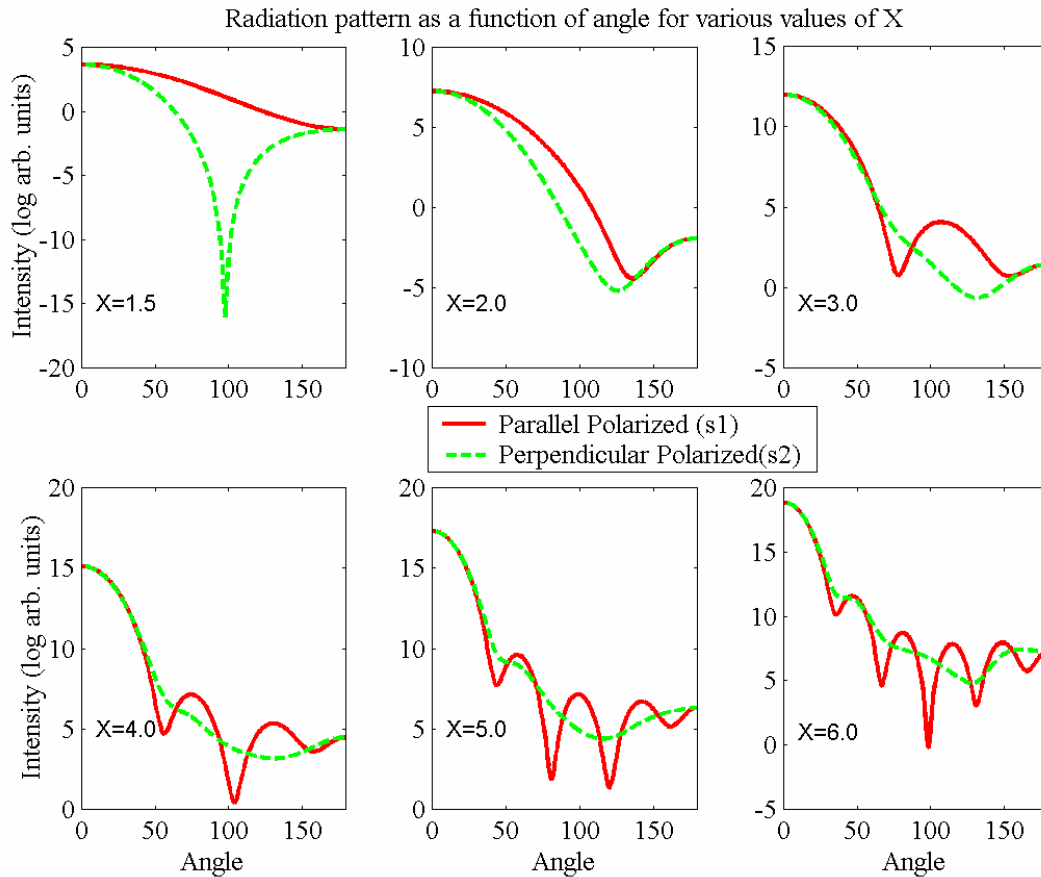


**Figure 12: Radiation pattern variation as X changes**

Note that in this example, 180 degrees is total backscatter of the light back along the incident light and there is no difference between the terms. Likewise this is the case for total forward scattering (at 0 degrees). If one were to choose a single color of light and carefully choose the angle, it would be possible to distinguish the various values of X. A more robust way of distinguishing the patterns is either to sample several different angles, or several different wavelengths at the same angle.

Having shown that the phase lag of the light varies with the length of the path through the beads, and that the lag is dependent on two parameters M and X, it is now possible to ask what the signal might look like. First, it must be noted that both M and X are dependent on

wavelength, further complicating matters. Focusing first on this simplest case of light-bead interaction, assume that the incident light wavefront impinges at a right angle to the surface of the sphere, passes through the center of sphere, and exists the opposite side of the sphere. The situation described is often referred to as the forward scattering extinction case, shown by Van de Hulst (1957; page 176) to be characterized by:

$$Q_{scattering} = 2 - \frac{4}{p} \sin p + \frac{4}{p^2} (1 - \cos p)$$

$$p = 2X|M - 1|$$

It should be noted that Van de Hulst equation only predicts the resonant signal, and does not incorporate additional terms for the high-frequency “ripple” signal. This so-called “ripple” signal is apparent only if the Mie calculations are done in their full detail, and is shown in Figure 13 (from Van de Hulst, 1957). Note that the amplitude of the “ripple” is small enough throughout to be (safely) ignored for the purposes of the work described in this dissertation.

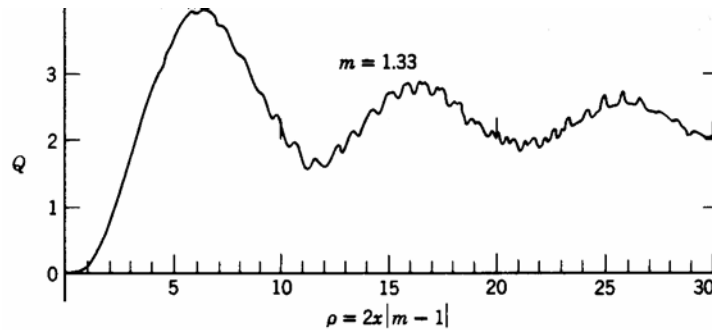


Figure 13: Example Q vs P plot (M=1.33, X increasing) ‡

‡ Taken from “Light Scattering by Small Particles” by Van del Hulst, copyright 1981 by Dover Publications. Reproduced with permission of Dover Publications.

Also, the range of the M parameter is limited to about  $1 < M < 2$ . However, for the scope of this dissertation, these limits are not exceeded. It should also be noted that the sinusoidal functions imply that a given bead size should yield an oscillatory signal as the frequency changes. More importantly, the  $p$ -parameter allows one to make an estimate of X if M is known and  $p$  can be estimated from the observed signal. Going the other way, treating  $p$  as a phase term, the period of the oscillations can be roughly estimated by assuming that the indices of refraction are constant over the range. However, because of the inverted wavelength term of X,  $k$  will be substituted for  $\frac{1}{\lambda}$  in the analysis. This estimation yields the following equation for the “k-space periodicity”:

$$\Delta k = (\text{diameter}_{\text{bead}})(M - 1)(REF_{\text{medium}})$$

Since the conversion to k-space is not a linear one, equating it to the linear optical wavelength domain is non-trivial. Still, it can be used as an additional check for the results. For example, in the case of 1.0  $\mu\text{m}$  polystyrene beads in water, the periodicity of the signal should be somewhere in the neighborhood of 0.50  $\mu\text{m}^{-1}$  in k-space. Furthermore, when comparing the signals of one bead of a certain diameter with the signal of a bead twice that diameter, the second signal should be half the period (twice the frequency) of the original signal. Figure 14 illustrates this point by plotting the (ideal) Van de Hulst equation for spheres that differ only in diameter, by a factor of two:

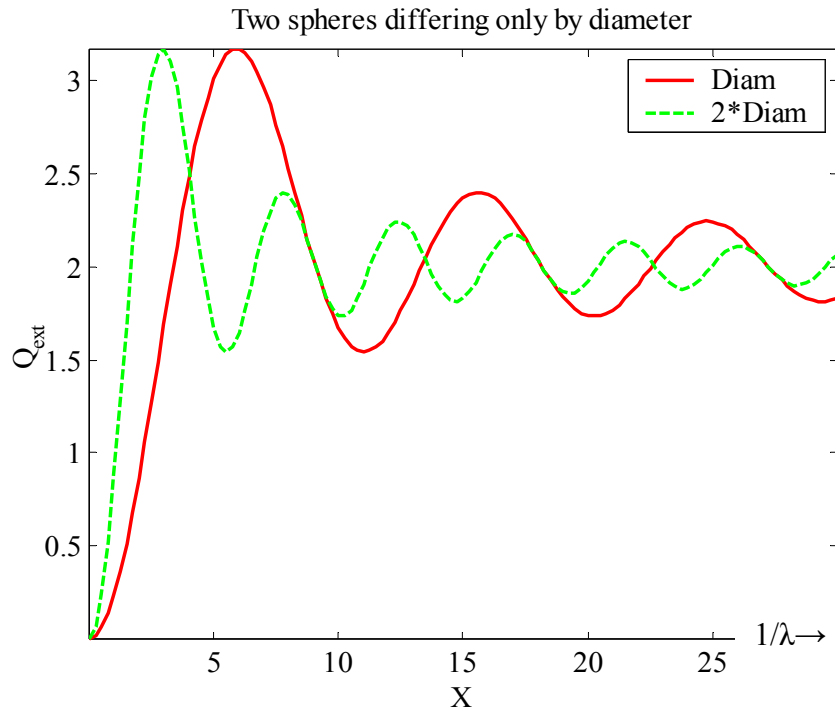


**Figure 14: Two spheres differing only in diameter (by a factor of two)**

## 3.0 METHODS

The following sections describe the main techniques and procedures used in this project.

### 3.1 HARDWARE DEVELOPMENT

For this project, a new type of endoscope was developed. This endoscope has the ability to rapidly scan the visible spectrum and acquire band-sequential images of tissue *in vivo*. The major design goals of the endoscope were as follows:

- Distal end (the part that goes into the patient) needs to be able to fit within a 2 mm instrument channel of common endoscopes
- System must be a non-contact, imaging scope (as opposed to a point-source tester)
- System must capture all needed data in less than 0.5 seconds
- System must be portable enough to take to the OR and able to be moved about the patient bedside by one person.

The endoscope system that was built satisfies all the major design goals. A block diagram of it is shown in Figure 15.

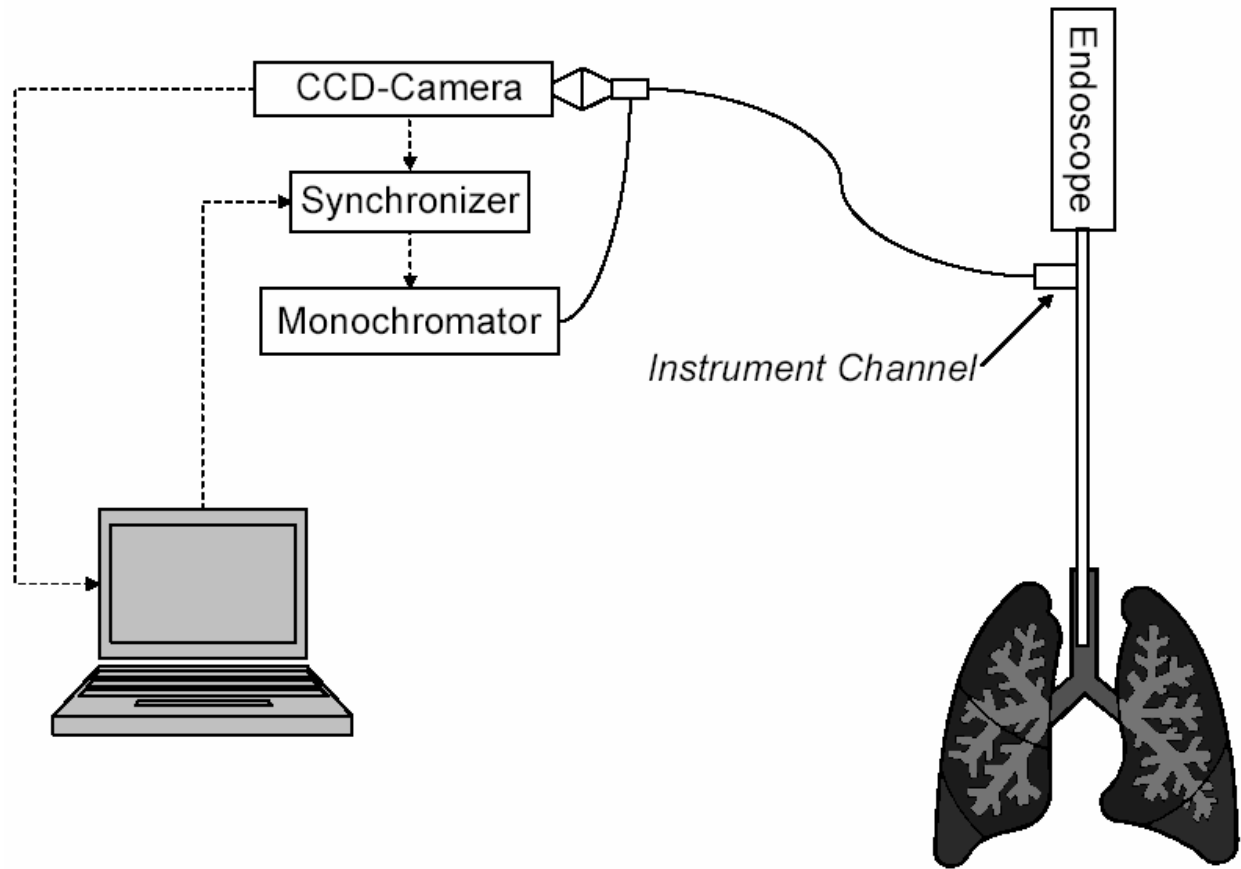


**Figure 15: Block diagram of the HSIE**

Referring to the above figure, the endoscope consists of a normal commercial endoscope, with an additional 2 mm imaging fiber bundle (described in the next section) placed in the instrument channel; a high-speed monochromator (light source); a high-sensitivity, high-speed CCD camera; synchronization electronics; and a processing computer. The fiber bundle can be reoved as needed by the operator, and in fact can be used in any standard endoscope such as the one included with the commercial, auto-fluorescence-based Olympus “LIFE scope.” The entire system obtains reflection-ESS (Elastic Scattering Spectropy) images at 60-120 per second and collects and stores the data as well as biopsy notes. For each optical biopsy, 32 images of differing wavelengths are obtained, and grouped into a single “spectral cube” (a two-dimensional

image where each pixel is a set of intensities at the different wavelengths which comprise the third dimension, thus forming a three-dimensional dataset). The following Figure 16 is a picture of the actual HSIE endoscope in the operating room.

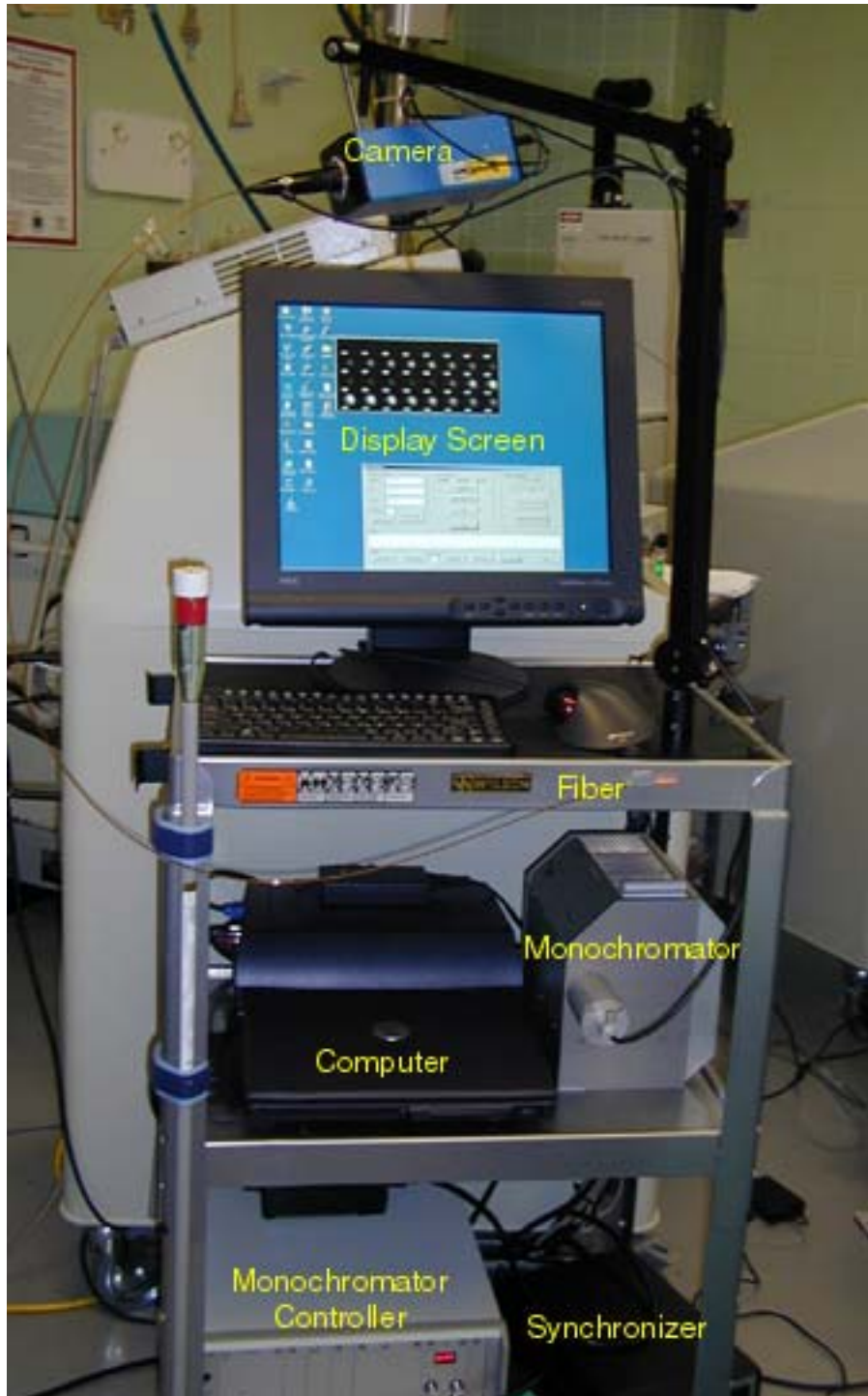


Figure 16: Hyper-spectral imaging endoscope components

### 3.1.1 Custom Fiber

The custom fiber was built to our specifications by Instrument Technologies, Inc., since we had no experience in making the fiber sterilizable. The “fiber” actually consists of a single solid-core fiber for the illumination, and two 10k-fiber imaging bundles with matched polarizers and lenses (Figure 17, left) configured in an equilateral triangle within the tip of the “fiber.” This design allows both polarizations of light to be simultaneously carried back to the camera.

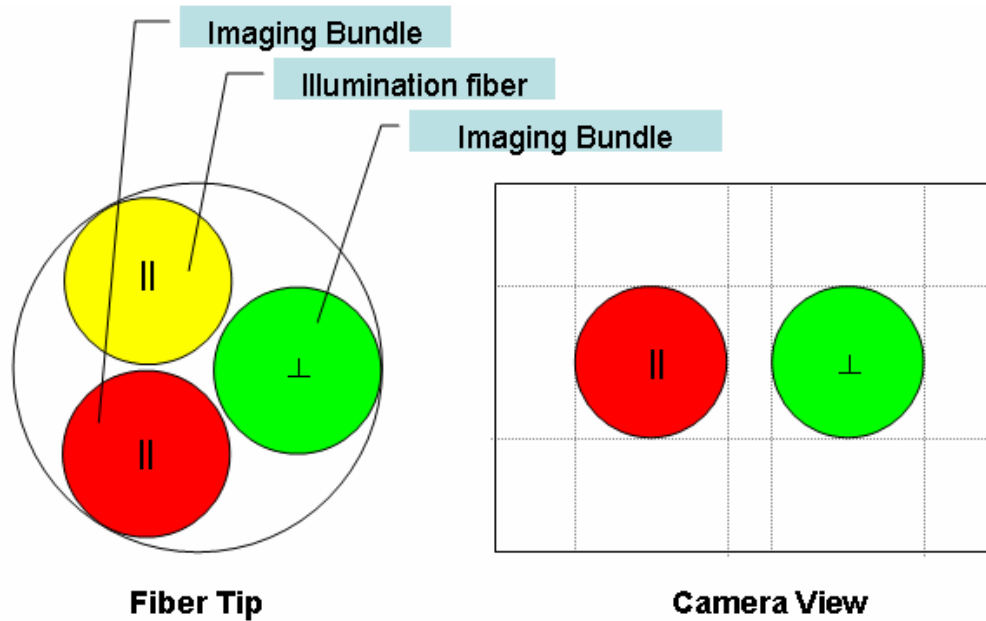


Figure 17: Fiber tip (left) and camera view (right)

The camera’s field of view (Figure 17, right) only contains the two imaging bundles and allows both polarization images to be obtained in a single camera exposure. The imaging fiber bundles do not fill the cameras view and thus some pixels are unutilized. For the current application of the HSIE to lung cancer, low light levels have forced 4-by-4 binning to be used. The binning and

unutilized pixels ultimately result in each imaging bundle's square (viewing area) to be reduced to 72 pixels by 80 pixels.

### **3.1.2 Design and Implementation**

As part of this thesis, two versions of the master synchronizer were built (see Figure 18 and Figure 19) and software for the Hyper-Spectral Imaging Endoscope (HSIE) was written. This HSIE was designed to obtain both (parallel and perpendicular) surface reflectance spectra at high speed. The master synchronizer aids in this by watching the camera and changing the frequency of the monochromator's emitted light when the camera isn't acquiring. Since the monochromator can switch in 2.5ms, the entire system is currently limited only by the camera's acquisition speed of 120fps (8 ms/frame) and its light sensitivity.

The synchronizer employed a PIC Microchip™ microcontroller to store sequences of voltage changes, and digital-to-analog conversion circuitry to drive the Polychrome IV monochromator. The controller interfaces to the laptop computer through a standard RS232 serial port, using the protocol documented in Appendix A. Since the monochromator must be sequenced very quickly in time with the camera, the voltage sequence is first downloaded in its entirety to the microcontroller's memory through the slow serial port. The computer then instructs the sequencer to watch the camera, and then the computer collects the images. As each image is taken by the camera, the synchronizer watches for the time period when the camera "shutter" is closed and then changes the voltage output (=monochromator's illumination frequency) in accordance to the stored sequence. Additionally, when the microcontroller is not watching the camera signals, it watches the external pedal. When the pedal is depressed (usually,



Two versions of the synchronizer were built because a second HSIE was needed as part of a second grant. The second design improves on the first by adding some expansion capabilities, a newer version of the microcontroller, and isolating the analog amplifier section from the digital logic section to reduce noise on the output channel. Furthermore, new packaging variants of the older parts were available. Thus, version two of the controller offers improved control stability, smaller size, and increased memory for storing longer sequences. To summarize, the master synchronizer built for this research is what allows the system to operate at the desired frame acquisition rates. To increase the rate further, a faster camera would have to be used.

### **3.1.3 Imaging Components**

To collect the images that would be analyzed, a fast-shuttered camera with good intensity resolution, good quantum efficiency, and hardware-pixel binning (for low light intensities) was needed. After much searching, a 12-bit, 60+fps camera manufactured by Cooke Corp. (Sensicam Model 360) was chosen. With a fast camera, and equally fast (or faster) and selectable light source was needed. In this case, a fast monochromator (Polychrome IV, with an analog interface) was purchased from TILL Photonics, and slightly modified. This light source in particular was used because of its ability to change the frequency of the selected light in less than 3 ms, thus allowing the illumination to be easily changed between faster camera exposures.

### **3.1.4 Additional System Components**

The remaining parts of the HSIE were all obtained from commercial vendors. The computer laptop and docking station (Model C100) were purchased from Dell Computers Corp. The Model

C100 was chosen because its docking station could accommodate the two full-size PCI cards that were needed for the camera interface and second video card. The 18" LCD monitor was obtained from Computer Discount Warehouse (CDW.com), and was chosen for good price/performance while being readable at a distance. The cart was purchased from Endoscopy Support Services, and was used to make the entire HSIE system mobile as well as for serving as a point of attachment for the camera arm. The camera arm was obtained from Special-T-Shop Manufacturing, and was used to allow the camera to be suspended near the doctor to compensate for the short imaging fiber length.

## **3.2 EXPERIMENTAL VALIDATION (MODEL) SYSTEMS**

### **3.2.1 Cuvette-based Model System Development**

One of the first methods to test any optical sensing system is to employ cuvettes filled with known substances. Cuvettes should give a concentrated, unadulterated signal for comparison or verification purposes. The empirical results obtained from the cuvette work can be used to refine the systems or models, and to test fundamental abilities of the imaging system. More complex imaging tests can be done with the tissue phantoms. For these tests, cuvettes of varying concentrations of the model materials will be scanned by the HSIE and the resulting data used to refine the signal analysis for the phantoms.

For the first set of cuvette experiments, water and polystyrene bead suspensions were used. The reason for this is that the relative refractive index will be high for water + polystyrene, and according to the Mie theory, this should increase the backscattered signal. Agarose gel and

polystyrene beads were also used as this was the basis for the tissue phantoms and any significant differences needed to be identified early. In these experiments, specular reflection from the cuvette wall was avoided by placing the illumination/collection fiber at such an angle to the target surface that Fresnel (specular) reflections are avoided (in the case of the HSIE, 40 degrees from the surface perpendicular should suffice). It should be noted, however, that this angle is not the angle between the illumination and collection fibers.

### 3.2.2 Tissue Phantom Development

Tissues phantoms are commonly used for a variety of testing purposes. One of the strengths of using phantoms is that their properties can be precisely and reproducibly. This allows a phantom with known properties to be used as a “ground truth” to test the imaging system and to help estimate system performance. Since epithelial tissue consists of two regions (epithelial cells and a connective tissue layer supporting it), it was natural to use phantoms that were built using a two-layer design.



**Figure 20: H&E stain of Lung lumen (left) and phantom diagram (right)**

Looking at Figure 20 above, the top layer simulates the epithelial cells, and the bottom layer simulates the diffusive backing tissue common in the human lung. In the case of the cancerous

lung tissue that can be imaged with an endoscope, and which may exhibit dysplasia, nuclei with a diameter of 4-7  $\mu\text{m}$  are considered “normal,” and those in excess of 10  $\mu\text{m}$  to be “abnormal.” Polystyrene beads are available in certain sizes, and so a size of 4.3  $\mu\text{m}$  (+0.5 $\mu\text{m}$ ) were used to represent “normal” nuclei, and a size of 10  $\mu\text{m}$  (+1 $\mu\text{m}$ ) will be selected to represent “abnormal” nuclei. Furthermore, to verify that the signal can be detected, additional beads of 0.5  $\mu\text{m}$ (+0.05) and 1.0  $\mu\text{m}$ (+0.1) were used as well. In the results section, the same phantoms were used for the various spectral scans to make the results comparable with each other.

### 3.2.2.1 Formulation

The top layer was built by placing drops of a still-warm suspension of polystyrene beads and agarose onto the flat surface of the bottom layer and then allowing them to spread out and cool. This technique was first described in the paper by Bartlett *et al.*, 2002. The bottom scattering layer preparation is based on the unpublished notes kindly supplied by Ousama A’Amar, working in Dr. I. Bigio’s lab at Boston University, and is formed by suspending  $\text{TiO}_2$  crystals in an agarose gel. The recipe that was used to make the phantoms is as follows:

- Materials
  - Agarose (Pierce, 17850)
  - $\text{TiO}_2$  crystals (J.T. Baker, 4162-01)
  - Polystyrene beads, purchased in a 2.5% suspension, 4.3 $\mu\text{m}$  (17140-5) and 10 $\mu\text{m}$  (18133-2) diameters, from Poly-Science, Inc.
  - A hot (70 degree Centigrade) water bath
  - Ultrasonic bath (sonicator)

- Petri dishes (or similar container to be used for the phantom)
- Various small and large test tubes, and some mixing containers
- Pipettes
- Optional bead surfactant: HEPES (N-2-Hydroxyethyl Piperazine-N<sup>1</sup>-2-Ethane Sulfonic acid, from Research Organics, 6003H) at pH 8.0

- Building the bottom (scattering) layer

To build the bottom layer, mix H<sub>2</sub>O with the Agarose, and then mix in TiO<sub>2</sub> into a slurry. For each 1ml of bottom layer material, 10mg of Agarose and 1.6mg of TiO<sub>2</sub> is needed. (For the phantoms built to test the HSIE, 3ml of bottom material was used for each phantom. Thus 3ml H<sub>2</sub>O, 30mg of Agarose, and 4.8mg of TiO<sub>2</sub> was used for each one.) Prior to mixing the H<sub>2</sub>O with the Agarose, 1-2ml of the H<sub>2</sub>O was separated and mixed instead with the TiO<sub>2</sub> to form a slurry and sonicated. The slurry is then placed in the hot bath. Mix the H<sub>2</sub>O with the Agarose, heat in a microwave until it boils, making sure that the Agarose mixes well and does not settle to the bottom of the container. The hot mixture should be clear and not cloudy at the bottom. After it cools down for a few seconds, mix with the slurry and sonicate. If the white slurry turns gray, the mixture was too hot. In this event, the Agarose and TiO<sub>2</sub> crystals have reacted and the step will have to be repeated. Finally, place the container into the hot bath to keep it warm while transferring the proper amounts into the petri dishes. Let the bottom layers cool until firm, and then place in a refrigerator until cold. The result is illustrated in Figure 21.



**Figure 21: Bottom layer constructed**

- Building the top layer

To build the top layer, one needs to make the agarose gel, mix in the polystyrene beads, and then pipette drops onto the cold bottom layers. Some bead suppliers include a surfactant that helps prevent the beads from clumping together. (If the beads lack a surfactant, use the HEPES instead of H<sub>2</sub>O as the buffer for this Gel.) Again, calculate the volume of Gel needed per phantom. The 4.3um beads need a ratio of .025ml to 1 ml of Gel. The 10um beads need a ratio of .050ml to 1 ml of Gel. Mix in the beads as was done for the slurry, using the beads instead of the slurry. After sonicating, quickly pipette the mixture onto the bottom layer of each phantom. Since the volume of the scattering layer is much less than that of the bottom layer, its thermal mass is much less and so will quickly cool to yield the appearance illustrated in Figure 22.



**Figure 22: Bottom+Top Layer (note the dots on the surface)**

A weakness in the design of the phantoms is that the resulting top layer is between 1-7 cell “layers” deep. Some variants of the above phantom were explored in an attempt to reliably construct a single “cell layer.” The first variant placed a thin film of water on top of the top layer. The second variant used a microscope cover slip to squash the top layer flat onto the bottom layer. In both cases, the additional specular reflections from the light of the HSIE tip (from the air-glass-gel interface) made imaging impossible and so were ultimately rejected.

To determine what concentration of beads was to be used, a titration was done to see what ratio of beads would not clump together. The materials and equipment normally used for constructing the phantoms are two pipettes (0.40ul and 1ul), 4 test-tubes, and a 1 litre container for the hot bath. As a form of quality control, the top layer is also applied to a regular microscope slide (see Figure 23), which can then be quickly checked for abnormalities in the beads (thermal damage, etc.) without the need for trying to image the phantom on a microscope.



**Figure 23: Quality-check slide**

The phantoms should be stored for at least a few hours in the refrigerator before use. Phantoms can be stored for up to 3 weeks in the refrigerator before a significant amount of water has evaporated from the gel. For the testing of the HSIE, the phantoms were normally used within 3 days of manufacture. To facilitate titration and other experiments requiring a large number of phantoms, 96 well plates made of black plastic (shown in Figure 24) will be used.



**Figure 24: Black, 96-well plate**

These plates have a clear plastic bottom that we spray-painted black to absorb all light that might reach the bottom of the well.

### **3.2.2.2 Verification**

The model described was verified by micro-dissection and microscopic imaging to verify the layer formation and to ascertain that the beads spread out relatively evenly and did not clump together.

### 3.3 SIMULATION DEVELOPMENT

A model was developed to predict what the HSIE should be seeing for a given target, and then the results were compared to what was observed by the system. Assuming the model is sufficiently accurate, the system can then be improved by exploring parameter changes through the model rather than building a new device each time. The model was tested against the tissue phantoms described above.

#### 3.3.1 Summary of relevant prior work

Dr. I. Bigio, followed by others, has initiated an area of research applying Mie scattering (of nuclei) to determine cell/tissue morphology. Mie scattering is based on predicting the effects of (roughly spherical) scattering bodies on (typically) monochromatic incident light. Since the range of wavelengths that the HSIE is capable of is within an order of magnitude of the diameter of the scattering bodies of interest (cell nuclei), the resulting scattering effects are wavelength-dependent. This wavelength dependence should give a contrast mechanism that should allow one to infer the average size of nuclei that make up a pixel in the resulting spectral cube.

Dr. Bigio's Elastic Scattering Spectroscopy (ESS) approach is a combination scattering and absorption measurement, of which Mie scattering (in particular, the forward-scattering extinction) is a component of the final signal that is analyzed. The ESS approach normally involves a touch probe, where the illumination and collection fibers are located in close proximity. The collected light is then sent to a spectrometer, and then resulting spectra analyzed in a variety of ways (Bigio, *et al.*, Mourant, *et al.*) to obtain classes of spectra associated with

various morphological conditions. These ESS systems have been used in human trials by Dr. Bigio and others, and have achieved high sensitivities and specificities in certain cases.

Some of Dr. Backman's (et al.) research is also related to what this dissertation will be attempting so far as a point-detection modality is concerned. Backman proposes Polarized Light Scattering Spectroscopy (PLSS), where by the reflected signal from cells ex-vivo was split into the parallel and perpendicular components and then subtracted from each other in an attempt to extract the Mie signal from just the surface. In this experiment, broad-band fiber optic white light (450-750nm) source was used to illuminate a 2 mm-diameter circle of the tissue sample, and the light then collected and subsequently split into both polarizations before entering a spectroscope. The resulting spectral data was then combined (with a few fudge factors) to extract the Mie signal. Samples of both cancerous (T84 Malignant cell line) and normal colon tissue were analyzed, and characteristic signals were obtained for each class of sample (cancerous and non-cancerous). These results were verified using microphotographs. The obtained signals were observed to have oscillating components in the spectrum, and it is surmised that these are the Mie components. The PLSS approach differs from the HSIE in the following ways:

- The HSIE uses glass fibers to transmit and collect the light from the target tissue
- The HSIE illumination is a series of mono-chromatic colors, rather than a broad-spectrum "white" light. Additionally, the spectral range of the HSIE is shifted toward the blue, relative to that used by Backman *et al.*
- The PLSS is a pure backscatter measurement, but the incident light was 15 degrees off the perpendicular of the target. The HSIE is a near-backscatter measurement (7 degree separation between illumination and collection)

Gorgekoudi et al., have used PLSS as part of three-modality (autofluorescence, diffuse reflectance, and light scattering) point-probe system in detecting and characterizing cervical pre-cancers in vivo.

### **3.3.2 Mie Scattering Calculation Code**

The Mie code used by the simulation (See Appendix) to calculate the ideal curves was based on the (Fortran code) example given in Bohren's book. This code was converted into an equivalent Matlab program and verified using test parameters and output that were also given in the book. The ideal curves were calculated using a 1nm step size over the entire spectral range of interest for each of the target bead diameters. The ideal curves were then used as input into the optical ray-tracing simulation of the HSIE.

### **3.3.3 Ray simulation**

To predict what the HSIE should "see," several key parameters needed to be determined. The optical geometry of the system at a given distance determines the angles of the scattered light that would be recorded by each imaging pixel of the camera. This simulation calculated the observed intensity of light (either parallel or perpendicular, as appropriate) for all voxels of the target. Using standard optical ray tracing techniques the model estimates the limits of the contributions of each imaged pixel, assuming the sole source of illumination is from the HSIE's illumination fiber. These results are computed for both the perpendicular and parallel parts of the final image (complex values) and then combined yielding a complex result. Taking the magnitude of the result gives the final values one would expect to see.

### 3.4 CLINICAL TRIALS

We developed the entire imaging elastic scattering spectroscopy approach in the hope that, in a not-too-distant future, it can be developed to address unmet needs in the clinic. Specifically, an endoscopic implementation that would improve detection of cancer and pre-cancerous conditions intrasurgically was a logical path to pursue.

An opportunity arose where by joining an existing study, the HSIE system could be used to obtain spectral information from human subjects in the operating room. The existing study was a detailed investigation into both the diagnostic power of Laser Induced Fluorescence Endoscopy (LIFE, Olympus Corp.) as compared to the current (gold) standard, and into the biochemical realm of cell markers for lung cancer. 250 patients (at high risk for lung cancer) were enrolled in the main study, with each patient receiving one or more bronchoscopic interventions that consisted of a diagnosis by use of (a) white-light (gold standard), (b) the autofluorescence-based LIFE imaging system (Olympus Corp.), and (c) intrasurgical tissue sample acquisition for subsequent cell-molecular analysis. We proposed that in addition to the above procedures, *in vivo* data could be collected with the HSIE. After it was determined that this would not negatively influence the main study, University of Pittsburgh Medical Center Internal Review Board approval was obtained to add HSIE onto the original study (See Appendix B for more details).

Patients that were to be imaged by the HSIE were a subset of patients from the main study who were being followed after successful treatment for lung cancer. These patients had failed a subsequent sputum test and were to receive a follow-up endoscopy procedure. For these

(consenting) patients only, the HSIE was also be used to collect spectral information about the biopsy sites. The spectral information could then be correlated with the results reported for the site by Pathology.

## **4.0 RESULTS AND DISCUSSION**

The following sections report and discuss the results of the techniques described in section 3.

### **4.1 PARTICLE SUSPENSIONS**

#### **4.1.1 Construction and test setup**

Standard 5-uL plastic cuvettes (optically clear over the visible light spectrum) were used to hold the material being scanned. The cuvette was placed in a harness (see Figure 25) that allowed the distance from the fiber tip to the 1mm thick wall of the cuvette to be controlled. The scans were performed at 40 degree fiber incidence to avoid specular reflection, at a nominal distanced of 6.5mm such that the 10mm focal point of the optics fell just inside the cuvette wall. The angle between the illumination and collection fibers was 173 degrees (backscattered) light. All scans were repeated 64 times, and then averaged to reduce random noise. Cuvettes were filled with either a 1:50 or a 1:100 dilution of beads and either H2O or Agarose (gel). All beads were initially 10% by weight, and then diluted to the specified ratio. Beads of the nominal diameters of 0.5  $\mu\text{m}$  and 1.0  $\mu\text{m}$  were chosen for this experiment because of the factor-of-two relationship should be apparent in the observed signals.

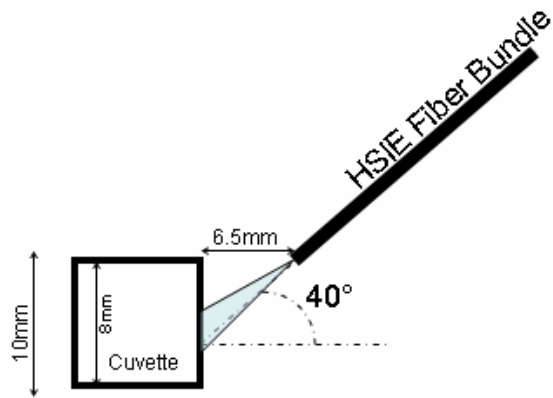
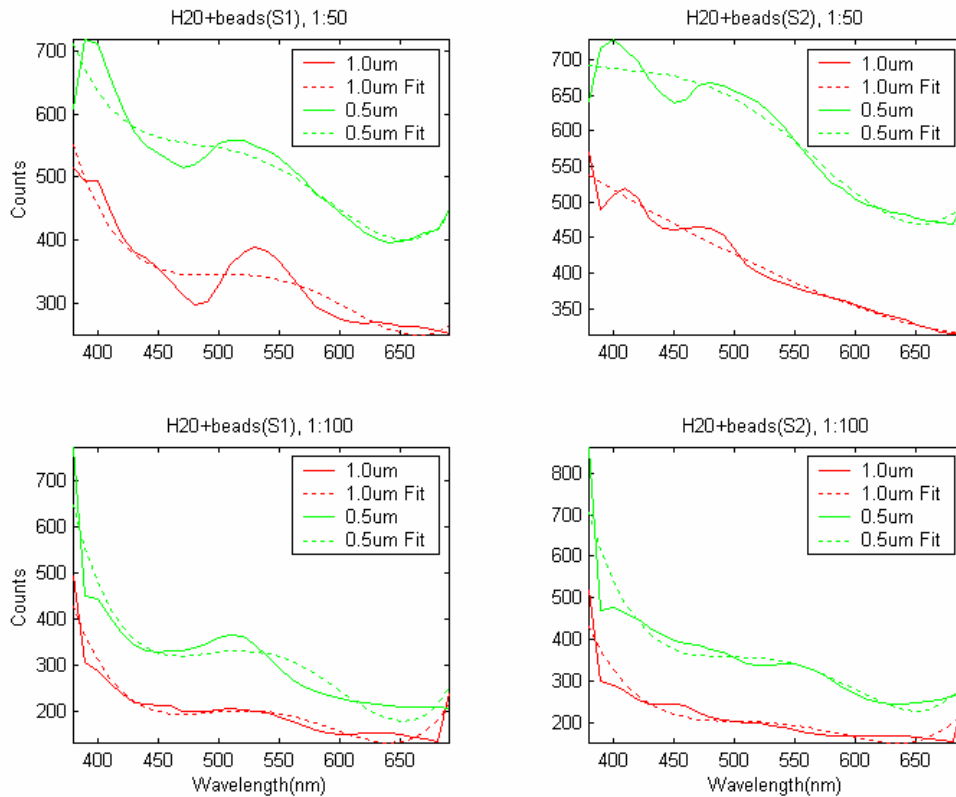


Figure 25: Cuvette data acquisition setup

#### 4.1.2 Results

This first set of figures covers the cuvette-based experimental data, “white” normalized using system-wide averaged spectra.



**Figure 26: comparison of H<sub>2</sub>O+beads at two concentrations**

From a physics point of view, the S1 (parallel) component contains information about both the surface of material and the deeper layers, while the S2 (perpendicular) component just contains information about the deeper layers. Figure 26 compares H<sub>2</sub>O+beads at the two concentrations, showing both the parallel (S1) and perpendicular (S2) signals obtained. The dotted lines represent a 3<sup>rd</sup> order polynomial fit to the signal to compensate for unknown scattering events as well as emphasize the oscillatory signal. First, it should be observed that there is in fact an oscillatory signal, and that it differs for different diameters. Second, there is a rough factor-of-two relationship in the count intensities, commensurate with the factor-of-two dilution relationship. Using the polynomial fit to extract oscillatory part of the signal yields interesting

patterns in the Fourier domain. The use of the Fourier Transform in analyzing single scattering events is common in the literature, and more recently has been termed Fourier Transform Single Scattering Spectroscopy (FTSSS) by Amelink, *et al.* The following four figures comprise K-space plots (commonly used in chemistry applications) make the oscillations clearer to the eye, accompanied by a fast-Fourier transform (FFT) of the signal. The top part of the plot is the residuals (deviation) from the curve fitting, and the bottom part is the FFT of the same data. The peaks in the FFT should correspond to the diameters of the beads.

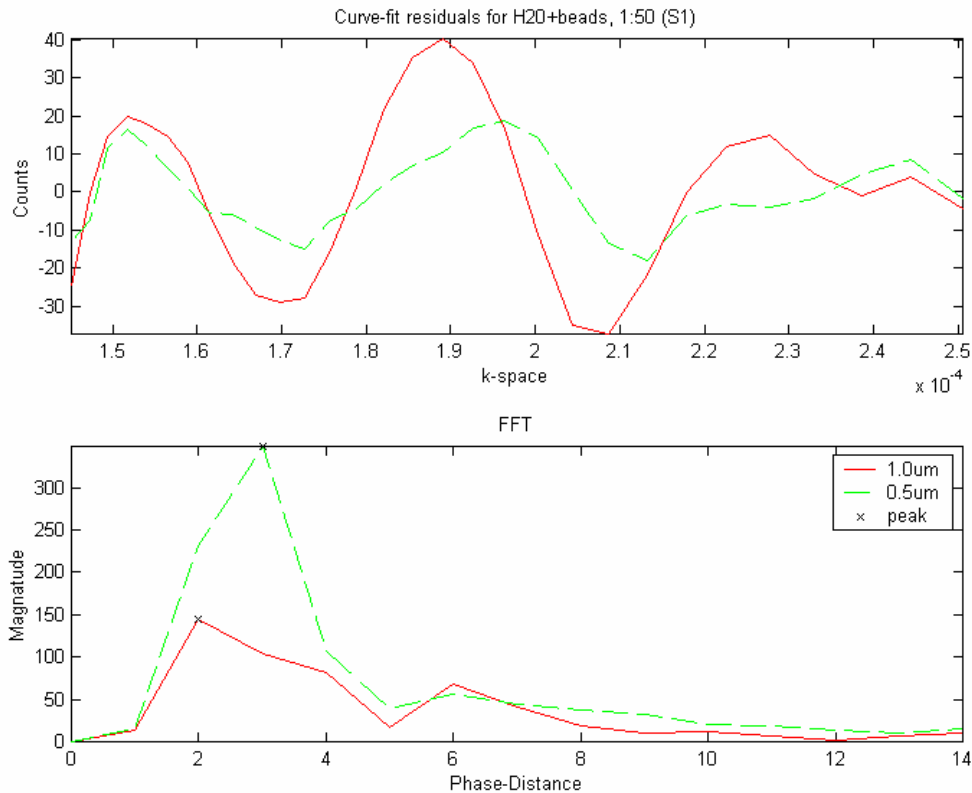


**Figure 27: S1 signal for H2O+beads at 1:50 dilution**

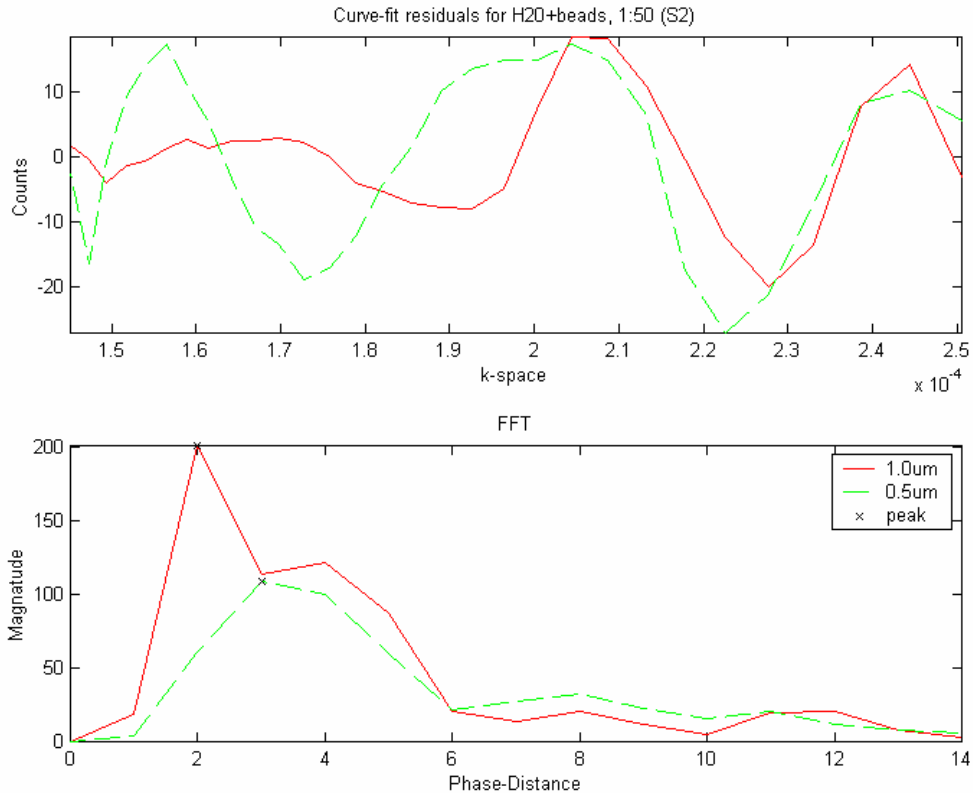


**Figure 28: S2 signal for H<sub>2</sub>O+beads at 1:50 dilution**

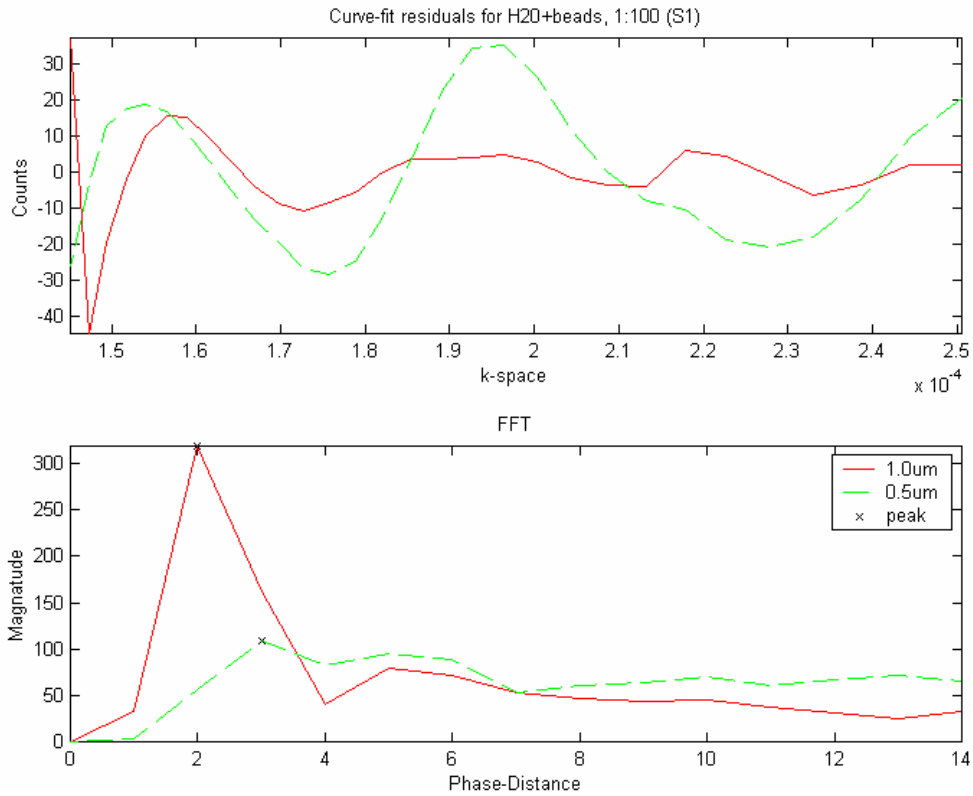


**Figure 29: S1 signal for H<sub>2</sub>O+beads at 1:100 dilutions**

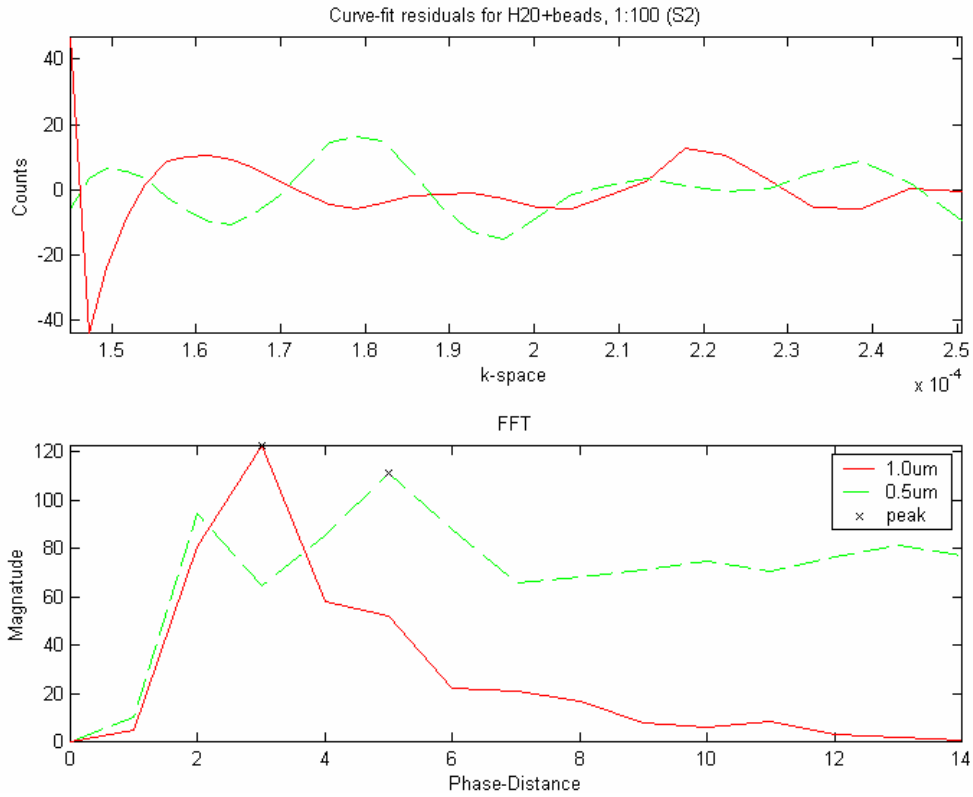


**Figure 30: S2 signal for H<sub>2</sub>O+beads at 1:100 dilutions**

It should be noted that as the dilution increases the signal gets weaker the amplitude of the oscillations also get weaker, but the peaks at integer phase-distances remain unchanged for the corresponding signal (either S1 or S2). This next set of figures compares the signals for a 1:100 dilution of beads suspended in either H<sub>2</sub>O or Agarose (AGR).

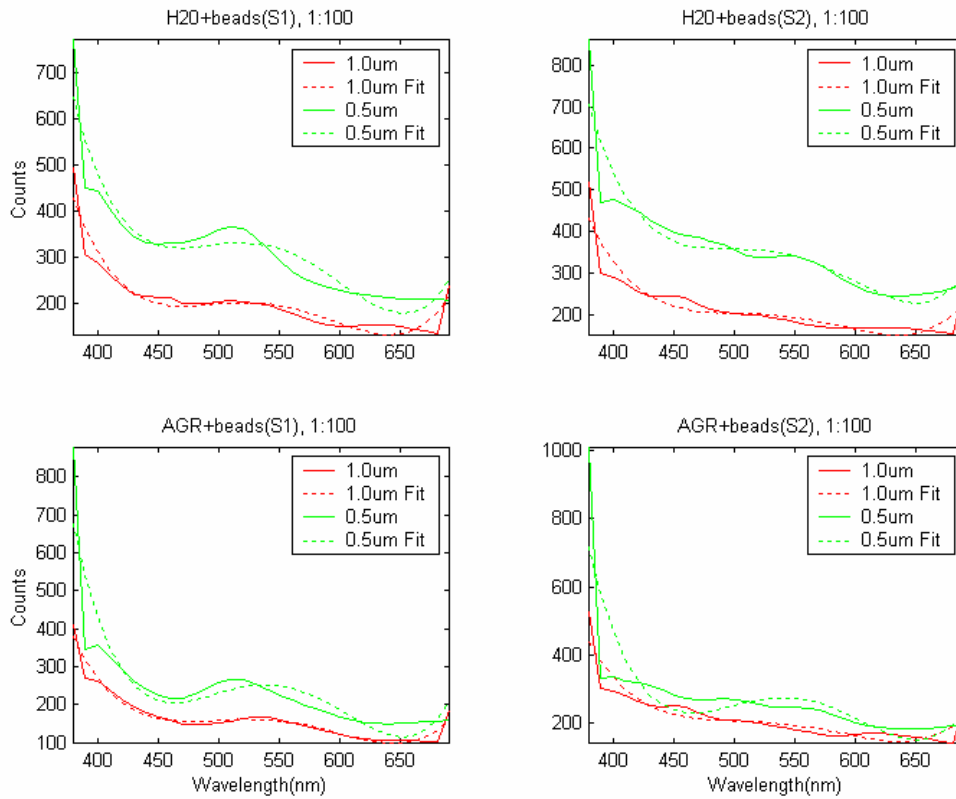


**Figure 31: Comparison of beads and either Agarose or H<sub>2</sub>O at 1:100 dilution**

As expected, the amplitude of the signal is further reduced by the switch to Agarose (change in relative indices of refraction). This amplitude reduction makes the FFT analysis tougher in the case of Agarose suspensions, but the peaks are still distinguishable, as shown in the next two figures.

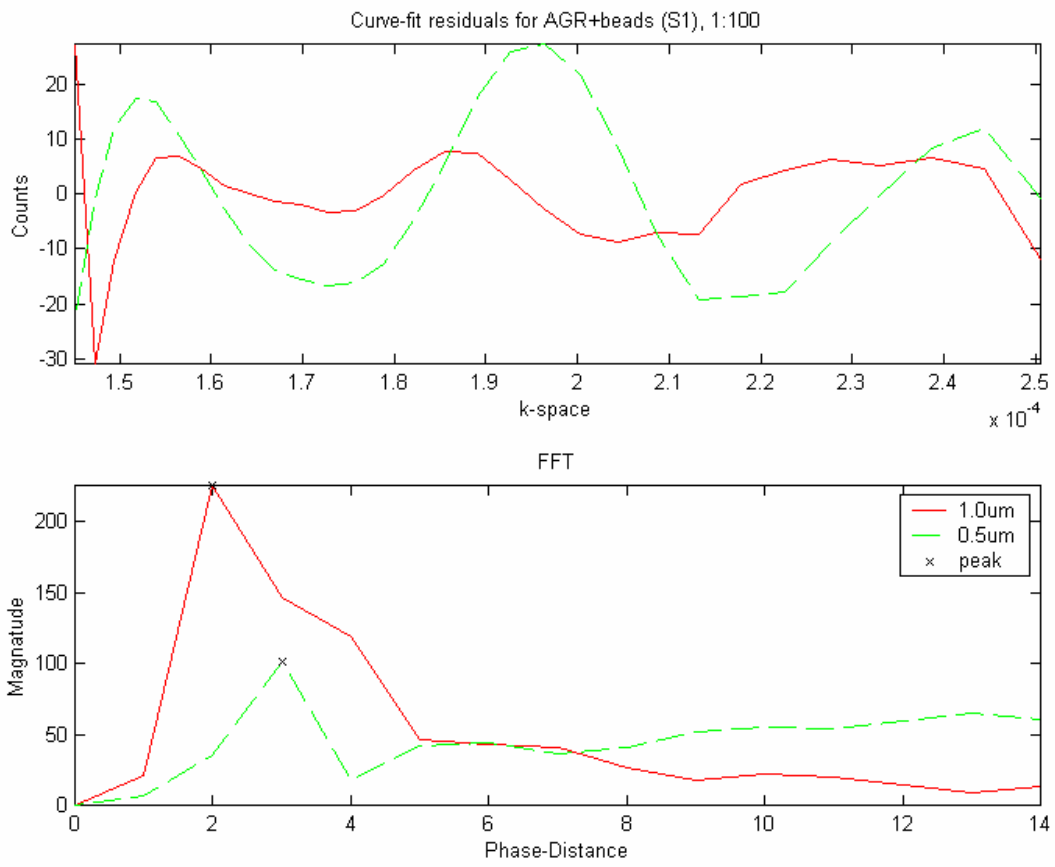


**Figure 32: S1 signal for Agarose+beads at 1:100 dilutions**

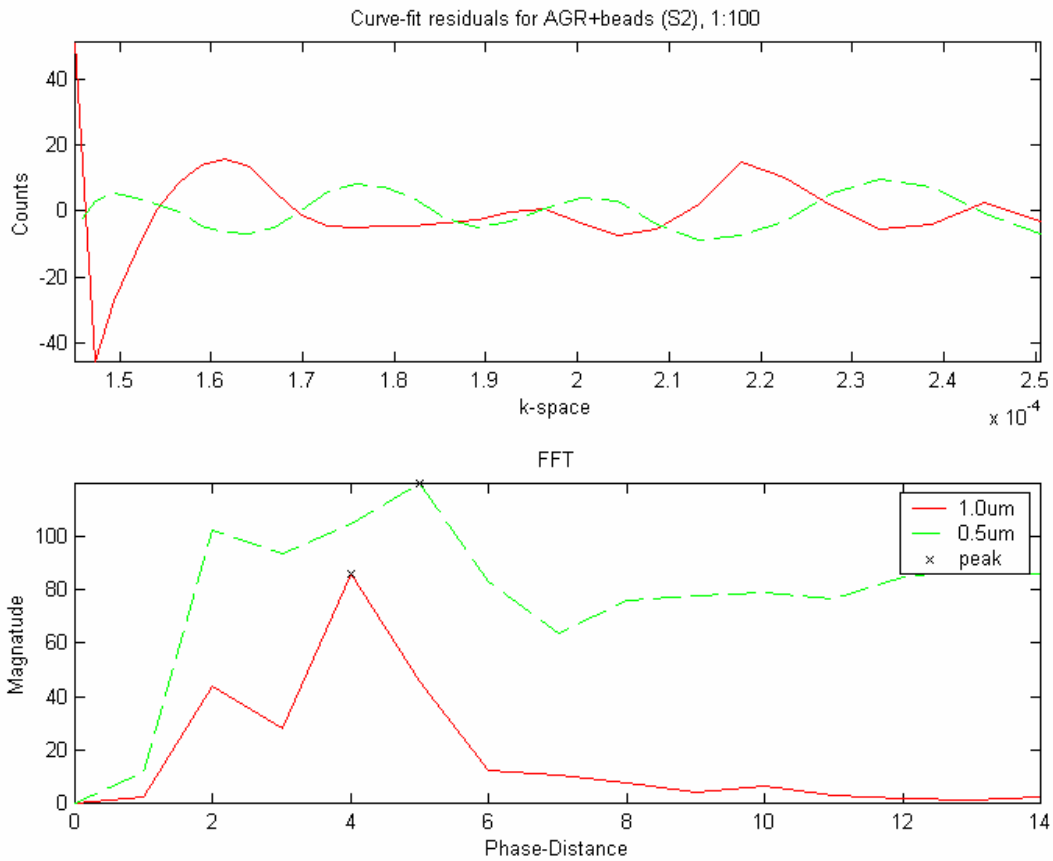


**Figure 33: S2 signal for Agarose+beads at 1:100 dilutions**

The results for Agarose have the characteristic peaks continue to appear in the S1 signal. The S2 signal exhibits some unexpected shifting which may be due to a variety of factors, including low sampling, or simply noise from the low signal. While the phase distance does not exhibit the desired factor-of-2 dependence, this may be simply a sampling resolution error, but it may also be from the fact that an average system response was used instead of a pixel-by-pixel response. This possibility will be explored in the next paragraphs.

For the pixel-by-pixel white normalization, a Spectrolon™ target was used to provide pixel-by-pixel white normalization curves for the entire field of view of the HSIE. In the case of tissue phantoms, we are only interested in the surface of the phantom. Intuitively, the parallel-to-

the-scattering-plane signal contains information from the surface + depolarized information from the deeper structures. The perpendicular-to-the-scattering-plane signal contains information from deeper structures that we have little interest in. Theoretically, one can be subtracted from the other, leaving just the information about the surface. In engineering practice, this is difficult to achieve proper cancellation due to light collection issues (the scattering planes for each imaging bundle are technically not the same, imaging bundle alignment, lens alignment, etc.) and parallax issues. With regards to the phantom data, performing the subtraction made things significantly worse, not better. Thus, the results presented here will be limited to the S1 signal.

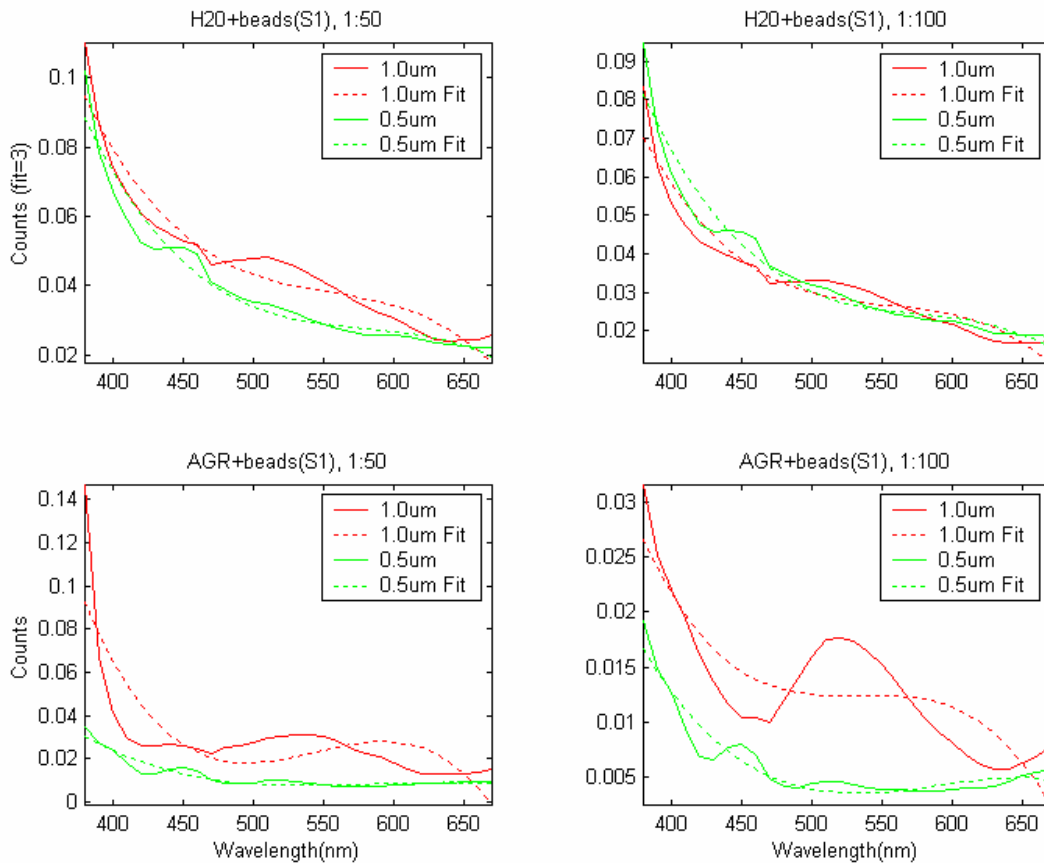


**Figure 34: S1 signals for tissue phantoms at 1:100 bead dilutions**

Applying to the results in Figure 34 the same procedure used for extracting the signals in Figure 31 yields the following 4 figures.

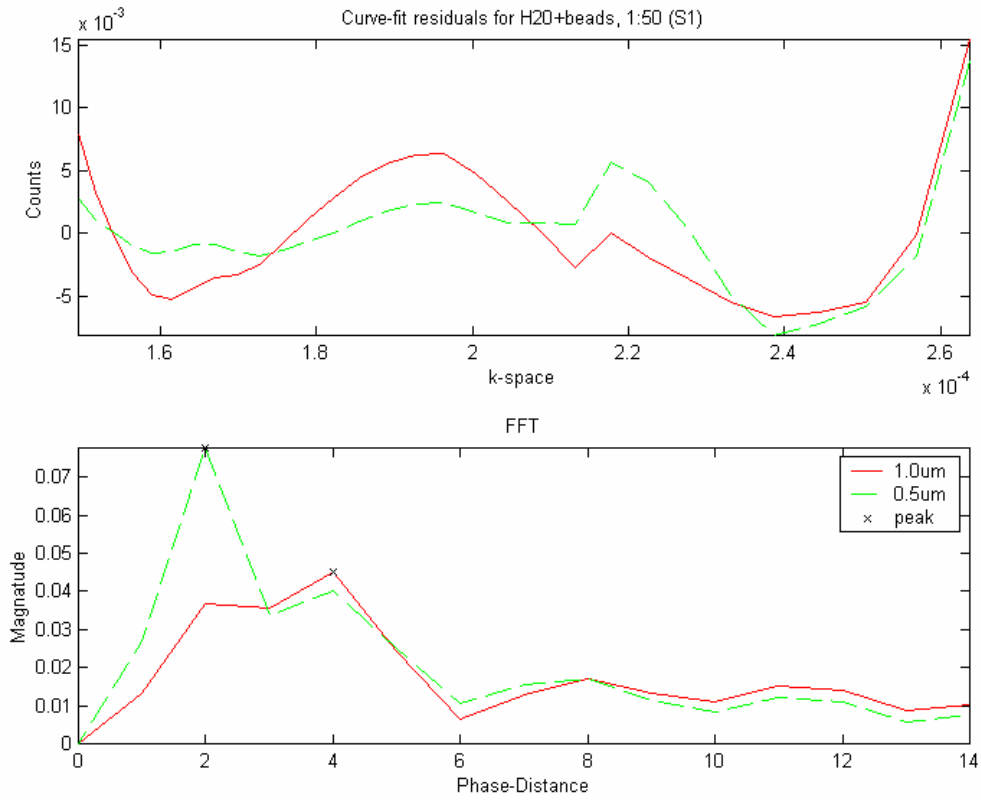


**Figure 35: New S2 signal for H<sub>2</sub>O+beads at 1:50 dilutions**

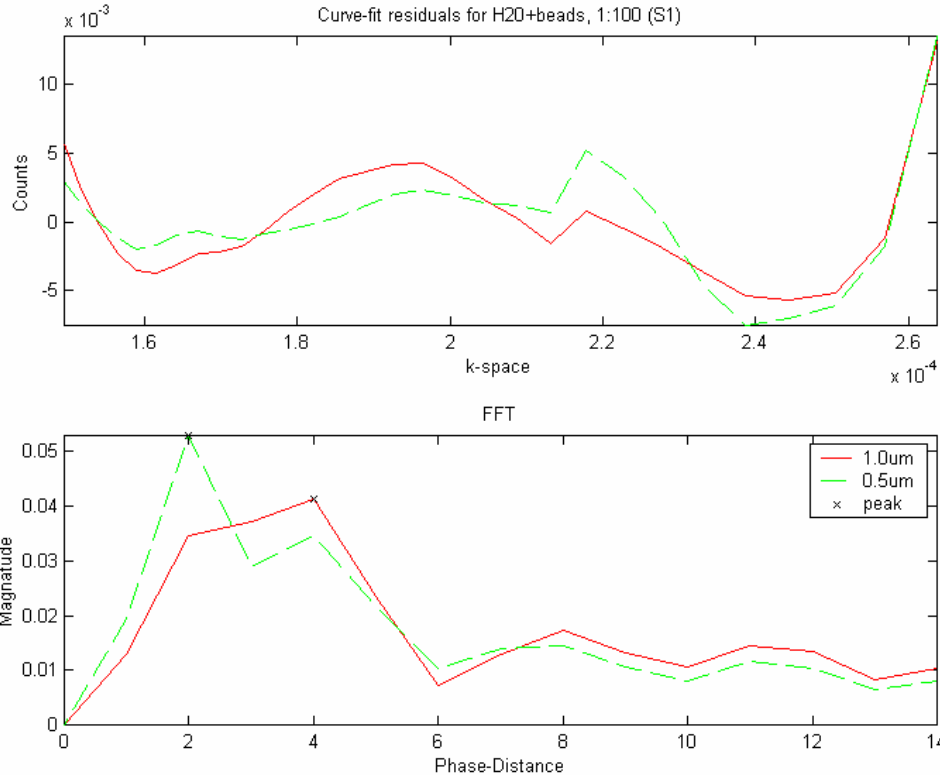


**Figure 36: New S1 signal for H<sub>2</sub>O+beads at 1:100 dilutions**

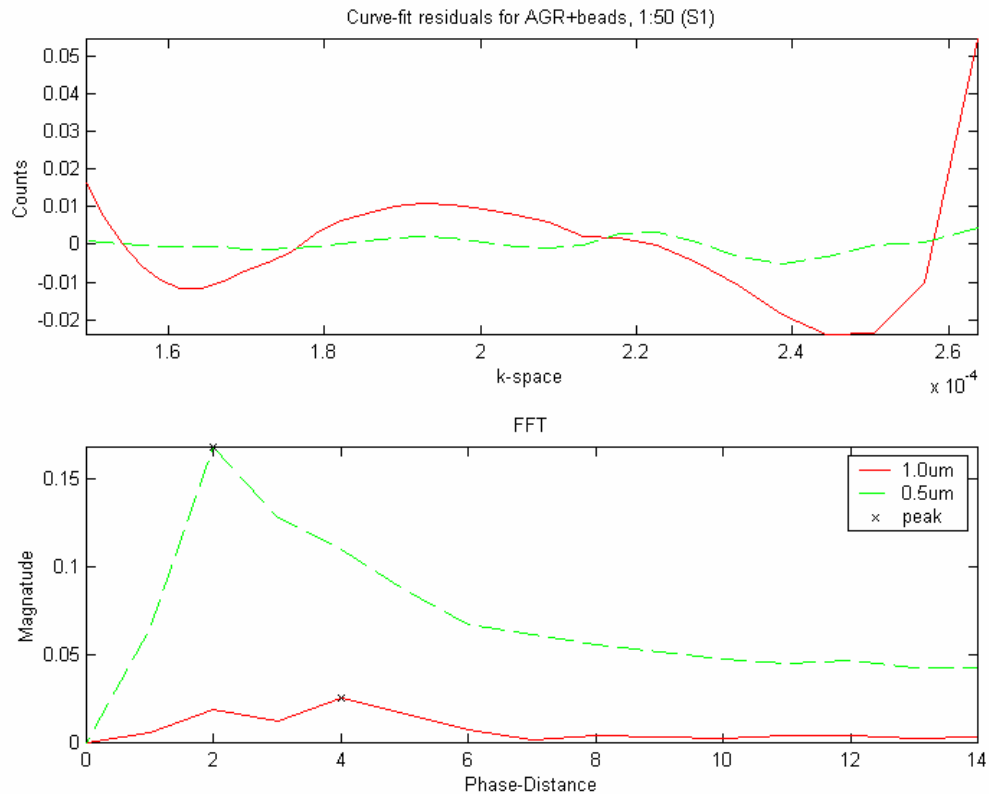


**Figure 37: New S1 signal for H<sub>2</sub>O+beads at 1:50 dilutions**

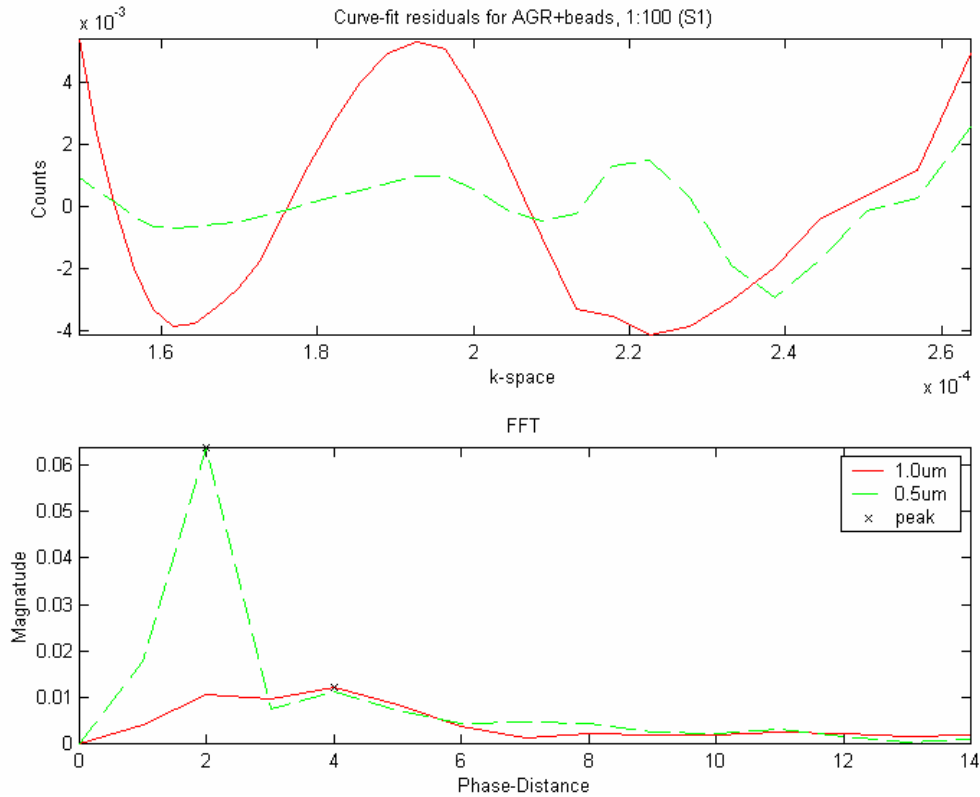


**Figure 38: New S1 signal for Agarose+beads at 1:100 dilutions**

The most significant difference here is that the peaks are now located consistently at a phase distance of 2 and 4, as opposed to the previous 3 and 4 (again, integer rounding error is the most likely culprit). The new peaks now have the factor-of-two relationship that was expected, and the signal amplitudes are slightly greater, leading to the conclusion that the pixel-by-pixel white normalization is necessary to reliably extract the Mie signals.

To summarize, it is possible to distinguish the beads from each other using FFT to find distinctive signal peaks. However, the spectral resolution of the HSIE is not sufficient to obtain clear separation of the peaks. Furthermore, the signal-to-noise ratio of the observed signals is low, and this will make detection and interpretation more difficult as we move on to the more complicated physical models (tissue phantoms).

## 4.2 BEAD-BASED TISSUE PHANTOMS

### 4.2.1 Construction

Using titration, a dilution of 1:80 for 4.3  $\mu\text{m}$  and a dilution of 1:40 for the 10  $\mu\text{m}$  beads (using HEEPS as an anti-clumping agent) was found to yield virtually clumping-free distributions of beads. However, real epithelial tissue has a tighter packing (with no clumps) than could be achieved with the beads.

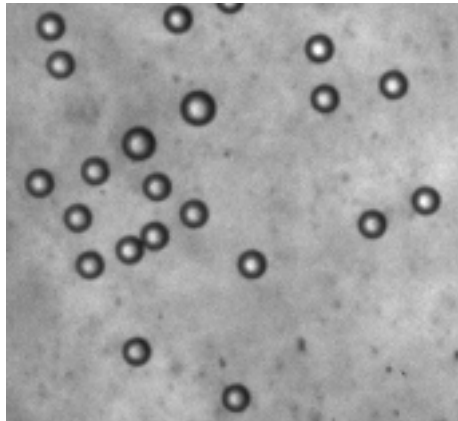


**Figure 39: Microscopic image of the top layer of a 10um-bead phantom (with one “diploid”)**

Figure 39 shows a microscopic view of the top layer of a 10um-bead phantom, viewed from the direction that the HSIE would be imaging using a 40x air objective. There is virtually no clumping, with only the occasional “diploid cell”-like touching of two beads. These “diploid” items could have been eliminated/neglected, but instead they were retained here as a representation of a dividing cell.

#### 4.2.2 Microscopic Imaging of Tissue Phantom to Verify Known Structure

For the first verification, two-layers were checked for through the excision of a small sliver of a phantom, which was placed on a slide and then imaged. Figure 40 was the result, using a 5x air objective.

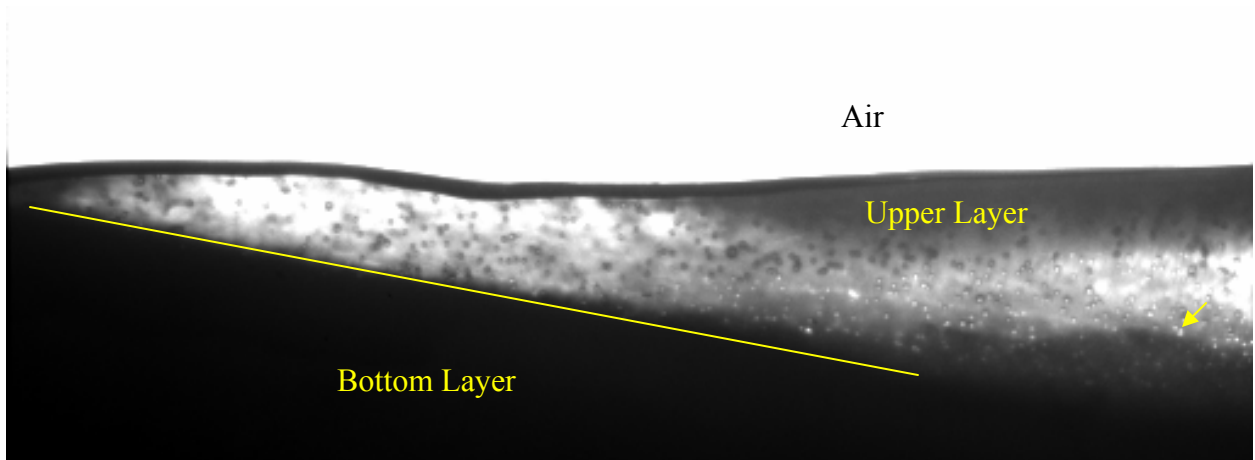


Figure 40: Side view of a 10um phantom

Looking at the cross-section of part of the phantom, the air, upper layer, and bottom layer have been labeled in the image, and a yellow line approximates the border between the upper (beads) and lower (scattering) layers of the phantom. The arrow indicates a 10um bead in the upper layer.

#### 4.2.3 HSIE Verification

For the second verification, a 96-well plate was prepared with several different phantoms in certain patterns. For each pattern, X=1.0  $\mu\text{m}$  bead phantom, Y=0.74  $\mu\text{m}$  bead phantom, and Z=0.5um bead phantom. In the patterns, data was collected at a 40 degree incident like in the

cuvettes (see Figure 25) to avoid specular reflections. The scans were repeated 64 times, and then averaged to remove noise. All data has been adjusted to a camera exposure time of unity.

**Pattern #1 Results**

The goal of this pattern (Figure 41) was to test how increasing the top layer concentrations affect the results:

<b>Bead Concentrations</b>	<b>1:25</b>	<b>1:50</b>	<b>1:100</b>
<b>Beads</b>	X	X	X
	Y	Y	Y
	Z	Z	Z

**Figure 41: Bead layer concentration test grid**

Each well was scanned individually, and the results summarized below. Curves were taken from the optical center of the imaging field of view.

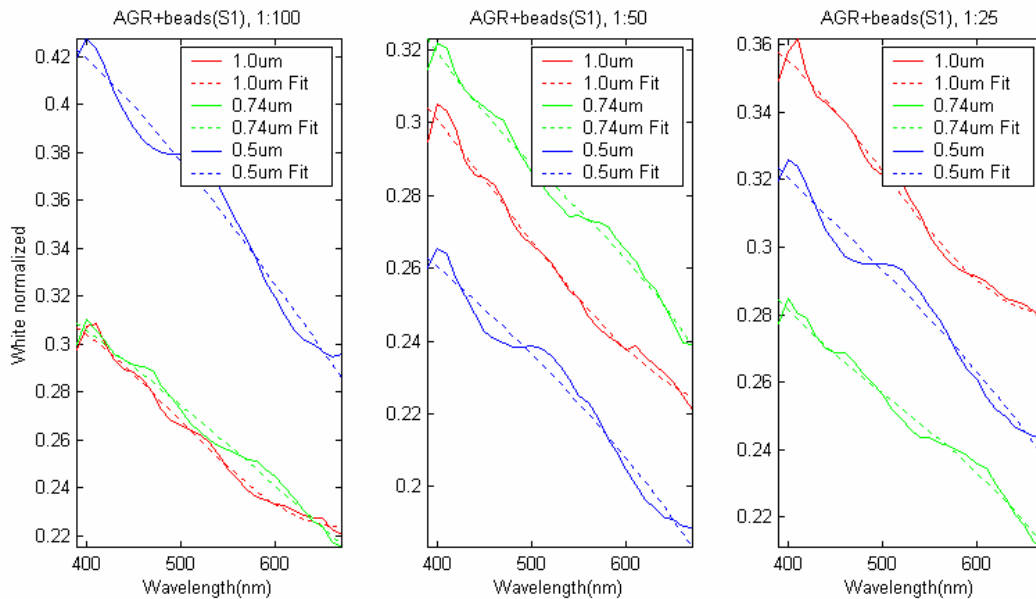


**Figure 42: Top (bead) layer titration signals showing White normalized signals vs. Wavelength(nm)**

The above figure shows the actual signal observed, with the dotted line polynomial fit included for clarity. These signals have a certain consistency as the concentration of beads is varied (shown in Figure 43), which is a desirable result.

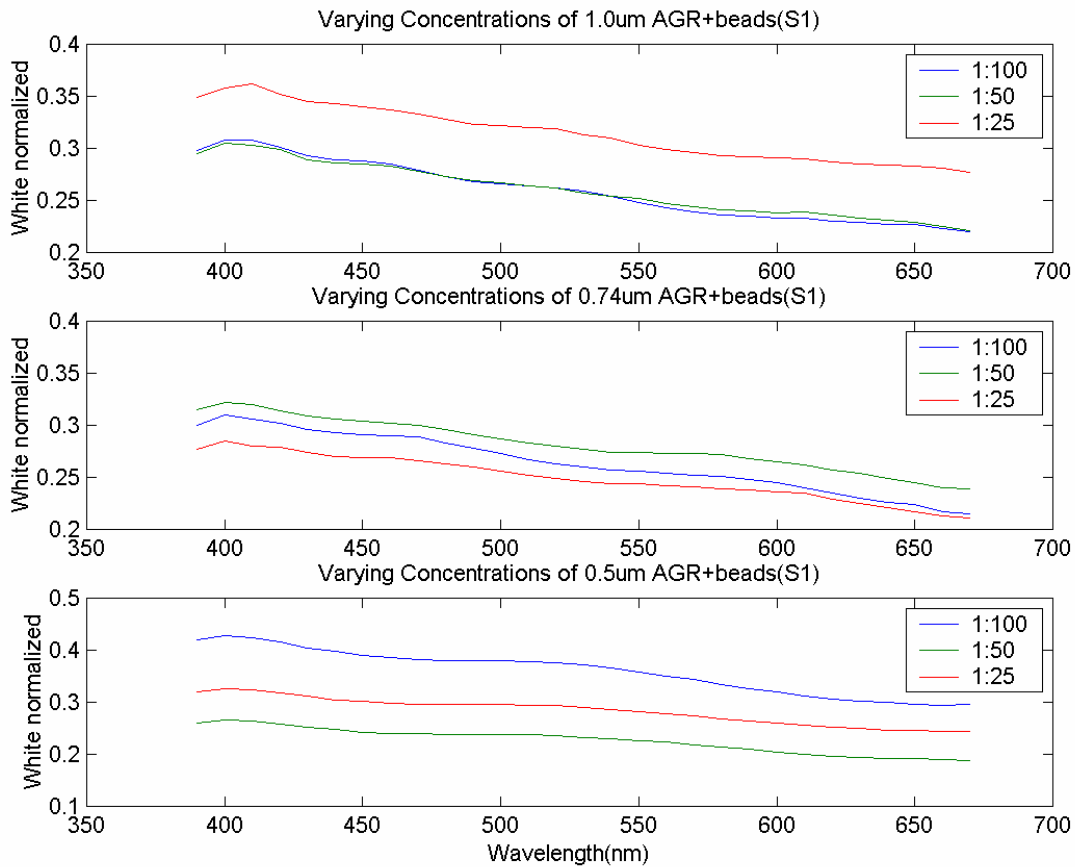


**Figure 43: Comparison of top (bead) layer signals by bead size**

Figure 43 groups the signals by bead size, and the signals are similar for each level. The magnitude of the separation for each concentration signal is not consistent, but this lack of consistent separation does not affect the subsequent signal extraction.

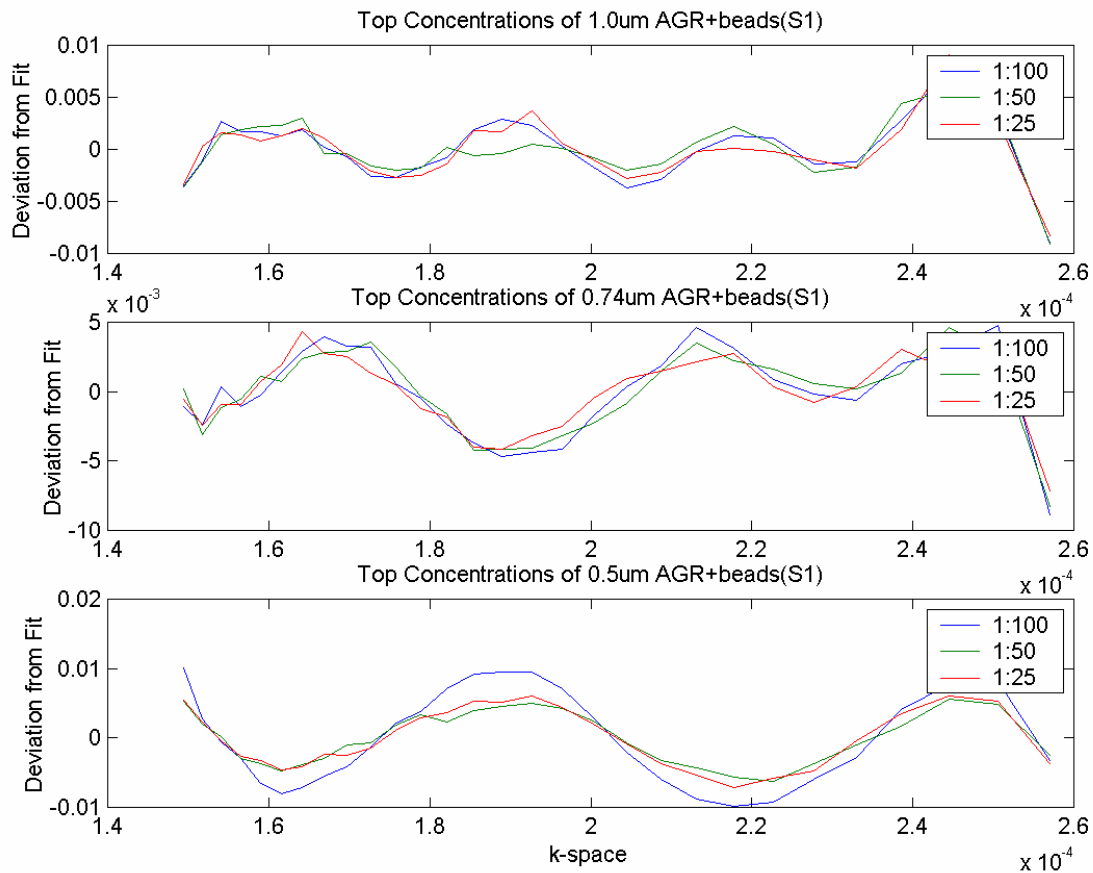


**Figure 44: Comparison of top (bead) layer signal deviation of fit**

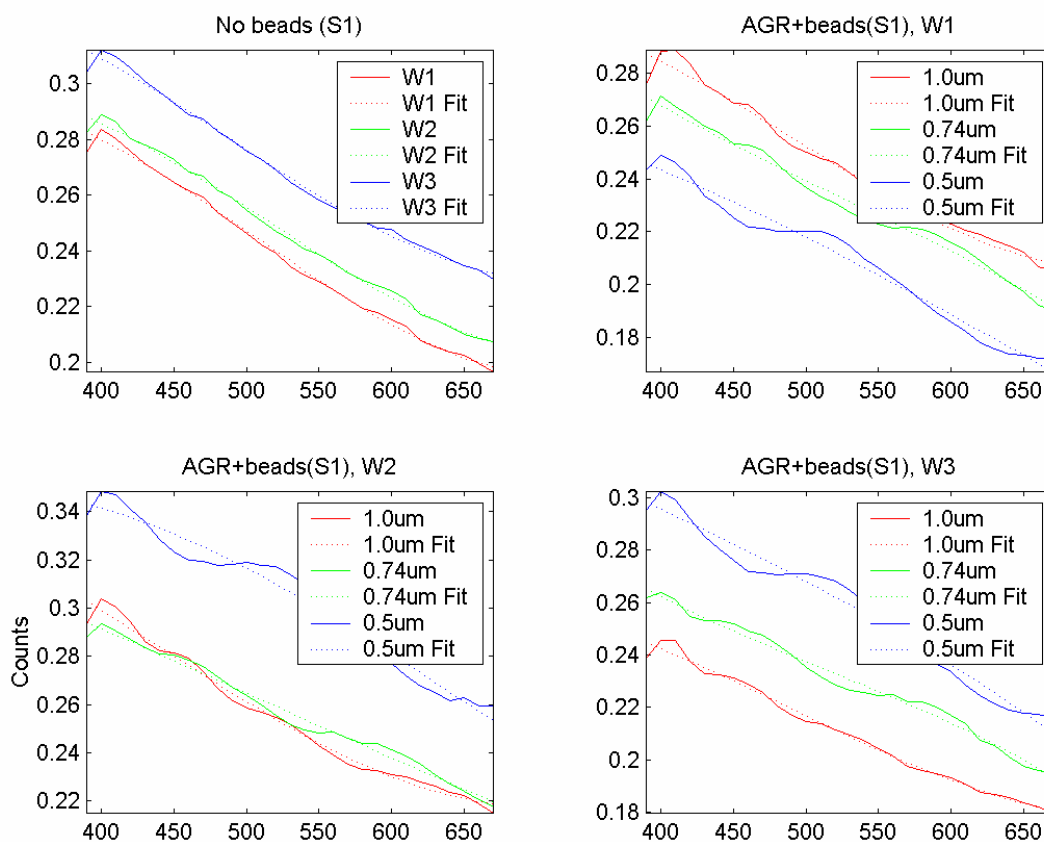
This final figure of the set (Figure 44) shows that the differences in the concentration of beads does not seem to significantly affect the signal, and that the signals can be differentiated at all concentrations. Furthermore, the top plot has roughly 4 signal peaks, the middle plot has roughly 3 peaks, and the bottom plot has roughly two peaks. This is consistent with the factor-of-2 difference between the top and bottom bead diameters, and the factor-of-1.5 relationship for the middle plot. To summarize, while the concentration of beads does affect the signal-to-noise ratios, it does not significantly affect the observed oscillatory signature.

## Pattern #2 Results

The goal of this pattern (Figure 45) was to test the how increasing the bottom scattering layer concentration affects the results:

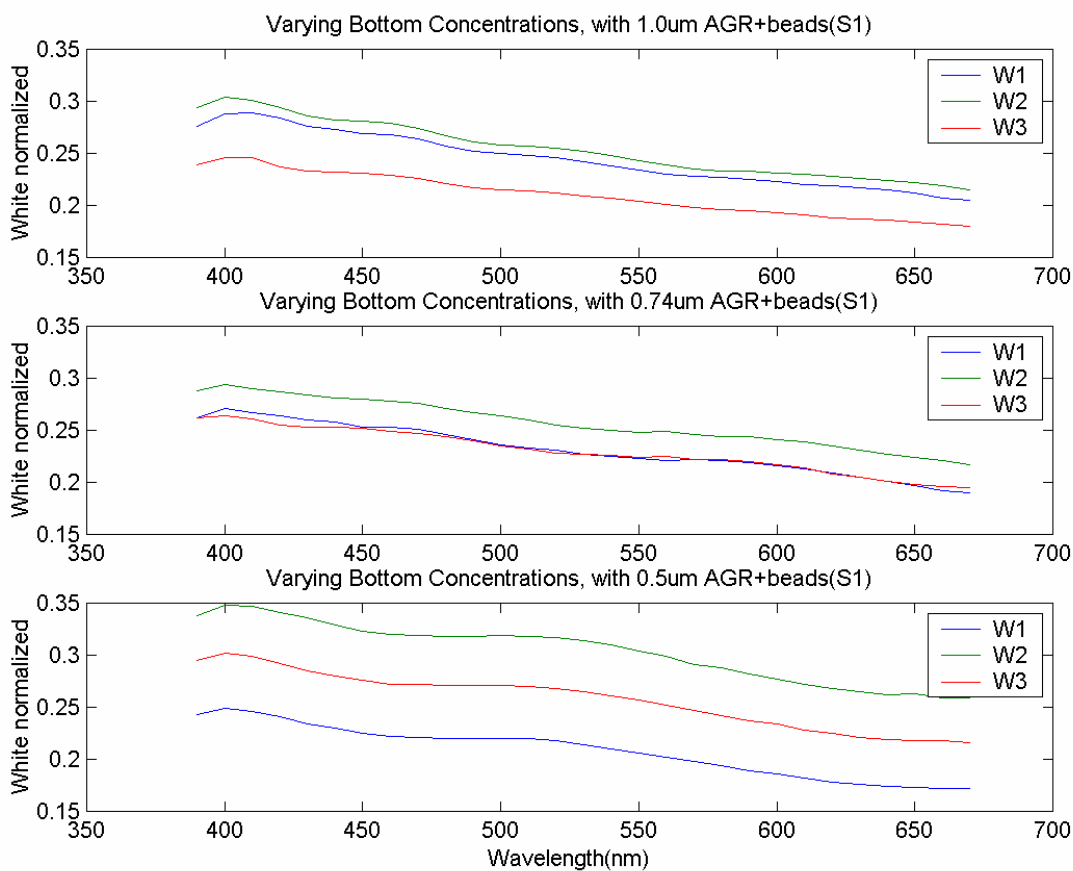
Background Concentrations	1	1.5	2
Beads	X	X	X
	Y	Y	Y
	Z	Z	Z

**Figure 45: Bottom layer concentration test grid**



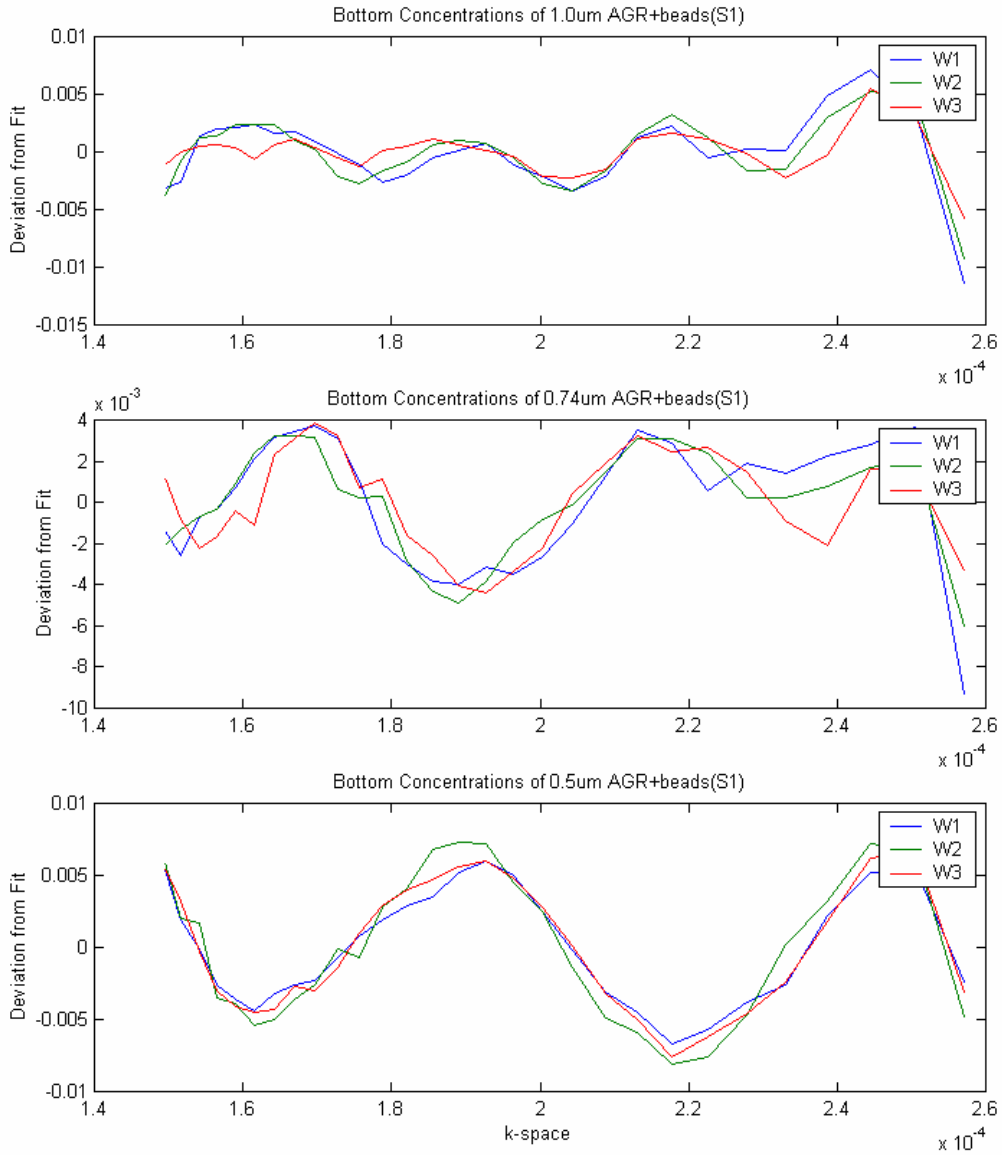
**Figure 46: Bottom layer titration signals**

Figure 46 is a summary of signals observed from the three concentrations (W1, W2, W3) of the bottom layer scattering components (16 mg, 24 mg, and 32 mg of  $\text{TiO}_2$  respectively). The upper left plot shows that there is no oscillatory signal contribution from the bottom scattering layer. The remaining three plots show the observed signal for each of the three concentrations, grouped by the bottom layer concentration.



**Figure 47: Comparison of signals by bead size**

Figure 47 groups the observed signals by bead size, and as was seen in Figure 43, there is not a consistent magnitude shift depending the concentration changes. Extracting the oscillatory components, as before, yields the following:



**Figure 48: Comparison of bead signal deviation of fit for a given bottom layer**

Observations that were made for pattern #1 can be also applied to the results in Figure 48, so to summarize the results of Pattern #2, the influence of the concentration of the TiO<sub>2</sub> bottom layer seems to be minimal on the S1 signal. This is consistent with the known physical fact that the S1 signal is comprised primarily of information about a depth of only a few wavelengths (for each color of light).

### **Pattern #3 Results**

The goal of this pattern was to test the ability to spatially resolve areas of different sized of beads. This pattern was a 3x3 grid with X and Z arranged in the shape of the letter “C”:

X	X	X
X	Z	Z
X	X	X

**Figure 49: "C" test pattern**

It was initially thought that only a 3x3 grid would be able to be seen by the optics of the HSIE, but in fact, only 4 wells were able to be successfully focused upon. Consequently, only a 2x2 section (XZ;XX) and a 1x2 section (XZ) of the grid were in fact imaged. Also, a separate phantom for each X and Z were also scanned to be used as classifier validations. The images were then analyzed pixel-by-pixel, and a false-color image based on the dominant oscillatory component of the spectra was generated.

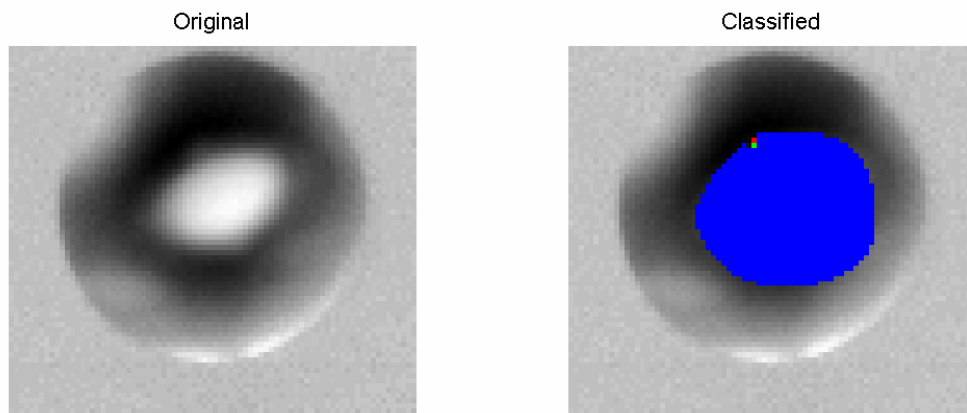


**Figure 50: Test for Z classification**

For the Z classification, the signal was fairly reliably classified, but a couple of pixels at the top were misclassified. The signals from the surrounding areas were too weak to be confidently classified.

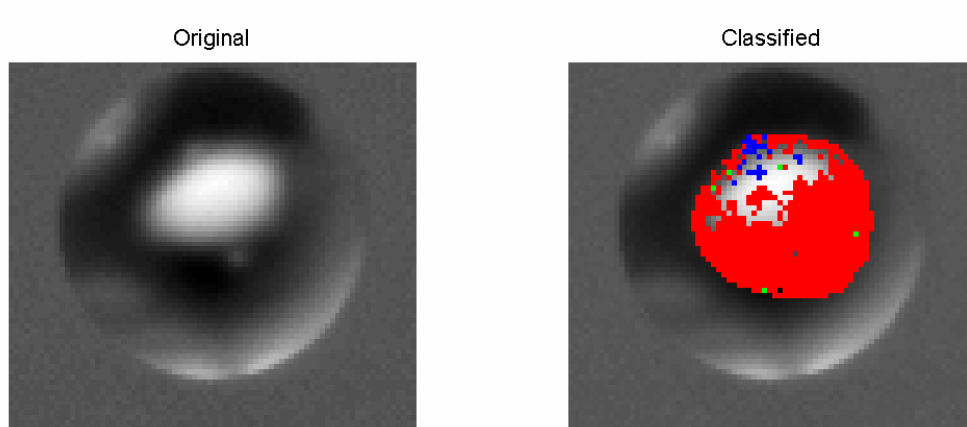


**Figure 51: Test for X classification**

In the case of the X classification, some of the signals in the center field of view were too weak to be confidently classified ( $\text{SNR} < 1.2$ ).

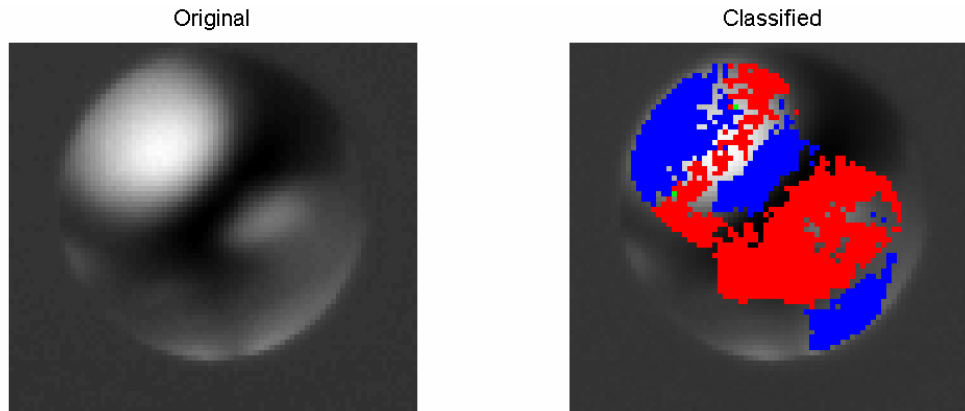


**Figure 52: 2x1 grid classification**

For this test, the upper left region should be blue, and the lower left region should be red. Again, signal strength was a big factor in confusing the classifier.

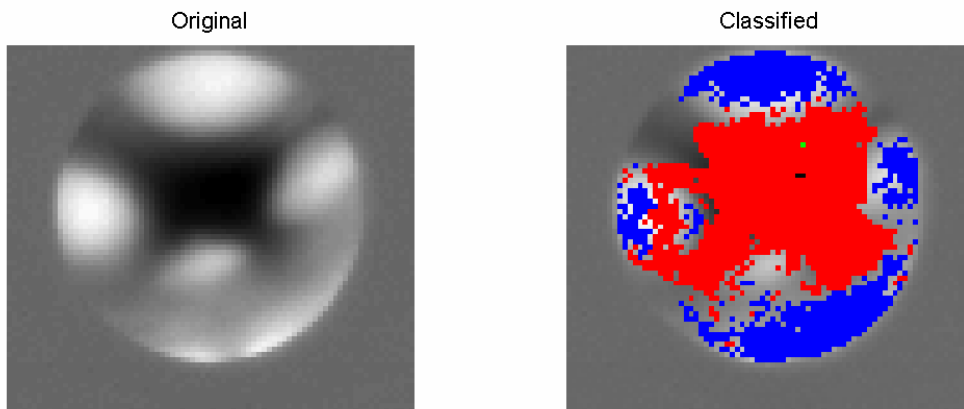


**Figure 53: 4x4 classification**

In this test, the bottom area should be red, and the top, left, and right regions should be blue. The center area is the flat-black plastic that separated the wells, and should not have been classified as either red or blue. There is a serious parallax effect evident in this image, and this violates on the previous assumptions that there is no significant change of distance over the field of view.

The results from the above figures were not as strong as expected. Some possible reasons for these unexpected results are:

- Beads were not of sufficient depth/density to generate a strong signal
- Scattering layer is “too efficient”, destroying the signal
- Light was insufficient in intensity generate a strong signal
- Spectral resolution of the system is too low (resulting in few points for the FFT)

The above images demonstrate that it is possible to detect different beads diameters in an imaging modality, the signal is very weak and suffers from this fact in a variety of ways. Furthermore, the distance and parallax issues cannot be ignored.

### 4.3 SIMULATION OF HSIE

For the model, it was assumed that the target being observed was in focus and consisted of only one size of beads that were uniformly distributed throughout the image volume. The first stage of this model estimated the angles between the illumination fiber and the imaging fibers, taking into account the numerical apertures of each. As the distance increases, the number of fixed-sized points of the target that are visible increase as would be expected. It should be noted that the tip optics have a focal length of 10mm (third set from the top), and that the calculations do not include the fact that at other distances the lenses will be out of focus. If the model were to stop at this point it would yield the following “predicted images” using the polarity calculation (for 1.0 $\mu$ m diameter):

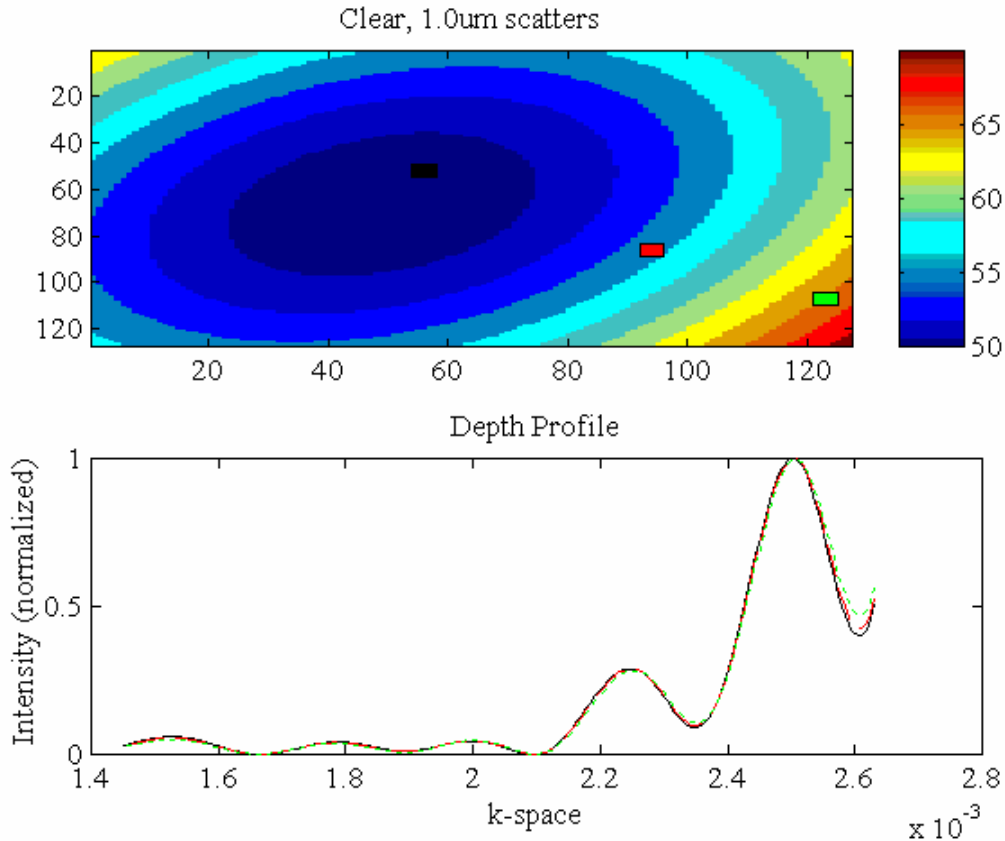


**Figure 54: Ideal HSIE view for 1.0µm (intermediate result)**

Referring to Figure 54, the top part of the figure is a spatial image view of the ideal “target.” The overlapping, disk-like contours arise from a combination of the two points of view (parallel and perpendicular imaging fibers) and the angular step-size of the curve library (0.1 degree). The bottom part of the figure is a graph of three distinct areas taken from the spatial image. These areas were chosen to illustrate how the signal can change through the field of view. The colored boxes correspond to the location of each curve in the image: the center (black, solid line), the lower right hand corner (green, dotted line), and half-way in between (red, dashed line).

However, the model does not stop there and instead continues by estimating the limits of the contributions of each imaging pixel by integrating over both the solid angle of the illumination

fiber (NA=0.45) and the solid angle of the imaging fiber's lens (NA=0.35). These results are computed for both the perpendicular and parallel parts of the final image and then combined using the polarity calculation. The model was further increased in its complexity with the inclusion of the fact that the light source used for the current HSIE has a mean 10 nm bandwidth. Assuming a uniform sampling over the useful range of the HSIE, incorporating this 10 nm bandwidth of the illumination into the model yields some interesting results, shown in Figure 55.

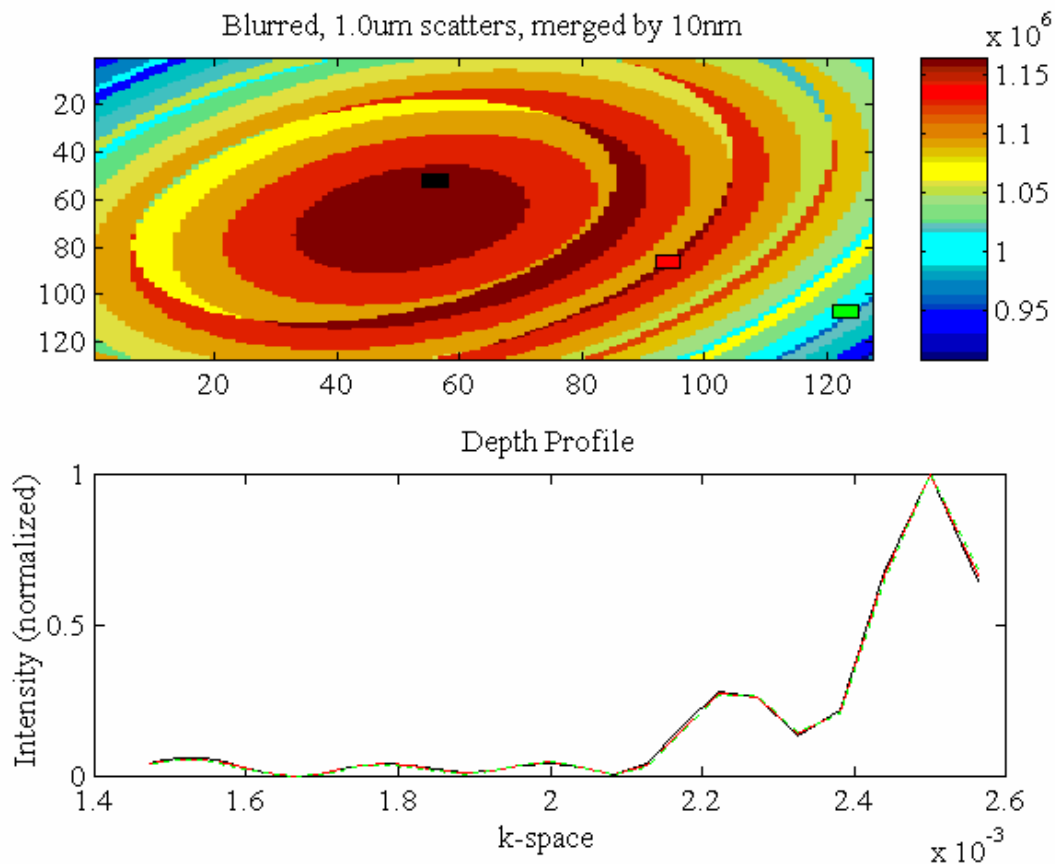


**Figure 55: 10um scatters, with a 10 nm illumination bandwidth and uniform sampling of the spectra**

In essence, the wide 10nm bandwidth of the light is smoothing out the scattering signal that we are looking for, and then sub-sampling it. Scattered signals are not as intense as the original light, and so to increase the power of the observed signal, it is possible to select an angle for which the

reflected signal would be strong for which both signatures were somewhat orthogonal (to maximize the distance between the classifiers). Figure 56 and Figure 57 examine the wavelength-angle topology (backscattering only) in different scales for the beads used in the phantoms (0.5  $\mu\text{m}$  and 1.0  $\mu\text{m}$ ):

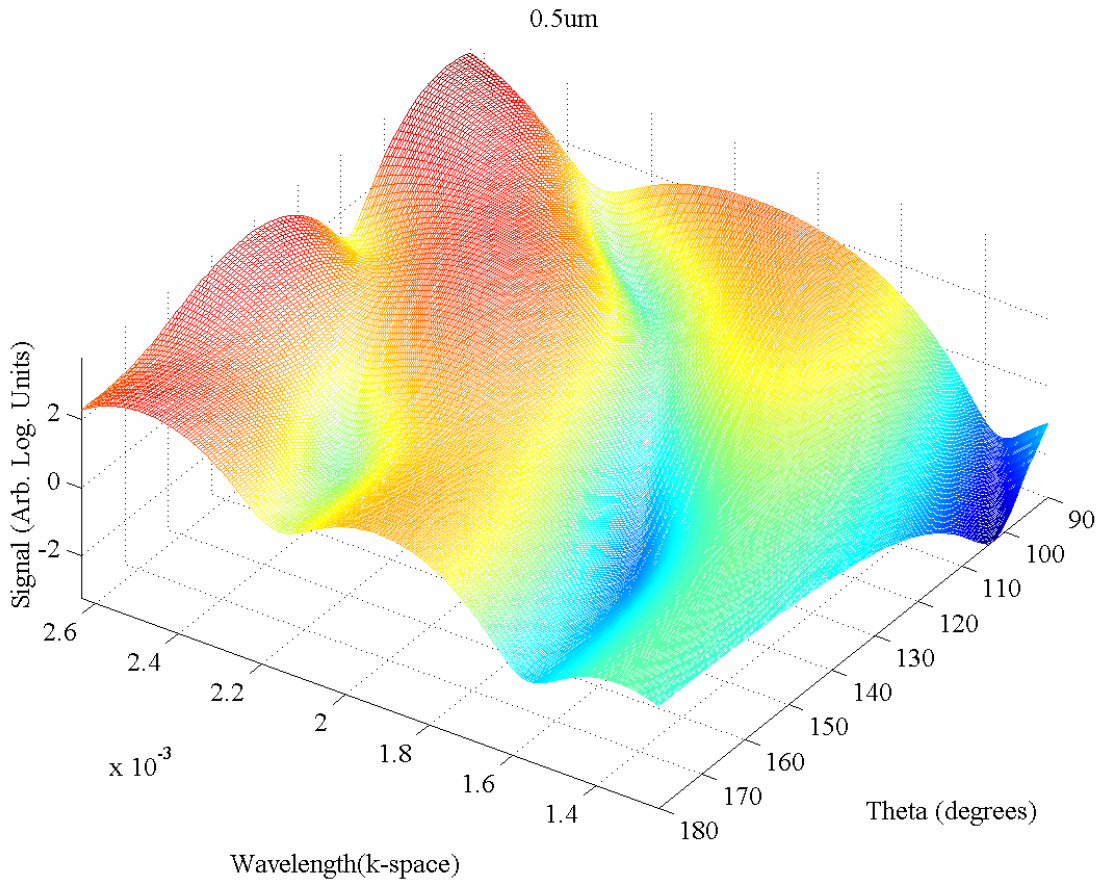


**Figure 56: Wavelength-angle topology for 0.5 $\mu\text{m}$  (90-180 degrees)**

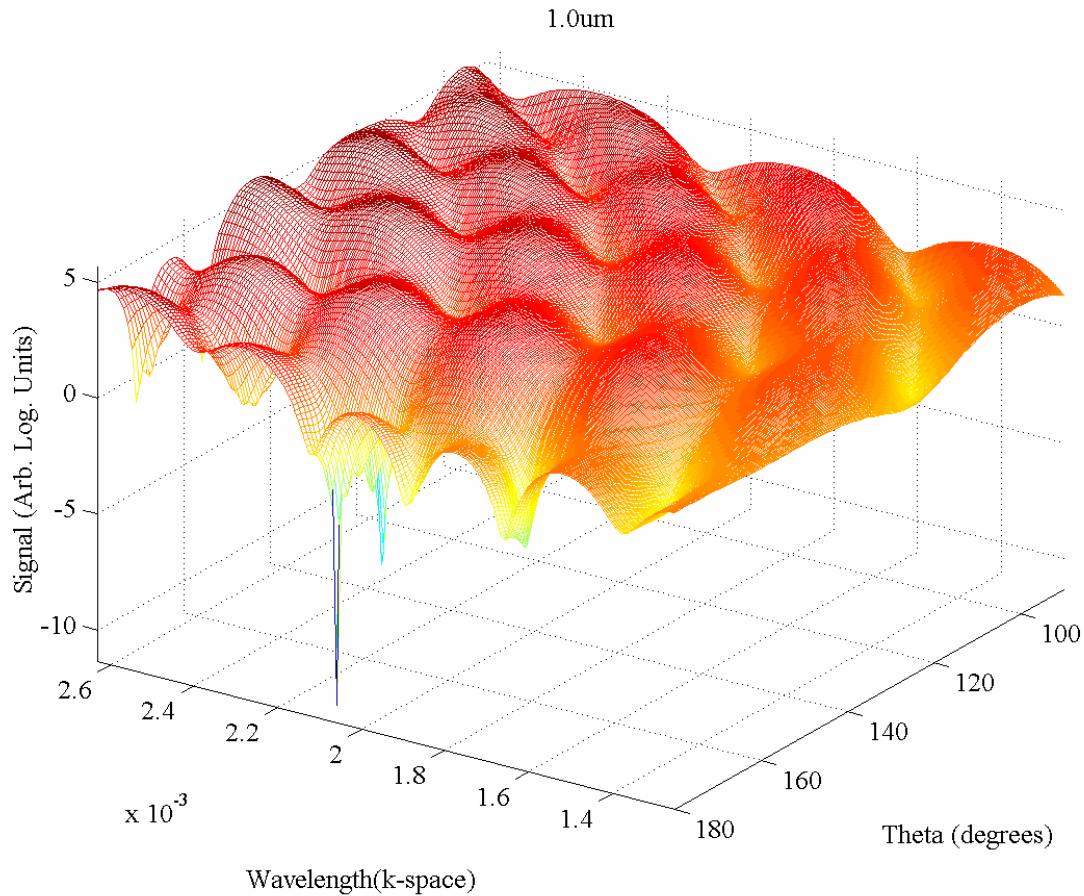


**Figure 57: Wavelength-angle topology for 1.0 $\mu\text{m}$  (90-180 degrees)**

Examining the above semi-log mesh plots, the oscillatory pattern can be easily seen, though there are some interesting minima that can be found around the 2.1 k-space. It can easily be seen that the 180-degree (backscatter at the exact same angle of the incident light) is a very strong signal to many of the other angles. However, separating that signal from the incident light is very difficult. The HSIE operates around 174 degrees, which is not necessarily the ideal angle. By way of analysis, calculating the power in each signal as well as their autocorrelation for each angle yields to following results shown in Figure 58:

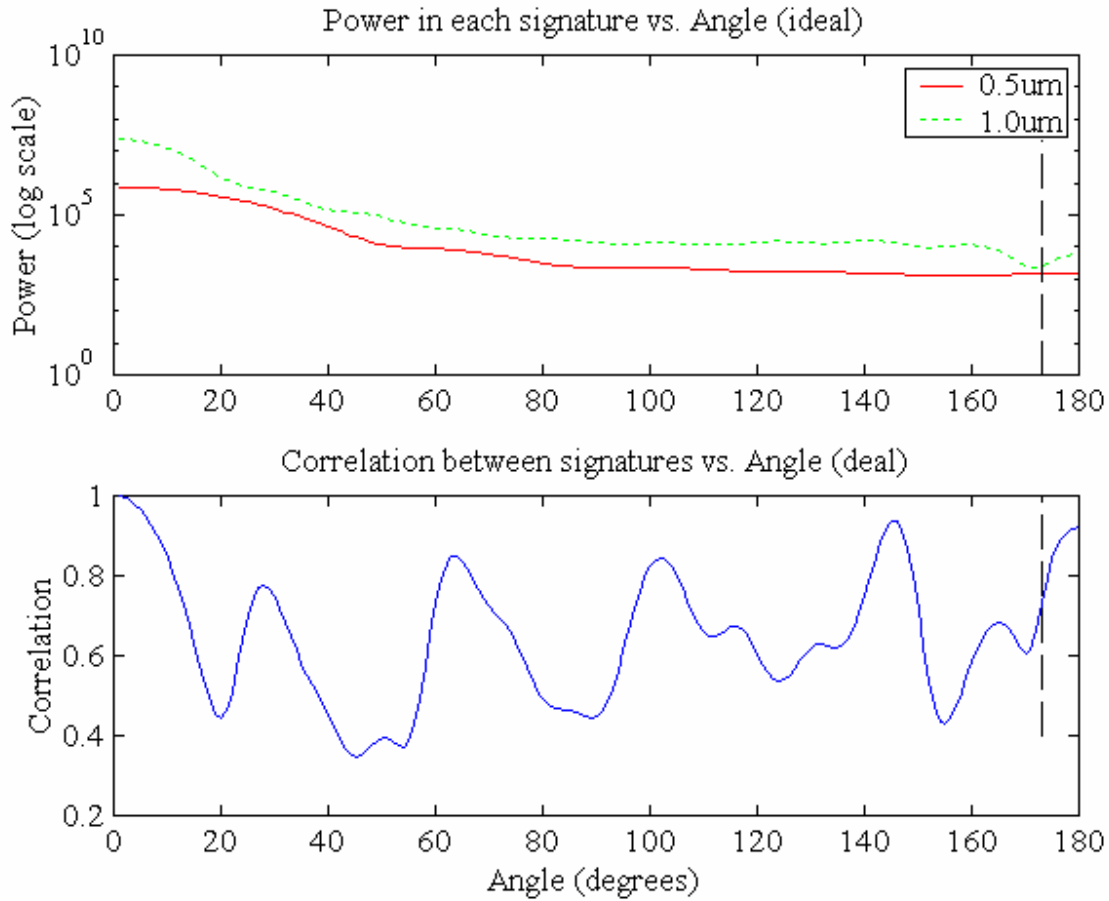


**Figure 58: Power and autocorrelation vs. angle**

The angle that the HSIE currently operates at is denoted by the dashed, vertical line. The upper plot shows how much power is in the reflected signals and the lower plot show the correlation between the signals. It can be observed that the current angle does not fair well in the power region and the signals being detected have a high correlation. As such, it will make distinguishing them more difficult. Figure 59 is a plot of the actual spectral signals found at the 173 degree angle.

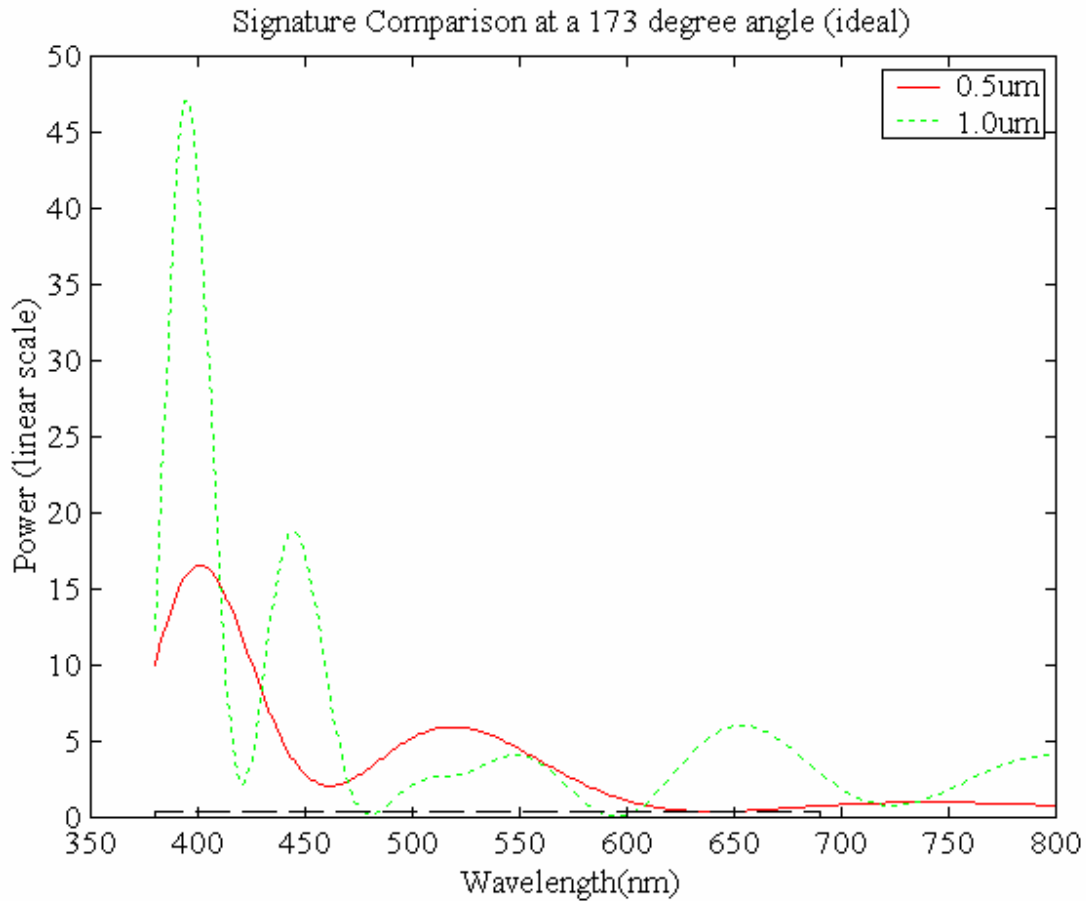


**Figure 59: Signature comparison at 173 degrees**

From a detection point of view, the signals have roughly comparable power while still being different from each other. Finally, it should be noted that the observed topologies differ greatly depending on the bead size.

Comparing the observed data with model predictions is another way to verify the model results. Using the HSIE data collected in the previous sections, the parameters of the observed data were used to predict what kind of signal the HSIE should be detecting in the given case. After performing the same polynomial fit, the resulting signals are directly compared in the following figure.

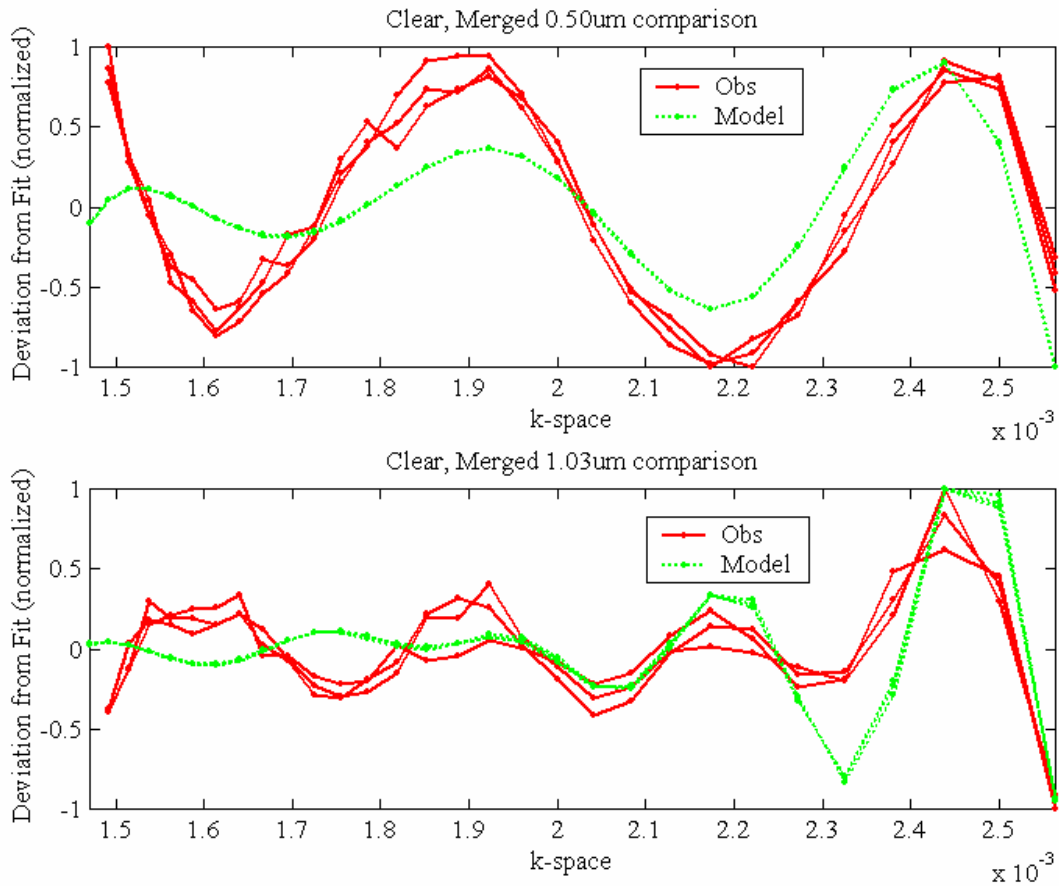


**Figure 60: Model prediction vs. real data comparison**

The above Figure 60 contains six traces for each plot. The three red (solid lines) traces are the observed data, and the three green (dotted lines) are the model predictions over the field of view (the three boxes shown in the various plots from the model sections). There is some variance over the field of view, primarily in the red-light region. However, overall, the signal changes little over the field of view of the model is small, and so it is reasonable to allow subsequent analyses to ignore a given pixel's position in the imaging view, thus treating each pixel as an independent sample.

Looking at the top plot (0.5  $\mu\text{m}$  bead comparison), there is a rough correlation of the oscillatory structure between the model and the observed. Some peaks are shifted slightly but others match. From a frequency-domain perspective, there are two (2) complete cycles.

Looking at the bottom plot, the signal that had the best correlation with the (nominal) “1.0 $\mu\text{m}$  beads” was in fact the predicted curve for 1.03  $\mu\text{m}$ . This discrepancy between the prediction and the observed bead size is within the  $\pm 3\%$  variance in size distribution listed for the beads used in the phantom. From a frequency domain perspective, there are four (4) complete cycles in the observed data, but four and a half (4.5) cycles in the model’s curves.

It is interesting to note that as the signal shifts from the blue to the red part of the spectrum, the correlation shifts as well. The reason for this could be from a prism-like effect of the cuvette wall.

For Figure 60, the media and bead refractive indices are 1.33 (water) and 1.59 (polystyrene bead manufacturer’s value) respectively. It should be noted that other values for the refractive indices ( $\pm 0.05$ ) of the media and beads can be chosen such that the green curves can be made to better overlap the red traces. However, improving the overlap for one bead radius makes the other radius traces overlap much less. This also serves as a reminder of the sensitivity of the scattering signal to the indices of refraction.

#### 4.4 CLINICAL WORK

The first clinical trial was located at the University of Pittsburgh Medical Center (UPMC). Dr. Neil Christie and his staff aided in this by providing the opportunity to work in conjunction with another study to collect *in vivo* data using the HSIE in the operating room (see Figure 61).



**Figure 61: Dr. Christie and his group using the HSIE in the operating room**

Over the span of almost 1 year, data was obtained from 30 patients. The following table summarizes the patients who participated, from whom data was acquired successfully.

**Table 4: Patient racial and gender breakdown**

	<b>Asian</b>	<b>Black</b>	<b>Caucasian</b>	<b>Totals</b>
<b>Male</b>	0	0	15	15
<b>Female</b>	0	1	14	15
<b>Totals</b>	0	1	29	30

Among the issues that encountered while taking data from live patients were:

- *Motion artifacts.* One quarter of a second was faster than any other spectral data collector found in the literature, but it was still not fast enough. Tissue movement from the nearby heart presented band-to-band motion artifacts that had to be accounted for.
- *Triggering issues.* Instead of relying solely on the operator/surgeon to trigger the data collection at the ideal time, using a semi-automatic trigger yielded superior results. This semi-automatic trigger took the form of allowing the system to wait for up to 3 seconds until images with a good signal-to-noise ratio were in view before starting the scan. Empirically, that limited the system to 170/256 and 240/256 of the camera's intensity range and gave reliable results with only a few over-exposed or under-exposed images in extreme cases of movement.
- *Specular reflection.* Given the small angles involved, intense specular reflection from surface in-homogeneities would occasionally burn-through the polarizers and over-expose pixels.
- *Display artifacts.* The Windows operating system used by the data collection and display computer only supports 8-bit grayscale images. Coupled with the contrast limited of LCD screens, this made eyeball estimates on the pixel intensities in a given 12-bit image very

unreliable. Mathematical metrics were quickly derived and implemented in the software; eye estimates were limited to making only the most general qualitative assessments.

- *Tissue trauma.* Passage of the endoscope into the lung traumatizes the tissues, causing inflammation and bleeding in some cases. In this study, patients were placed only under a light sedation, and so in some cases, coughing/lung clearing reflexes were not suppressed sufficiently and would be inadvertently triggered. Such coughing usually traumatized the airways enough so that blood would begin to flow down and coat the visible tissues. This blood coating would make it impossible to optically biopsy the underlying tissues, and so often it was a race against time to image the tissue before it became impossible.

Unfortunately (from a scientific viewpoint), data could not be collected from a patient that turned out to be positive for lung cancer. This raises a few questions about the sensitivity and accuracy of the sputum test used for screening patients, as well as makes estimating the sensitivity and specificity of the HSIE for this application impossible.

With regards to software-related issues, motion artifacts for *in vivo* imaging of tissue proved to be very problematic. Unintentional movement by the target and/or the surgeon holding the endoscope made it very difficult to capture spectral-cubes of with good pixel signal-to-noise ratios (SNR) without over or under exposing the image—particularly in the lungs near moving organs like the heart. This issue is partially related to the Windows operating system’s inability to display intensity gray-maps at depths greater than 8 bits-per-pixel (our camera captures at 12 bits-per-pixel). The conversion algorithms available to us have a tendency to make the operator think that the image is over-exposed, when in fact it is far from it. Furthermore, it is difficult for the operator to trigger acquisition before the ideal frame is in view. Consequently, an automatic pixel intensity range checker was implemented in the software that would cause the spectrum

acquisition to be delayed until the pixel-intensities were within a user-definable range. This automatic feature was very successful in giving us consistent pixel SNR and dramatically reducing the number of spectral-scans required in order to get a “good” one. However, while this did reduce the impact of inadvertent movement of the scope and/or tissue target, it did not eliminate it. It is estimated that a camera speed-up by at least a factor of 3 will be necessary to minimize motion smear sufficiently for it to cease to be a concern.

We have recently undertaken a second study, planning it based on some of the lessons learned in the research described above. This study is still in progress at the Allegheny general Hospital in Pittsburgh PA, using a more recent version of our HSIE instrument. One of the new goals in this study was to aid the surgeon by having the spectral scattering imagery guide (in part) some of the biopsies, with the intent to link the intrasurgical imagery with subsequent pathology analysis. While the technology appeared to work quite well (and reliably), and we were able to investigate 21 consenting patients so far, the frequent changes of participating surgeons, support personnel losses, and other administrative issues made it difficult to achieve all our goals so far. With the promised enhancements in the Pathology department’s participation in the analysis of the biopsied specimens, we hope to obtain more clinically meaningful results soon. Additional, advanced image analysis in collaboration with a group at Carnegie Mellon University Robotics Institute should also improve our ability to extract meaningful conclusions from this study.

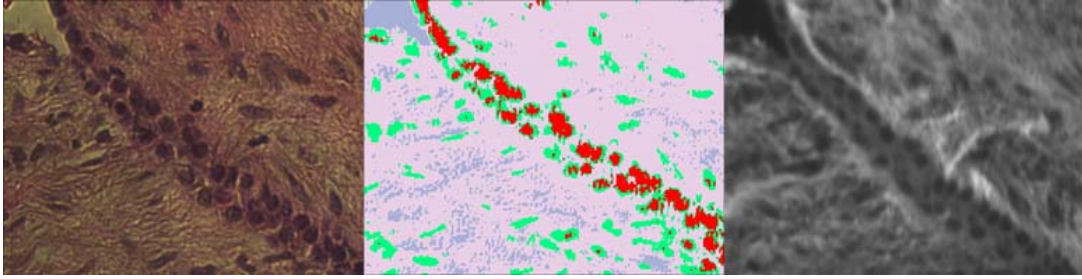


**Figure 62: Same bronchoscopic biopsy-derived tissue sample imaged in three modes (Hematoxylin-eosin stained pathology slide, imaged directly in transmitted light; Hyper-spectral segmentation/classification of the same slide, based on a microscopically acquired image cube and auto-fluorescence image of the same area, excited at 390nm and detected at 430**

## **5.0 SUMMARY AND FUTURE WORK**

The following sections summarize the results, and propose designs for future work.

### **5.1 SUMMARY**

This project had three major thrusts: construction of the hyperspectral imaging instrument, the computer modeling, and testing against phantoms. The construction of the machine was accomplished after the clearing of a couple of engineering hurdles. The first hurdle was the construction of the custom fiber endoscope, which was solved by hiring a sub-contractor to manufacture it. The second hurdle was the synchronized acquisition of the band-sequential images at high speeds. This was solved by building specialized electronics in-house that slave the band-sequential illumination source to a high frame rate camera, and the development of custom data-collection software to run on a laptop. The computer model was done by the translation of verified Mie calculation code from Fortran to Matlab and then performing ray-trace calculations according to the machine geometry to predict what the image should look like. The last thrust, the testing against known phantoms, encountered some difficulties. The phantoms were built and verified by microscopic dissection and laser goniometry, but signal-to-noise issues stemming from the unfavorable illumination angle of the tip and blurring from the wide bandwidth of the illumination source used made extracting the signal from the noise almost

impossible. The HSIE was also used to gather data in the operating room, with the intention of empirically comparing cancerous sites with non-cancerous sites. Unfortunately, of the 30 patients seen, none were positive for cancer, making the empirical comparison impossible. Given the difficulties and additional control parameters unearthed during this project, the current HSIE system proved inadequate to do the task it was developed for. It is not, however, a complete failure. This project has pointed the way towards a device that can perform this task, but the existing design will need to be significantly modified in several ways as described below

## **5.2 NEXT GENERATION SYSTEM**

The next generation HSIE system will need to have improvements made in several areas, some of which are simply upgrading to newer versions of the same technologies. Newer cameras with greater quantum efficiency, higher image acquisition rates, and better response in the 700-800nm (red light) spectrum range are just coming onto the market, and they could be incorporated into any new design. However, there are some trade-offs to be made based on the system parameters that have been identified as part of this work. Based on the trade-offs for these parameters, three new designs can be envisioned.

### 5.2.1 Next Generation System Parameters

The Mie-theory based modeling has made clear several parameters will need to be estimated and/or adjusted to improve the strength of the desired signal:

- Distance estimation ability: The distance from the tip to the target significantly affects the observed back-scattered angle.
- Reduced bandwidth of illumination: The merging (smearing) of the signal by a broad illumination is destroying the signal oscillations, reducing the system's sensitivity.
- Minimization of systemic registration issues: It is (currently) technically infeasible for a fiber with two imaging bundles to be placed so that there is a zero rotational error in the camera's viewfinder

Additionally, the clinical trials with live patients have made clear some additional issues (which are inter-related):

- Increased light collection/camera efficiency: Insufficient light delivery through the illumination fiber forces pixel binning and slower imaging rates.
- Increased acquisition speed: Cardiac movement introduces significant motion artifacts (between spectral bands) into the spectral cube.
- Specular reflection rejection (by increasing the back-scattering angle) or increased camera dynamic range
- Fiber rigidity and/or diameter needs to be reduced if some of the more unusual, but still normal, lung lobe configurations occasionally encountered are to be explored.

In all the designs which follow, this dissertation will explore some of the design changes that could be done to the distal end of the HSIE system. In all the designs, the monochromator is replaced with either an Acousto-Optical Tunable Filter (AOTF) or a liquid-crystal filtered light

source. This change is independent of tip improvements and would immediately narrow the illumination bandwidth from 10-12nm to approximately 2-3nm, allowing for a more finely sampled spectra.

### **5.2.2 New Design #1**

The goal of this design is to maximize the optical angle between the light source and the imaging bundle, but it has the secondary effect of removing the systematic registration problem. Referring to Figure 63, it differs from the current HSIE design in three distinct ways. First, it only has one imaging bundle. Second, the illumination fiber is replaced by a more expensive polarization-compensated fiber that does not have a polarizer in front of it. This allows the illumination to be polarization-sequenced, allowing for both polarizations to be obtained through the single imaging bundle. Third, a method for determining the distance from the tip to the target is added. This is done by adding a smaller, single-mode (monochromatic) illumination fiber located in the center of the triangle. While data is being collected, periodically the single-mode fiber will be illuminated, causing a spot to appear in the image. The size of the spot will be inversely proportional to the distance, and thus give an approximate distance from the tip to the target. Increasing the scattering angle will hopefully increase the signal intensity, as predicted by the Mie simulation model. This fiber design should also be more flexible, as the fiber will be less crowded. A trade-off here is that the acquisition time will be half the rate design #1, since two pictures must be taken to capture both parallel and perpendicular information. In this design the illumination fiber is replaced by a more expensive dispersion compensated fiber that does not have a polarizer in front of it, and only one imaging fiber bundle is used (that does have a polarizer). This change would allow the illumination light source to be rapidly polarized (using a

Pockels cell, for example), thus it then becomes possible to collect both the parallel and perpendicular light using the same imaging fiber.

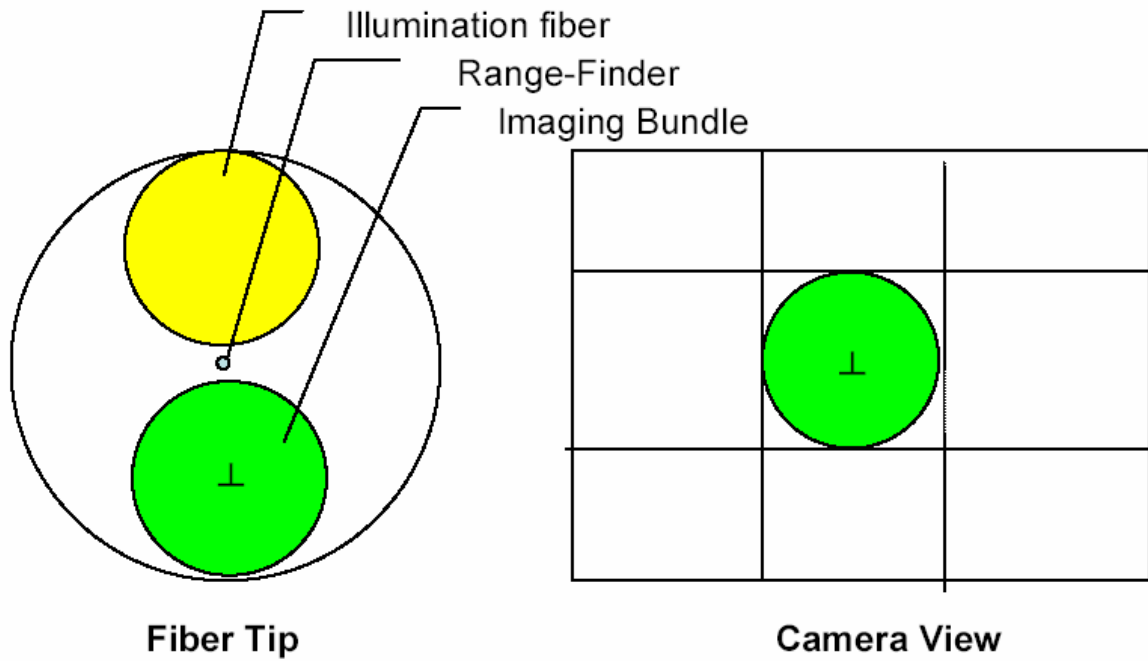
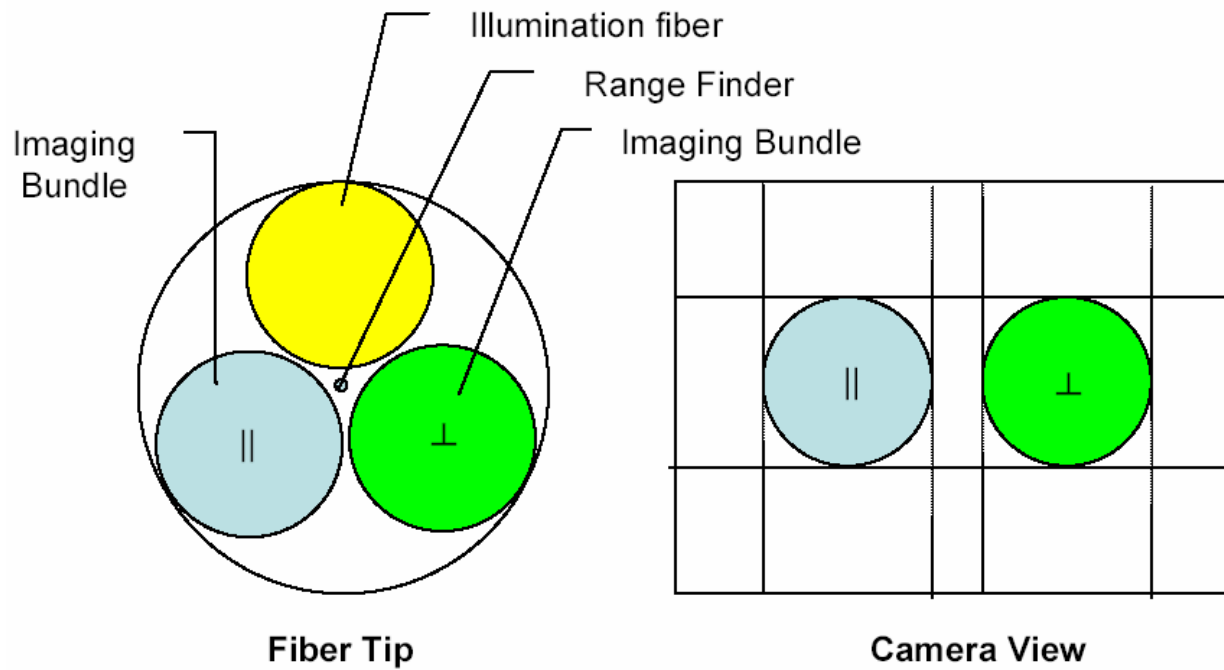


Figure 63: New Fiber design #1

This design will maximize the geometric angle between the illumination and imaging bundles. However, the angle gains are modest given the 2mm constraint and a 10mm working distance. Shortening the working distance would allow the illumination fiber to be polished in a non-flat manner at a 10 degree angle, artificially enhancing the incident light level.

### 5.2.3 New Design #2

The fiber polishing approach does not work in the case of two imaging bundles, and so to increase the angle in this case one must make the total diameter larger. Hence, new design #2 (shown in Figure 64) assumes that the diameter is allowed to be expanded to 3mm. Furthermore, it extends the current design in two distinct ways. First, the illumination fiber is replaced by a more expensive dispersion compensated fiber that does not have a polarizer in front of it (as in the first design). This allows flexibility in how one uses the two fiber imaging fiber bundles. One could use it in the manner of the original HSIE, mimicking the original polarizer configuration and collecting both images simultaneously. One could also sequence the illumination polarization and only collect data from one imaging bundle. In this configuration, the unused bundle could be optically diverted to another use such as an RGB brightfield camera. If the illumination spectrum is similar to the RGB spectrum, the RGB camera could collect light at the same time the other spectral information is collected. Furthermore, the light-sources could be interchanged, allowing a broad-spectrum illumination to instead be used with the RGB when spectral data is not being collected. Secondly, the range-determination scheme described in the first design is also included in this design.



**Figure 64: New Fiber design #2**

This design would solve many of the problems outlined above, but does not address the systemic registration issues unless data is collected using only one of the imaging bundles. However, the fact that data can be collected in several modes makes this design flexible for research purposes.

### 5.2.4 New Design #3

If cost and endoscope diameter were no restrictions, it would be desirable to dispense with the imaging fibers all together and instead switch to a camera-on-the-tip design (see Figure 65). Such a radical design change would accomplish several things.

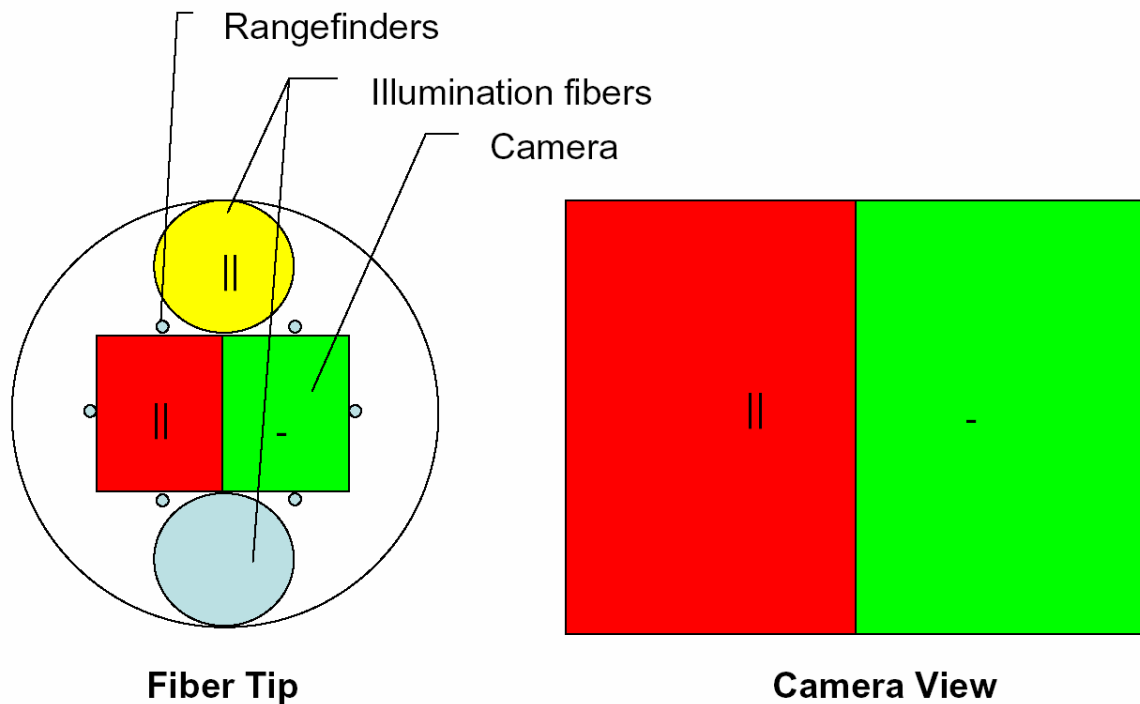


Figure 65: New fiber/endoscope design #3

First, the registration issues between the parallel and perpendicular images would be greatly simplified (only one axis of freedom and no rotation adjustment). Second, increased light from the imaged tissue would reach the camera. Third, the alternate (lower) illumination fiber could be used for either other imaging modalities (such as fluorescence lifetime imaging, whose required excitation laser intensity would burn through any film polarizer) or as an alternate light source

that would allow even more detailed analysis of the distance to the surface being imaged than the six rangefinders would allow. Fourth, this tip would allow the rest of the endoscope to be much more flexible because of the omission of the fiber bundles. Fifth, the inclusion of several optical rangefinders would improve the range estimation for multiple quadrants of the image, providing for a more robust analysis of the surface being imaged.

In conclusion, for the application of Mie theory to become a powerful intra-surgical method using no contrast agents, the following is needed:

- A fundamental understanding of what Mie scattering regime light-tissue interaction is yielding
- Carefully designed and implemented technologies
- Moving from a point spectroscopy to a full-fledged imaging modality, to be on par with established endoscopy techniques and current minimally invasive surgical practice

This work show the first steps in the development of this powerful method. Mathematical modeling and tissue phantoms aid in understanding the fundamentals. Realization of the prototype HSIE and its subsequent use in a real operating room aids in understanding where the state of the technology is today, and what design, logistic and performance issues need to be addressed. It also aids in understanding how new methodologies can be added to the established endoscopy procedures, and how HSIE can help with optical biopsy, and, more generally, with the overall goal of better diagnostics, more tightly coupled - spatially and temporally - into treatments.

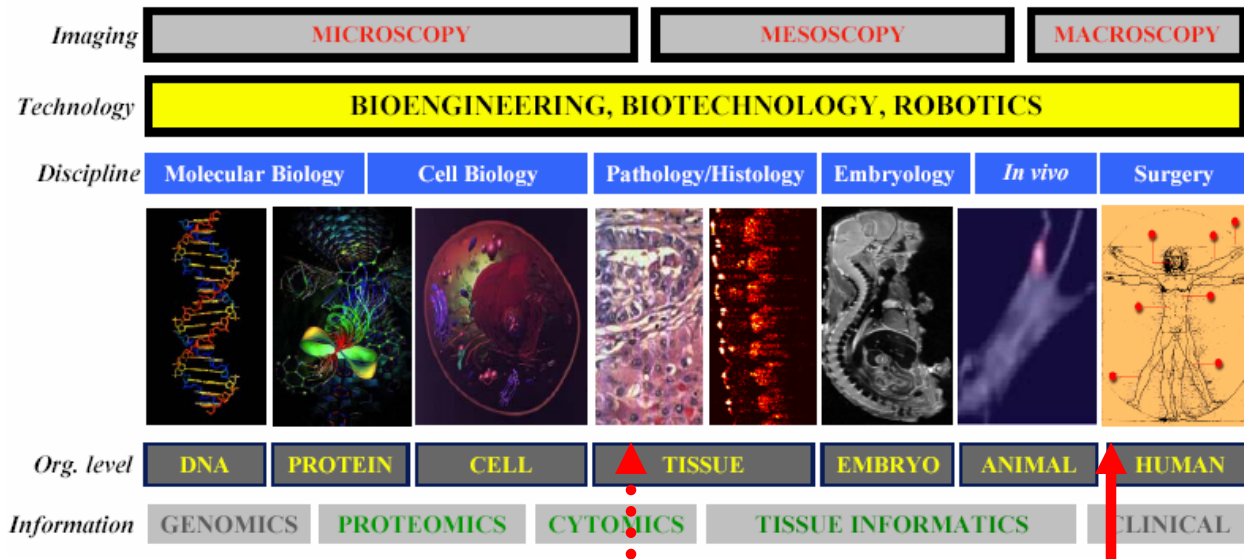


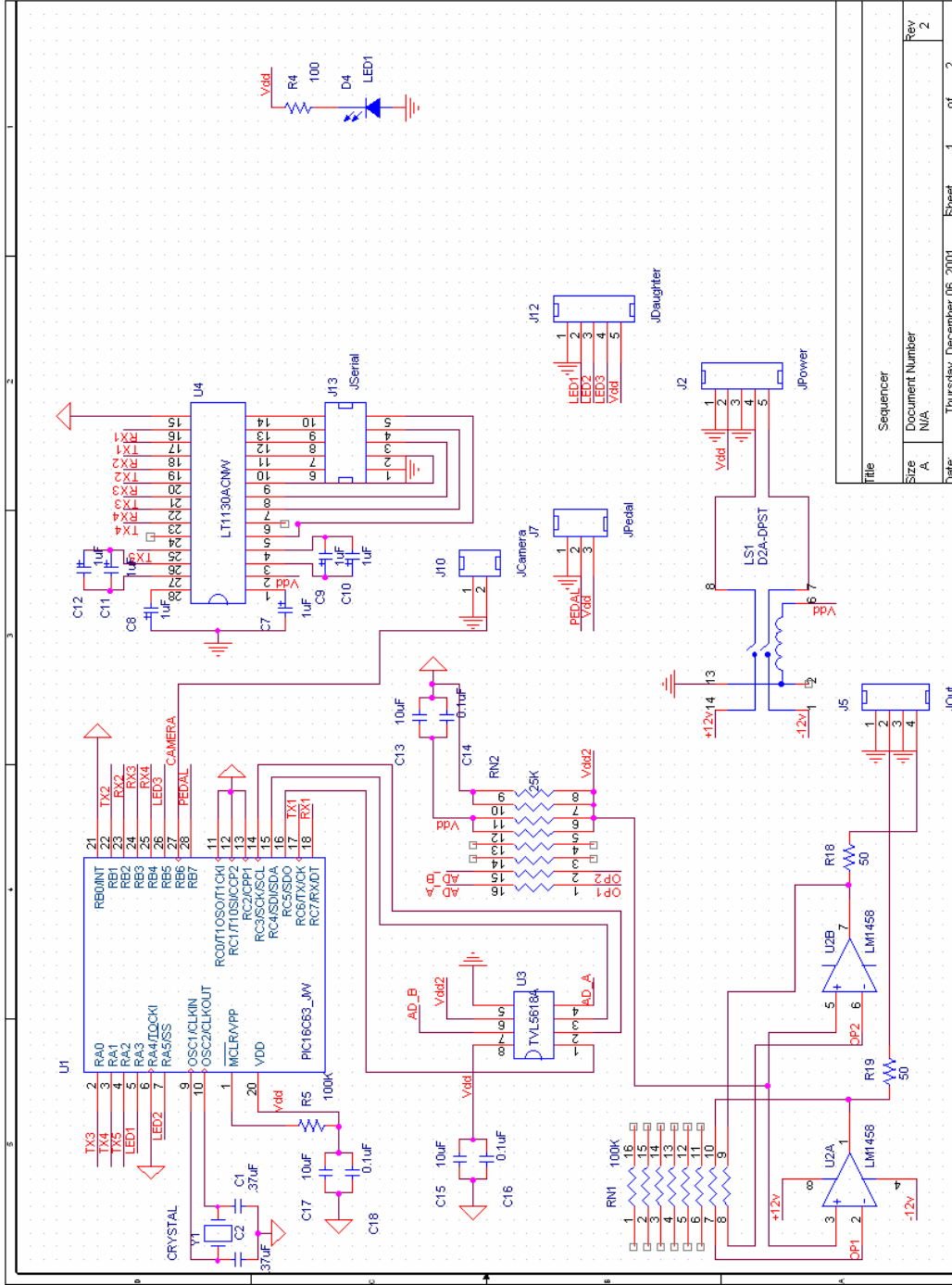
**Figure 66: Bench-to-bedside translational continuum**

In the often mentioned bench-to-bedside translational continuum (within which this project tries to move from the dotted-red arrow to the solid-red arrow), the first implementation of the HSIE glided when pushed out of the laboratory nest. I am confident that the next incarnation will fly, rather than just glide.

## **APPENDIX A**

### **CIRCUIT DIAGRAM AND PROTOCOL OF SEQUENCER**

The diagram which follows is a functional schematic of the sequencer described in the previous sections. The software protocol which controls it then follows.



Title	Sequencer
Size	Document Number
A	N/A
Date:	Thursday, December 06, 2001
Sheet	1 of 2
Rev	2

## Overview of Sequencer Protocol

The Line Protocol is a frame-based canonical byte-encoded protocol. Commands consist of an operator (OP), followed by up to six (6) bytes of data, followed by a checksum (CS) byte, followed by a carriage return (#13):

<b>Operator (OP)</b>	<b>Data Byte 0 – Data Byte 6 (D0 – D6)</b>	<b>Checksum (CS)</b>	<b>End of Frame (#13)</b>
--------------------------	--	--------------------------	-------------------------------

The checksum is a running total of all previous bytes, excluding itself and the end-of-frame byte. The maximum length of the frame (in bytes) is 9. However, for maximum compatibility, all bytes of the frame except the End-Of-Frame (#13) will be encoded in hex. Therefore, the maximum length possible of a hex-encoded frame is 17 characters. For example, a frame of (#10,#11,#00,#21) with the End-of-Frame excluded would be encoded as 0x0A0B0015. Consequently, all communications will be in canonical lines of hex digits. Command Frames can have up to 8 data bytes, while Response frames can have up to 48 data bytes.

### Operator

The operator is broken up into two parts: the most significant 4 bits and the least significant four bits -- In other words, two hex digits. The first hex digit is the Operator Group (OG), and the second digit is the actual command or response message.

The following operators (commands and **responses**) are currently defined (all numbers are in Hexadecimal code):

Group 0: Generic Acknowledgements	<b>00: Bad Frame (Checksum failed)</b> <b>01: Unrecognized Command</b> <b>02: Invalid Data (but valid command)</b> <b>03: Overflow</b>
-----------------------------------	---

	<b>07: Power-on/reset flag set</b> <b>08: Change Acknowledged</b> <b>0C: Unsigned integer response (more to follow)</b> <b>0D: Unsigned integer response (final)</b> <b>0E: String response (more to follow, concatenate)</b> <b>0F: String response (final)</b>
Group 1: Device Information	10: Get Device ID String 11: Get Device Serial Number
Group 2: Status Information	20: Get power on, self test hardware error code 21: Get power on, self test software error code 22: Get configuration error code 23: Get current state 24: Get pass count
Group 3: Device programmable options	30: Clear Power-Reset flag 31: Get Operating Mode 32: Set Operating Mode
Group 5: External Trigger port	50: Get Trigger states 52-58: Get Trigger #0-#6 Mode 59-5F: Set Trigger #0-#6 Mode
Group 4: Voltage Sequencer #0	40: Initialize Sequencer to known zero state 41: Get Mode 42: Set Mode 43: Get Tail 44: Set Tail 45: Get Slot (#) 46: Set Slot (#, value) 47: Get Active Slot 48: Set Active Slot (#) 49: Get Trigger Control Mode 4A: Set Trigger Control Mode 4E: Get Info 4F: Get Secondary Info

### **Error Codes**

Currently defined error codes are:

Hardware	00: No Error
Software	00: No Error
Configuration	00: No Error

### **Operating Modes**

Currently defined operating modes are:

00	Suspended Operation
01	Programming mode
02	Single Pass
03	Repeating Pass

### **Operating States**

Currently defined operating modes are:

0x	Suspended Operation
1x	Programming mode
2x	Start of Pass
3x	Repeating Pass

Where x=software specific sub-phase. Note that the first hex digit corresponds to the operating mode.

## Examples

There are some example protocol exchanges to help in understanding the protocol. Note that after a power up, the box will send only a 0x03 response to any command it receives until the power-on reset flag command (0x30) is received. This allows the controlling computer (master) to detect the event and react appropriately.

### **Power-up example**

Master	Device	Comment
(Anything but command 30)		
	(07)	
30.		<i>Clear power-on flag</i>
	08.	

All numbers are in hex.

### **A basic startup information query example**

Master	Device	Comment
10		Get Device ID String
	0F + String	Reply
11		Get Serial Number
	0D + number	Reply
20		Get Hardware error code

	0D + number	Reply
21		Get Software error code
	0D + number	Reply
22		Get Config error code
	0D + number	Reply
31		Get Current Mode
	0D + number	Reply
23		Get Current State
	0D + number	Reply

All numbers are in hex.

#### Reading the current sequence from the box

Master	Device	Comment
<i>F2</i>		<i>Request the entire list</i>
	<i>0C + number</i>	<i>Slot #1</i>
	<i>0C + number</i>	<i>Slot #2</i>
	<i>0C + number</i>	<i>Slot #(n-1)</i>
	<i>0D + number</i>	<i>Slot #n</i>

All numbers are in hex.

#### Changing the current operating mode of the box

Master	Device	Comment
<i>32.02</i>		<i>Select suspended operation</i>
	<i>08</i>	<i>Okay</i>

All numbers are in hex

#### Programming a fresh sequence into the box

Master	Device	Comment
<i>F4</i>		<i>Clear the list</i>
	<i>0D + number</i>	<i>Number of slots remaining (okay)</i>
<i>F3 + 16-bit number</i>		<i>Add first number</i>
	<i>0D + number</i>	<i>Number of slots remaining (okay)</i>
<i>F3 + 16-bit number</i>		<i>Add second number</i>
	<i>0D + number</i>	<i>Number of slots remaining (okay)</i>
<i>F3 + 16-bit number</i>		<i>(Repeat as necessary)</i>
	<i>0D + number</i>	<i>Number of slots remaining (okay)</i>

All numbers are in hex

If the capacity of the box is exceeded, it will respond with “03 - Overflow”

## Line Coding Examples

<i>Frame (in bytes, hex digits)</i>	<i>Line coding (in characters)</i>	<i>Symantec Meaning (decimal numbers)</i>
30.	3030¶	Clear Power on reset
32.01.	320133¶	Set operating mode to 1
	¶	
0C.2D.	0C2D39¶	45 (more to follow)
0D.2D.	0C2D3A¶	45 (final number)
0E.	¶	“AOTF SEQ” (more to follow)
0F.	¶	“UENCER” (final)

Programming a fresh sequence into the box

<b>Master</b>	<b>Device</b>	<b>Comment</b>
<i>F4</i>		<i>Clear the list</i>
	<i>0D + number</i>	<i>Number of slots remaining (okay)</i>
<i>F3 + 16-bit number</i>		<i>Add first number</i>
	<i>0D + number</i>	<i>Number of slots remaining (okay)</i>
<i>F3 + 16-bit number</i>		<i>Add second number</i>
	<i>0D + number</i>	<i>Number of slots remaining (okay)</i>
<i>F3 + 16-bit number</i>		<i>(Repeat as necessary)</i>
	<i>0D + number</i>	<i>Number of slots remaining (okay)</i>
<i>22</i>		<i>Get Config error code</i>
	<i>0D + number</i>	<i>Reply</i>
<i>31</i>		<i>Get Current Mode</i>
	<i>0D + number</i>	<i>Reply</i>
<i>23</i>		<i>Get Current State</i>
	<i>0D + number</i>	<i>Reply</i>

All numbers are in hex.

## APPENDIX B

### INTERNAL REVIEW BOARD (IRB) DOCUMENT

#### *Imaging Elastic Scattering Spectroscopy Endoscopy IRB Protocol*

#### **Lung Fluorescence Endoscopic Surveillance in Patients at High Risk For Developing Lung Cancer**

**RESEARCH PROTOCOL ABSTRACT:** The purpose of this study is to evaluate the efficacy and usefulness of the LIFE-Lung Bronchoscopy to identify early molecular markers that correlate with pre-cancerous carcinoma in situ (CIS) or micro-invasive lesions and eventually will be used to direct their identification and treatment. Patients with non-small cell lung carcinoma (NSCLC) that have undergone surgical lung resection, patients with head and neck squamous cell carcinoma (HNSCC) that have undergone radical head and/or neck dissection and patients with severe chronic pulmonary disease will be recruited. *Approximately 250 patients will be enrolled in this study through the University of Pittsburgh Cancer Institute.*

#### **HYPOTHESIS AND SPECIFIC AIMS:**

- Establish a surveillance bronchoscopy program for early detection of NSCLC patients, HNSCC patients, and patients with limited pulmonary reserve, who are at a high risk for developing NSCLC.
- Study differences in the mutations in p53 and K-ras genes, bombesin-like receptor-subtypes and HGF protein levels in normal mucosa, metaplasia, dysplasia and CIS.
- Monitor the histologic and molecular impact of PDT on high grade dysplasia and CIS.
- Monitor the impact of Imaging Elastic Scattering Spectroscopy (IESS) on detecting dysplasia and CIS.

**BACKGROUND INFORMATION AND SIGNIFICANCE:** The development of carcinoma of the lung follows a latent period that spans several decades as the normal respiratory epithelium is exposed to various carcinogens. The response of the normal mucosa to these

stresses is believed to be a predictable progression from high grade dysplasia to carcinoma in situ and eventually resulting in invasive carcinoma.(1) There is an average period of four to five years during which time individuals exfoliate markedly atypical cells (that actually represent carcinoma in situ) into the bronchial secretions before the progression to an invasive carcinoma.(2)

If these pre-invasive (high grade dysplasia and carcinoma in situ, CIS) lesions can be detected more efficiently with the LIFE-lung Fluorescence Endoscopic System it will then be possible to interrupt and/or reverse the process of carcinogenesis with a new, FDA approved, non-invasive therapy, i.e. Photodynamic Therapy (PDT).

PDT has been used investigationaly for NSCLC since 1980. A prospective phase II study on PDT with Photophrin II for centrally located early stage NSCLCs by the Japan Lung Cancer Photodynamic Therapy Group demonstrated an 85% CR in 54 patients with 64 carcinomas after initial PDT therapy with a mean duration of complete response of over 14 months. (3) More recently, (1997); Cortese et. al. from the Mayo Clinic documented a complete response in 15/21 patients (16/23 cancers) after an initial PDT session. Subsequent primary lung carcinoma developed in 5/21 patients (24%), however 9 patients (43%) were spared an operation after a mean follow-up of 68 months. (4) On January 9, 1998 Photodynamic Therapy with the photosensitizer Photophrin II, using a 630 nm laser was approved for T1 NSCLCs.(3)

Dysplasia and carcinoma in situ are approximately 90% curable with PDT. At present, less than 15 % of patients with invasive lung cancer can be cured even with aggressive, multimodality treatment strategies (surgery, chemotherapy and/or radiation therapy).(5) By the time an invasive carcinoma of the lung produces symptoms, it is usually locally or systemically advanced beyond curability. In 1998, only one out of eight people diagnosed with invasive, non-small cell lung carcinoma (NSCLC) will live five years.

At present, occult lung carcinomas in these high-risk patients are most commonly identified through periodic sputum cytology and/or standard routine chest x-rays. Both of these modalities are less than optimum screening tools -- the former does not localize the lesion within the tracheobronchial tree and the latter is neither sensitive nor specific for malignancy. Screening with LIFE bronchoscopy yields a 170 - 500% improvement in the detection of high-grade dysplasia and CIS than standard light bronchoscopy however the expense of such aggressive screening can only be justified if the incidence of cancer in the screened population is high. Two populations of high risk patients are the focus of this study: those with severe chronic obstructive pulmonary disorders as demonstrated by obstructive pulmonary functions tests and those who are status-post resection of a NSCLC with no current evidence of disease.

The North American Lung Cancer Study Group showed that Stage I (T1,N0,M0) non small cell lung carcinoma patients who have undergone complete surgical resection have a 60-70% five-year survival but have a 3.6% per year risk of developing a second lung primary.(6) Data from the Mayo Clinic on patients that underwent surgical resection for sputum cytology positive but radiologically occult lung cancer found that second primary lung cancers occurred at a rate as high as 5% per year in this patient population.(7) In a collective review of 1406 patients with occult or stage I completely resected lung carcinomas, the incidence of second-primary lung cancers was 11.4% (range 3-30%).(8) The mortality from second-primary lung carcinomas in surgical patients is much higher than for the first tumor because treatment are both more limited

and complicated as a consequence of their prior lung resection.(9) Second NSCLS primaries are a particularly vexing treatment dilemma in patients who have undergone a prior curative, surgical resection because of their limited, residual pulmonary reserve.

Patients with a history of Head and Neck Squamous Cell Carcinoma (HNSCC) are at a high risk of developing carcinomas throughout their respiratory tract, with many of these arising in the lungs. (23) Many of these tumors are found to be low-stage lesions and are amenable to treatment if detected early enough. (23) In a retrospective study, Leon *et al.* (24) reported 302 (16%) out of 1,845 patients with HNSCC had developed a second carcinoma, with 31% occurring in the lungs. In support of this finding, a study done by Cahan *et al.* (25) demonstrated that a second primary lung carcinoma was present in 137/142 lung tumors in patients with HNSCC. Occurring at a rate of 3-7% per year, second carcinomas may lead to significant complications and an overall poor survival rate in this particular group of patients. (23,24) Close medical surveillance would allow for an earlier diagnosis of a second tumor and a greater chance of benefiting from preventative therapy. (23,25) Cooper *et al.* (26) believe that preventative therapy will have its greatest impact in those patients who continue to have routine follow up visits and who are treated for an early stage primary tumor.

Patients with severe COPD are also at high risk for developing NSCLC and are difficult to manage with curative-intent because their diminished pulmonary function prohibits pulmonary resection or definitive irradiation. The recent revival of lung volume reduction surgery (LVRS) to improve the mechanics and subjective sense of dyspnea of patients with severe, disabling COPD has reinforced the concomitant risk of lung cancer in these patients. A clear correlation, independent of cigarette smoking, exists between obstructive lung disease and lung cancer.(10) Hazelrigg *et al.*(11) reported finding 18 lung carcinomas in 281 patients who underwent LVRS for an overall incidence of 6.4%. These data are consistent with the 7.8% incidence of carcinomas in this same LVRS population previously reported by Pigula *et al.* from our institution in 1996.(12) In Hazelrigg's series, 9/19 (47.3%) of the lesions were radiographically occult - 4 were identified intra-operatively and 5 lesions found incidently in the resected specimen by the pathologist.(13)

White light bronchoscopy has been shown to be a useful tool in localizing radiographically occult lesions. However, Woolner *et al.* demonstrated that only 29% of carcinoma in situ (CIS)(12) and 69%(15) of micro-invasive tumors are identified by experienced bronchoscopists. In 1996 an endoscopic lung imaging system developed by the British Columbia Cancer Research Centre in conjunction with Xillix Technologies Corp., known as the LIFE-lung Fluorescence Endoscopy System was approved by the FDA. LIFE-lung bronchoscopy is performed with a helium-cadmium laser using blue light @ 442 nm for illumination and allows visualization of these differences in normal and abnormal tissue autofluorescence. Lam and others have shown that the tissue autofluorescence spectra of areas of dysplasia and carcinoma in situ differ significantly from those of normal bronchial tissues. (16) Specifically, LIFE Bronchoscopy improved sensitivity of detection of metaplasia and dysplasia is improved by 171% over current WLB. LIFE bronchoscopy's sensitivity for the detection of CIS is 500% greater than that of standard WLB.

In vivo spectroscopy with an optical, multichannel, analyzer enables the LIFE bronchoscopy system to demonstrate a difference in autofluorescence intensity (predominantly in the green region of the visible spectrum) of areas of dysplasia or carcinoma in situ in comparison to normal bronchial tissue. These autofluorescence differences in the absence of exogenous drugs were exploited to design and develop the LIFE-lung system.(17) In a normal bronchus, most of the

auto-fluorescence comes from the submucosa.(18) (Most likely, the decrease in fluorescence intensity in dysplasia and CIS is due to both thickening of the epithelium, loss of endogenous fluorophors and increased light absorption by the increased capillary density in these lesions.)

The LIFE-lung Fluorescence Endoscopy System is comprised of a 125 mW helium-cadmium laser as a source of blue light (442 nm), two image-intensified CCD cameras with green (520nm) and red (>630 nm) filters, a computer with an imaging board and a color video monitor.(19) The blue light is delivered to the bronchial surface with an adapter that connects to the fiberoptic light-guide of a standard, white-light, bronchoscope. Non-collimated light at 12-15 mW is emitted at the distal end of the bronchoscope. The fluorescence from the bronchial surface is captured by the imaging bundle of the LIFE-lung Endoscopy System. Images of the bronchial mucosa at both red and green wavelengths are simultaneously captured by the image intensified CCD cameras onto the imaging board of the computer. These images are then integrated using a specially developed algorithm such that normal tissue can be differentiated from dysplasia and CIS and are displayed in real time.

Fluorescence bronchoscopy using the LIFE system is identical to standard flexible bronchoscopy except that it utilizes blue light (from a Helium-Cadmium light source) in contrast to white light (commonly emitted from a Xenon or Halogen light source). Both fluorescent and reflected light are produced when the bronchial surface is illuminated by visible light, the difference is that with the LIFE-lung system, the image is reconstructed from emitted fluorescent light instead of from light reflected off of the bronchial surface. Emitted fluorescence and reflective light are separated by appropriate filters.

To compare, the standard Pentax Videobronchoscope System (VB-2000, Asahi Optical Col Ltd., Tokyo, Japan) uses a 300 W Xenon short-arc lamp (Model EPM-3000) with a filter wheel to produce red, green and blue light sequentially at a video rate. The red, green and blue reflectance images are then captured sequentially by a single CCD detector at the tip of the bronchoscope and combined to construct a reflectance color image. Using the Pentax light source the light-intensity at the tip of the bronchoscope is 200 mW in contrast to the 15-20 mW output from the Helium-Cadmium laser light source. There has not been a single report of any adverse effects from exposure of the human bronchus to visible light since the introduction of fiberoptic bronchoscopy in 1967.

**In addition to using the LIFE-Lung Fluorescence Endoscopic System, we will also be investigating the use of imaging spectroscopy. In collaboration with Carnegie-Mellon University, Daniel L. Farkas, PhD and Elliot Wachman, PhD have proposed an alternative optical procedure in the early detection of cancer known as Imaging Elastic Scattering Spectroscopy (IESS). This technique is sensitive to small changes in tissue morphology, and thus provides a way of detecting abnormal lesions *in vivo* in much the same way that a pathologist routinely does *ex vivo*. This system performs imaging spectroscopy, in which measurements are made over 10,000 points at once. The intent of this procedure is to collect spectroscopic image data from abnormal tissue detected on the LIFE system. The IESS scope will be inserted through the instrument channel of the LIFE endoscope prior to any biopsies being taken and the image will be acquired within 0.5 seconds. The IESS scope is then removed and the biopsy performed as usual. The IESS data will be analyzed, correlated with the pathology reports and stored at Carnegie-Mellon University under the supervision of Dr. Elliot Wachman, PhD. At the conclusion of the trial, the complete set of spectroscopic images will be categorized by lesion type and evaluated for sensitivity and selectivity.**

This IESS scope is manufactured, as specified by Drs. Farkas and Wachman, by Instrument Technologies, Inc., a nationally recognized producer of custom OEM medical products in full compliance with the FDA's GMP and ISO 9001 regulations. The light source to which this scope is connected (TILL Photonics, Model Polychrome IV) is based on a 150W Xenon lamp, similar to that used in conventional endoscope light sources. A standard digital camera mounted to the endoscope and PC complete the IESS system.

**SIGNIFICANCE:** The risk of developing second lung primary in a patient with NSCLC who has undergone a potentially curative resection is almost 5% per year with limited salvage treatment options available (20). Identification of pre-malignant changes such as high-grade dysplasia and carcinoma in situ has been elusive until the development of the LIFE-Lung Fluorescence Endoscopic System which received FDA approval for the detection of dysplasia and CIS in 1996. Unpublished data from a recent multi-institutional clinical study showed that LIFE bronchoscopy, when used as an adjunct to conventional WLB, improved the physician's ability to identify moderate/severe dysplasia or worse, when compared to WLB alone on a per-patient basis from 37% to 75% and on a per-lesion basis, detection improved from 25% to 67%; and an overall 171% increase in the detection rate (21).

Historically, areas of high-grade dysplasia and carcinoma in situ could only be "followed" however, significant data now exist that suggest that these early lesions are 90% curable employing a noninvasive, local treatment i.e. PDT (22). The LIFE-Lung system can be used to correlate the histopathologic changes in the tracheobronchial epithelium with molecular abnormalities at a given point in time (static), to study their progression longitudinally over time (dynamic) and to monitor their response to therapeutic intervention with photodynamic therapy. Identification of early activation events in the mucosa could translate into means to perform molecular screening of sputum as an adjunct to cytologic screening.

**PROGRESS REPORT AND PRELIMINARY STUDIES:** (See Background section).

**RESEARCH DESIGN AND METHODS:** Two hundred and fifty adult (age>18) male or female patients from three different high risk patient populations will be studied. The first population consists of patients with Non-Small-Cell Lung Carcinoma (NSCLC) who are status post complete resection and have no evidence of disease (NED). The second group is composed of patients with Head and Neck Squamous Cell Carcinoma who are status post radical head and/or neck dissection and are NED. The third population of patients are those with severe chronic, obstructive, pulmonary disease (COPD). These three cohorts of patients were selected because of the high incidence of CIS development in each group, not for comparative purposes between the populations. No patients will be excluded on the basis of race, gender, or HIV status.

Bronchoscopic Procedures:

The bronchoscopies will be done in the Department of Thoracic Surgery at UPMC. All investigators will be checked for color blindness using standard color charts. Study patients will be NPO for a minimum of six hours prior to the procedure and one hour afterwards. Standard preoperative parenteral medications are permissible. Lidocaine Lollipop, Lidocaine Injection

(LTA), Preoperative and intraoperative Versed and Fentanyl, intraoperative 1% Topical Xylocaine (vocal cord and tracheobronchial paralysis). Viscous Lidocaine (hypopharynx), Cetacaine spray (nasopharynx) and Intra-tracheal instillation of 1% Lidocaine (vocal cords) will be used to achieve adequate airway anesthesia. Conventional WLB will be carried out first using an Olympus BF20D fiberoptic bronchoscope. The entire tracheobronchial tree will be inspected and videotaped. The exact location of any Class II and Class III changes will be recorded in the image management program in the LIFE system during the bronchoscopy. Tissue will be classified according to the following:

Class I: no visual abnormalities, appears normal.

Class II: inflammation, trauma, anatomical anomalies, possible metaplasia.

Class III: changes suggestive of moderate or severe dysplasia, carcinoma in situ, invasive cancer.

During the WLB exam the physician will be allowed to change classifications for a given site. However once fluorescence bronchoscopy has begun the physician will not be allowed to make revisions to the classifications made during the white-light exam.

Fluorescence bronchoscopy will be performed using the LIFE-Lung Endoscopic System following completion of the WLB examination, by merely changing light sources. Again, the entire exam is to be videotaped and narrated. The precise location of all Class II and Class III changes will be recorded in the image management program of the LIFE system.

Tissue samples will be classified according to the following categories:

All Class II and Class III lesions will be biopsied with forceps, at least one biopsy per area. In addition, one random biopsy will be obtained from a visually (by WL and LIFE bronchoscopy) Class I area. A total of four random biopsies will be taken if no Class II or Class III areas identified by WLB or LIFE bronchoscopy.

All biopsies will be snap-frozen (for molecular markers), formalin-fixed and paraffin embedded for hematoxylin and eosin staining.

Interpretation of the histopathology will be made by one designated pathologist, Samuel Yousem, MD, without knowledge of the LIFE-bronchoscopic findings.

No radiation or photosensitizing agents will be administered to patients for either the WLB or LIFE-bronchoscopy exams.

#### Molecular Markers:

In addition to the tissue samples a blood sample (one 10 ml green top tube) will be taken. Patients will also be asked to fill out a questionnaire about smoking history, family history, and other risk factors, as well as place of residence and other demographic information. The patients will not receive results of the research for molecular markers and they will not be placed in the patients medical record.

1-2 mm<sup>3</sup> biopsies will be taken. A matching normal biopsy will be taken for each biopsy of a lesion. These will be designated by a alphanumeric code to designate anatomical location and

patient ID. One biopsy from each area will also be taken for histology (formalin fixation). The other biopsies will be snap frozen in liquid nitrogen in the OR, within 30 seconds of collection and transported on dry ice or in liquid nitrogen to Dr. Siegfried's laboratory, where they will be stored at  $-80^{\circ}\text{C}$  until distributed to investigators. A portion of the biopsy will be fresh frozen and analyzed for DNA mutations in p53 and K-ras genes.

The following preparations from the biopsies will be made. Each abnormal biopsy and matching normal biopsy will be used for either DNA, RNA, or protein isolation. An attempt will be made to distribute the biopsies equally among the three procedures. From the isolated DNA, mutations in the p53 gene and the K-ras gene will be assayed. Researchers have shown that p53 and K-ras deletions occur in lung tumors. Preliminary data suggest that bombesin-like peptide receptors are over-expressed in smokers, therefore these receptors will be assayed by reverse transcriptase-polymerase chain reaction (RT-PCR). From the isolated protein, telomerase activity will be determined using the TRAP assay, and levels of HGF protein, believed to be associated with the invasive process in lung cancer, will be assayed by Western Blot. The goal of these studies is to identify molecular markers that could distinguish between normal mucosa, metaplasia, dysplasia and carcinoma in situ. The effect of PDT on any/all markers identified will also be studied.

The blood will be treated as follows: white blood cells will be separated by Ficoll-Hypaque and frozen at  $-80^{\circ}\text{C}$  for later DNA isolation. The plasma will be stored frozen in 2 ml aliquots in a non-frost free freezer. The white blood cells will be used for isolation of DNA to determine cytochrome P450 (CYP) genotypes and Phase 11 enzyme genotypes. Although there are no immediate plans to assay any markers in the plasma, it will be retained for future use. Sputum specimens will be analyzed for the following molecular markers: Kras and p53 mutations as well as hepatocyte growth factor.

The bloodwork, sputum and biopsy specimens will be under the control of the principal investigator of this research project and will not be shared with secondary investigators (i.e., other than those involved in the current research project). The results of these tests cannot yet be interpreted or applied in a clinically relevant or meaningful manner and will not be provided to the subjects. If this information should become clinically relevant as a result of the availability of new strategies for the prevention or treatment of lung cancer it will be provided to the patients.

We anticipate that up to 350 patients per year will be asked to participate. We expect approximately a 50% accrual rate, however, only about 50 to 100 will actually have lesions that require biopsy, who will contribute tissue to the study. About 75% are estimated to come from the previous lung cancer group and 25% from the COPD population. Individuals who have high grade dysplasia, carcinoma in situ, or microinvasive carcinoma will be offered photodynamic therapy. We will obtain serial biopsies from these patients for clinical surveillance annually in patients with normal mucosa and at six months for patients with metaplasia or dysplasia.

#### Photodynamic Therapy for High Grade Dysplasia and Carcinoma In Situ Lesions:

Photodynamic therapy for early (T1) NSCLC lesions was approved by the FDA on January 9, 1998. PDT for high grade dysplasia, carcinoma in situ, or invasive carcinomas (T1 lesions) will be administered in the standard well-published fashion. Specifically, a total dose of 100-200  $\text{J}/\text{cm}^2$  will be delivered using a KYP/YAG-dye tuned to emit a 630 nm wavelength light 48 hours after a Photofrin II injection (2mg/Kg), to those lesions over approximately 500 seconds. A 1cm

or 2.5 cm cylindrical diffuser fiber - the length dependent upon the axial length of the lesion will be used. A clean-up bronchoscopy (white light) is performed to remove mucous and cellular debris (bronchial-casts) 24 hours after the PDT treatment. A follow-up LIFE-bronchoscopy will be performed 6 weeks after PDT treatment and all treated lesions will be re-biopsied. If a patient would be eligible to receive photodynamic therapy the procedure, risks and benefits will be discussed by the attending surgeon and the patient will sign a hospital consent form for that procedure.

#### Patient Follow-up:

Patient surveillance will consist of a repeat LIFE bronchoscopy. Patients who are found to have no abnormalities will have a follow-up bronchoscopy one year after the initial bronchoscopy. Those diagnosed with moderate to severe dysplasia will be assessed and re-biopsied in three months. Those with CIS will be re-evaluated 6 weeks after Photodynamic Therapy treatment, with a repeat LIFE bronchoscopy and biopsy of the anatomic location of the treated lesion.

#### **BOISTATISTICAL DESIGN AND ANALYSIS:**

The number of biopsies taken in each patient will vary depending upon the identification and number of Class III areas visualized. Previous experience with the LIFE-Lung endoscopy system, in conjunction with white light bronchoscopy (WLB) has found that the prevalence of moderate or severe dysplasia, or carcinoma in situ was 19% in patients that had a primary lung cancer completely resected. We will assume our post-resection patients are similar and that the combined modality (WLB and LIFE) detection rate is 50% higher than WLB alone. An increase in detection rate of moderate or severe dysplasia or carcinoma in situ using LIFE of less 20% would not represent a clinically meaningful improvement so that the study is designed to allow this possibility to be excluded with high probability. From Table 1: the probability that the null hypothesis that "LIFE increases the detection rate by only 20%" would be rejected if the true effect was that "LIFE increases the detection rate by 50%" (alternative hypothesis). This assumes that only one positive biopsy is obtained from each subject, multiple positive biopsies will increase the power of the study. These statistics are based on a sample size of 250 patients which will provide good power at the  $\alpha = 0.05$  level. Over the past two years, 7/1/95 - 6/30/97, there have been 594 lung resections performed at the University of Pittsburgh Medical Center by surgeons in the Section of Thoracic Surgery, and accrual of this number of post-resectional patients should not be difficult. Previous clinical studies with the LIFE-Lung system have suggested that its false positive rate is similar to that of WLB, with neither technique having a particularly high rate, so that the power to test differences in their specificities will be low with the chosen sample size of 250 patients.

One objective of this study is to measure the differences in the detection rate for moderate and severe dysplasia as well as CIS between LIFE-Lung fluorescence and WLB (reflective) bronchoscopy. This will be calculated on a per-person and a per-lesion basis. Confidence intervals will be calculated assuming these observations to be independent. Ratios between these quantities and values calculated for WL bronchoscopy alone will be computed. The distribution of LIFE +/WLB - & LIFE -/WLB + lesions conditional to the total number of +ve lesions will be analyzed using a  $\chi^2$  test on both a per-person and per-lesion basis. An important objective will be to determine the false positive rate of WLB and LIFE-Lung bronchoscopy especially after PDT treatment of CIS lesions with Photophrin.

**HUMAN SUBJECTS:** No exclusion criteria shall be based on race, ethnicity, gender or HIV status.

Lung

National	Native Amer/Eskimo	Asian	Black	Hispanic	White	Other	Overall
Female	0.10	0.30	6.50	0.40	32.30	1.70	41.30
Male	0.10	0.70	11.00	0.80	0.80	2.70	58.70
Total	0.20	1.00	17.50	1.20	1.20	4.40	100.00

University Health System Consortium (UHC) Database Calendar Year 1995

Lung

Local	Native Amer/Eskimo	Asian	Black	Hispanic	White	Other	Overall
Female	0.00	0.00	3.10	0.00	38.40	0.50	42.00
Male	0.00	0.50	8.10	0.00	49.10	0.30	58.00
Total	0.00	0.50	11.20	0.00	87.50	0.80	100.00

University Health System Consortium (UHC) Database Calendar Year 1995

ELIGIBILITY/INELIGIBILITY CRITERIA:

Inclusion Criteria:

1. Patients with NSCLC that have undergone complete resection, via a lobectomy, pneumonectomy or wedge-resection, and who are currently NED.
2. Patients with HNSCC that have undergone radical head and/or neck resection and who are currently NED.
3. Patients with severe chronic, obstructive, pulmonary disease as evidenced by pulmonary function studies abnormalities: i.e. FEV<sub>1</sub> < 50% predicted; RV > 200% predicted and/or DLCO < 40% predicted.

Exclusion Criteria:

1. Patients with uncontrolled hypertension (systolic > 200 mm Hg, Diastolic pressure > 120 mm Hg).
2. Patients with unstable angina.
3. Patients with known or suspected pneumonia.
4. Patients with acute bronchitis within one month of the procedure.
5. Patients who have received neoadjuvant or adjuvant chemo- or radio-therapy within the past six months.
6. Patients with white blood count less than 2000 or greater than 20,000 and/or platelet count less than 50,000.
7. Patients with any known bleeding dyscrasia.
8. Patients who have received fluorescent photosensitizing drugs such as Photofrin within one month of the procedure.
9. Patients with known allergic reactions to topical xylocaine.
10. Patients who are on or have received chemopreventive drugs (i.e. retinoic acid) within one month of the procedure.
11. Patients who have received ionizing radiation to the chest within six months of the procedure.
12. Patients who have received systemic cytotoxic chemotherapeutic agents within the past six months.
13. Patients who are pregnant or nursing. All women of childbearing potential must have a negative serum pregnancy test prior to enrollment.

Sources of Research Material Patients who are seen in UPCI/UPMC clinics are identified as potential research subjects. Other subjects are referred in specifically for possible participation in a particular study which they or their physician are aware of based on publications, which list clinical trials at UPCI by means of various publications, including the World Wide Web. Such publications and Web listings are not advertisements for specific studies. Rather, they are public listings of trials available.

Recruitment Methods and Consent Procedures. Once a patient is identified as a potential participant in a research study as indicated in above, they are screened for eligibility. Depending on whether the screening procedures are invasive or whether they involve tests that would not be done in the routine care of the patient, an appropriate consenting procedure would be carried out as follows:

If the screening procedures are invasive and/or involve tests that would not be done for the routine clinical care of the patient, they would be asked to provide written informed consent before they are screened.

If the testing to determine eligibility is such that would be done for routine clinical care, the potential subject would not be asked to sign a consent form until such time as they are determined to be legible for the study.

In either case, the consent process would be carried out as a joint effort among the patient's physician, the study coordinator, and/or the investigators on the study.

Potential Risks. Patients who will be recruited into this study are those where a standard fiber-optic bronchoscopy would be indicated either to establish the exact anatomic tumor location and rule out synchronous lesions (in patients with T1-T3,N0,M0 lesions) preoperatively or patients who have undergone a previous anatomic resection of their NSCLC primary and are not currently undergoing adjuvant therapy (within the past six months). The specific risks associated with a standard bronchoscopic procedure include:

Bleeding (usually mild and self-limiting): < 1:20,000.

Drug reaction, including over-sedation: < 1.0%.

Pneumonia, bronchitis or aspiration requiring therapy: <1.0%

Loss of teeth: < 1.0%

As an adjunctive examination during a standard fiber-optic bronchoscopy, fluorescence examination with the LIFE-Lung system will carry similar potential risks. Although the risk of an adverse drug reaction will already incurred with the standard fiber-optic bronchoscopy, the risk of bleeding secondary to additional biopsies will be additive.

All patients will undergo WLB and LIFE-Lung bronchoscopy with continuous electrocardiographic and oximetric monitors. If a patient develops a significant arrhythmia or sustained de-saturation below 90% on supplemental oxygen the procedure will be terminated. The bronchoscopy suite will be fully equipped with emergency medical equipment and supplies. Additional time to perform the LIFE-lung fluorescence examination is approximately thirty minutes. There is no foreseeable risk to either patient population in extending the examination time approximately 30 minutes.

Risks associated with photodynamic therapy primarily include: allergic reaction (7.7%) and photosensitivity (1.9%) after photophrin II injection, transient elevation of ALT (1.9%), and pulmonary toxicity (predominantly atelectasis) (7.7%).

Risk Management Procedures. Patients will be monitored at intervals as stipulated in the Methods section. Appropriate care will be provided to patients who experience difficulty while being treated, and patients are encouraged in the consent forms to report adverse experiences to the investigators. This information is collected per the protocol, and treatment is administered as needed.

Evaluation of the Risk/Benefit Ratio. Evaluation is performed as per the statistical information in the protocol. Any interim reports which are prepared by the investigators or received from the sponsor would be provided to the University of Pittsburgh IRB.

**JUSTIFICATION FOR UTILIZATION OF GCRC RESOURCES:** The principle investigator and protocol coordinator will meet on a three month interval to review data and adverse events and summarize with a progress report that will be given to the University of Pittsburgh IRB. Any reports received by the sponsor will also be given to the IRB.

**RESEARCH NEEDS TO BE PROVIDED BY INVESTIGATOR'S OR OUTSIDE LABORATORY:** (see elsewhere in text)

**FUNDING SUPPORT:** American Cancer Society – Pittsburgh Cancer Institute Grant, University of Pittsburgh Department of Surgery, National Cancer Institute/National Institutes of Health.

**COSTS AND PAYMENTS:**

LIFE-lung bronchoscopy will be performed in tandem with standard white light bronchoscopy, the latter is a routine examination covered by insurance for patients with indications such as lung cancer, COPD, chronic cough, hemoptysis and other pulmonary symptoms. No payment for participation will be given. The patients will be billed for a conventional bronchoscopy, the standard pathologic examination of biopsies and standard sputum cytology. The patient will not be billed for the LIFE-lung bronchoscopy, the biopsies, or the molecular marker laboratory work relating to the biopsies, sputum or blood sample. PDT for T1 NSCLC is an FDA-approved treatment and covered by patient insurance as well.

Molecular studies of biopsies obtained through LIFE Bronchoscopy are being sponsored by several research grants. A group of investigators (the Lung Carcinoma Working Group) at UPCI is interested in studying these biopsies to obtain preliminary data for a Program Project Grant to examine early events in lung carcinogenesis. These investigators include: Drs Jill Siegfried, Phoutone Keohavong, Marjorie Romkes, William Bigbee, and Sharon Shriver. The UPCI Lung Cancer Basic Science Program is sponsoring a Pilot Project to Dr Phoutone Keohavong (total costs \$20,650) to examine mutations in p53 and K-ras genes in these specimens. Dr Jill Siegfried has a grant from the NIH to study bombesin-like peptide receptors (direct costs \$163,000 per year) and these funds will be used to examine these receptors in LIFE Bronchoscopy specimens. Dr. Siegfried also has a grant from the American Cancer Society to study hepatocyte growth factor (HGF) which will cover the costs of measuring HGF in these specimens. She also has a grant from the Mark Ravitch/Leon C. Hirsch Center for Minimally Invasive Surgery for \$24,640 to study molecular markers of pre-neoplasia/carcinoma in situ in the respiratory epithelium. Dr Shriver has a pilot grant from the UPCI Lung Cancer Basic Science Program to study genes on chromosome three (\$25,000 total costs) and these funds will also be used to study 3p deletions in the biopsies. All specimens will be stored at no cost in Dr Siegfried's laboratory and DNA, RNA, and protein will be extracted there. The extracted material will be shared among the investigators, with funded investigators receiving priority. Because many of the biomarkers will be measured by PCR reaction, very little material will be required. The biological sample or genetic material may lead, in the future, to new inventions or products. If the research investigators are able to develop new products from the use of the patient's biological sample or genetic material, there are currently no plans to share with the patient any money or other rewards that may result from the development of the new product.

**QUALIFICATIONS OF COLLABORATING INVESTIGATORS:**

*Neil A Christie, MD, FRCS(C)* is an Assistant Professor of Surgery in the School of Medicine at the University of Pittsburgh. He is a thoracic surgeon who also trained in cardiothoracic and general surgery. He has extensive clinical experience in thoracic oncology having completed a two-year fellowship in cardiothoracic surgery at The Cleveland Clinic Foundation.

*James D. Luketich, MD* is an Associate Professor of Surgery and Head of the Section of Thoracic Surgery at the University of Pittsburgh. He has extensive clinical experience in thoracic surgery. He has numerous publications covering many issues in thoracic surgery, however his main interest currently is surgical therapy for esophageal cancer. He is an associate member of the Pittsburgh Cancer Institute and is a clinical investigator with the Eastern Cooperative Oncology Group.

*Peter Ferson, MD* is a Professor of Surgery at the University of Pittsburgh Medical Center in the Section of Thoracic Surgery. Previously he was the Chief of Cardiac Surgery at Montefiore Hospital. Dr. Ferson is currently then Chief of Thoracic Surgery at the VA Medical Center, and Director of Clinical Services.

*Percy Buenaventura*

*Jennifer Ruben Grandis*

*Jill Siegfried, PhD* is an Associate Professor of Pharmacology in the School of Medicine at the University of Pittsburgh. She has extensive research experience in the cell biology of malignant transformation, and is particularly interested in growth factor and growth factor receptor interactions in malignancy, as well as genetic and molecular abnormalities in lung cancer. She has numerous collaborative efforts ongoing in the School of Medicine, as well as other institutions. She is also an associate member of the Pittsburgh Cancer Institute.

*Kelly Kraynick, RN, BSN* is the Clinical Research Coordinator for the Section of Thoracic Surgery. Her clinical experience includes one and a half years working as a staff nurse for neurosurgical and cardiothoracic patients. Her research experience includes one and a half years at the University of Arizona, Sarver Heart Center, working as a Clinical Research Coordinator for the Cardiovascular Protocols and working two years with Diabetic Neuropathy Protocols for the University of Pittsburgh, Department of Neurology.

*Sue Churma, RD CNSD* is the Research Dietitian for the Section of Thoracic Surgery. Her clinical experience includes four years as an inpatient oncology dietitian, and also four years working as inpatient and outpatient dietitian for the Section of Thoracic Surgery. Her research experience includes two years with the Lung and Esophageal Photodynamic Therapy program with the Section of Thoracic Surgery. She has also helped with the LIFE program during its first stages of development.

*Patty Mantia, RN* Thoracic Specialist of University of Pittsburgh Medical Center. Her clinical experience includes sixteen years as an Operating Nurse for UPMC Presbyterian. Her responsibilities include coordinating care of patients and staff for the Thoracic Surgery Division. Her research experience includes the collection and documentation of specimens in the operating room which includes those in the LIFE protocol. She is also responsible for specimen and data collection for other current studies.

## **REFERENCES:**

1. Auerbach O et al: Changes in bronchial epithelium in relation to cigarette smoking and in relation to lung cancer. *N Engl J Med* 265:253-267,1961.
2. Saccomanno *et al.*: Development of Carcinoma of the Lung as Reflected in Exfoliated Cells. *Cancer* 33:256-270,1974.

3. Lam S and Becker H: Future Diagnostic Procedures, in Thoracic Endoscopy, Chest Surgery Clinics of North America (6);363:1996.
4. Thomas *et al.* Cancer Recurrence After Resection: T1N0 Non-Small Cell Lung Cancer. *Ann Thorac Surg* 1990;49:243.
5. Cortese *et al.* Roentgenographically occult Lung Cancer: A Ten Year Experience. *J Thorac Cardiovasc Surg*, 1983;86:373-380.
6. Lam S and Becker H: Future Diagnostic Procedures, in Thoracic Endoscopy, Chest Surgery Clinics of North America (6);364:1996.
7. Pairolero *et al.* Post surgical stage I Bronchogenic Carcinoma: Morbid Implications of Recurrent Disease. *Ann Thorac Surg* 38:331-338,1984.
8. Skillrud *et al.* *Ann Intern Med* 1986; 105:503-7.
9. Hazelrigg *et al.* *Ann Thorac Surg* 1997;64:303-6
10. Pigula *et al.* *Ann Thorac Surg* 1996;61:174-6.
11. IBID.
12. Woolner *et al.* Roentgenographically Occult Lung Cancer: Pathologic Findings and Frequency of Multicentricity During a 10-year Period. *Mayo Proc.*, 59;453-466:1984.
- 13.
14. Woolner *et al.* Pathology of Cancer Detected Cytologically. In: National Cancer Institute Cooperative Early Lung Cancer Group: *An Atlas of Early Lung Cancer* . Tokyo: Igaku Shoin, p.108.
15. Hung J, Lam S *et al.* Autofluorescence of Normal and Malignant Bronchial Tissue *Lasers Surg Med* 1991;11:99-105.
16. Palcic B, Lam S *et al.* Detection and Localization of Early Lung Cancer by Imaging Techniques. *Chest* 1991;99:742-3.
17. IBID
18. Lam S and Palcic B: Fluorescence detection. In: Roth JA *et al* (eds.). Lung Cancer, Blackwell Scientific Publ. 325-338.
19. Pairolero *et al.* Post surgical stage I Bronchogenic Carcinoma: Morbid Implications of Recurrent Disease. *Ann Thorac Surg* 38:331-338,1984.
20. Unpublished data from Protocol-LC 01, A Multi-Centre Study of Fluorescence Bronchoscopy Using LIFE and White-Light Bronchoscopy in Detecting Dysplasia and Carcinoma In Situ, Xillix Technologies Corp., Vancouver, B.C. Canada
21. Lam S: Seminars in Oncology, Vol 21, No 6, Suppl 15,1994:pp15-19.
22. Leong P, Rezai B, Koch W *et al.* Distinguishing Second Primary Tumors From Lung Metastases in Patients With Head and Neck Squamous Cell Carcinoma. *Journal of the National Cancer Institute* 1998; 90:972-77.
23. Leon X, Quer M, Diez S *et al.* Second Neoplasm In Patients With Head And Neck Cancer. *Head and Neck* 1999; 21: 204-10.
24. Cahan WG, Montemayor PB: Multiple Primary Cancers of the Lung, Esophagus, and Other Sites. *Cancer* 177; 40: 1954-60.
25. Jones AS, Morar P, Phillips DE *et al.* Second Primary Tumors in Patients with Head and Neck Squamous Cell Carcinoma. *Cancer* 1995; 75: 1343-52.
26. Cooper JS, Pajak TF, Rubin P *et al.* Second Malignancies in Patients who have Head and Neck Cancer: Incidence, Effect on Survival, Implications based on RTOG experience. *Int J Rad Oncol Biol Phys* 1989; 17: 449-56.

	NULL HYPOTHESIS	
Prevalence of moderate or severe dysplasia or CIS with white light bronchoscopy	20% more lesions found using LIFE-Lung Fluorescence Endoscopy	
	a=0.05	a=0.01
0.10	0.81	0.61
0.20	0.98	0.93

**Table 1**

Estimated Power for Study Design Enrolling 250 Patients Under the Alternative Hypothesis that 50% More Disease is Identified Using LIFE Fluorescence Endoscopy.

## APPENDIX C

### MATLAB MIE LIBRARY CODE

```
%BEGIN Original source file build_library6.m
%This function builds a disk-based library of calculated Mie scattering coefficients
%for an ideal sphere of the given diameter(s) with a given refractive index
%and located in the given media.
%The function name and parameters has been preserved so that
%they are consistent with the original text in
%Bohren & Huffman, "Absorption and Scattering of Light by Small Particles",
%Wiley Interscience, 1983
%It is intended for other functions to load the Mie curves as needed from the
%disk.
```

```
function build_library6(ref_med, ref_bead, diameter_list);
```

```
%A usage example....
```

```
    if (nargin==0)
        ref_med = 1.33; %water
        ref_bead = 1.59; %polystyrene
        diameter_list = [1.025 0.505 0.495]; %um;
    end
    starttime=now;
    for d=diameter_list;
        if (exist(curvelib6path(ref_med,ref_bead,d))~=2)
            save_callbm(d,ref_med,ref_bead);
        else
            disp(sprintf('Skipping %dmm...',d));
        end
    end
    disp('Done. ');
    disp('Starting Time');
    disp(datestr(starttime,0));
    disp('Ending Time');
```

```

disp(datestr(now,0));

function save_callbm(diameter,ref_med, ref_bead);
    nang=901;
%radii = 1:0.5:20;
    radii = [diameter]/2; %diameters
    if (1==0)
        waves = (380:1:1500)*0.001;
    else
        waves = (380:1:690)*0.001;
    end
%Note: Thetas are specified in degrees
%thetas = [165:180];
%distance = 7;
%dtheta_i = atan(0.4/distance)
%dtheta_r = atan(0.175/distance);
    dtheta = 90/(nang-1);% = 0.1
%dtheta1 = ceil(dtheta_i/dtheta)
%dtheta2 = ceil(dtheta_r/dtheta)
%thetas = 165:dtheta:180;
    starttheta=1;
%disp('Precomputing Sphere Scattering');
%disp('For thetas');
%disp(thetas);
%disp('For lambdas');
%disp(waves);
%disp('For radii');
%disp(radii);
    callbm_results.radii=radii;
    callbm_results.dradius=0.1;
    callbm_results.waves=waves;
    callbm_results.dwave = waves(2)-waves(1);
    callbm_results.units = 'um';
    callbm_results.dtheta=dtheta;
%callbm_results.distance=distance;
    callbm_results.thetas = starttheta:dtheta:180;
    rslt = [];
%r_checkpoint =
[radii(1),radii(floor(0.25*length(radii))),radii(floor(0.5*length(radii))),radii(floor(0.75*length(radii)))]
    r_checkpoint = [0];
    disp(sprintf('Building %s',curvelib6path(ref_med,ref_bead,diameter)));
    for r=length(radii):-1:1
        rad=radii(r);
        ttl = sprintf('Radius=%6.3fnm',rad);
% set(FH,'name',sprintf('Wave=%6.3fnm',wav*1000));

```

```

disp(sprintf('----- Radius=%6.3f----- (begun at %s)',rad,datestr(now,0));
gall=[];
for w=length(waves):-1:1
    wav = waves(w);
    disp(sprintf('----- Radius=%6.3f, Wave=%6.3f -----',rad,wav));
% [gy,gx]=makeGaussian(rad,ss);
%     gy = [1 1 1];
%     gx=[rad-1 rad rad+1];
%     glen = length(gx);
%     [ts1,ts2,tres]=doParams(wav,rad,nang);
%     temp_res=[ts1,ts2,tres];
%     gall(w,.,:)=temp_res((floor(starttheta/dtheta)):end,:);
end
% subplot(2,1,r);
% plotResults(ttl,rslt,waves,thetas);
%return;
%     rslt(r,.,:)=gall(.,.,:);
% if (sum(r==r_checkpoint)>0)
%     callbm_results.res=rslt;
%     disp(sprintf('Saving checkpoint at %%%d...',floor(100*(r/length(radii))));
%     save 'callbm_JQE_checkpoint' callbm_results
%     callbm_results = rmfield(callbm_results,'res');
% end
end
%Note that data is in the format (radius,wavelength,,:)
%(:,1) is s1, (:,2) is s2, (:,3) is theta, etc.
disp('Generation complete. Saving...');
callbm_results.res=rslt;
save (sprintf('curvelib\%s',curvelib6path(ref_med,ref_bead,diameter)),'callbm_results');

function pl=printResults(ang,s1,s2,res);
len = length(s1)
disp(sprintf('Ang'));
%th=floor(res(:,1));
pl=zeros([length(ang),3]);
p=1;
for k=1:len,
    if (find(ang==floor(res(k,1))))
        pl(p,1)=res(k,1);
        pl(p,2)=s1(k);
        pl(p,3)=s2(k);
        p=p+1;
        disp(sprintf('%6.2f%13.6f%16.3f',res(k,1),s1(k),s2(k)));
    end
end
end

```

```

function [s1,s2,res]=doParams(wavel,rad,nang);
    refmed = 1.33;
    refbead = 1.59;
    %refrel = complex(1.59,0)/refmed;
    refrel = complex(refbead,0)/refmed;
    %refrel=computeRefRel(wavel*1000);
    %[refbead,refmed,refrel]=computeRefRelPSB3(wavel);
    %disp(sprintf('RefMed=%8.4f, refre=%f, refim=%f,refmed,real(refrel),imag(refrel)));
    %rad=0.525;
    %wavel=0.6328;
    x=2*3.14159265*rad*refmed/wavel;
    %x=2*3.14159265*rad/wavel;
    %disp(sprintf('Sphere Radius=%7.3f, wavelength=%7.4f, size param=%8.3f,rad,wavel,x));
    dang=1.570796327/(nang-1);
    [s1,s2,qext,q sca,qback]=bhmie(x,refrel,nang);
    %disp(sprintf('Qsca=%13.6f, Qext=%13.6f. Qback=%13.6f,q sca,qext,qback));
    res=[];
    return;
    s11nor=0.5*(abs(s2(1))^2+abs(s1(1))^2);
    %disp(sprintf('Ang'));
    len = (2*nang-1);
    res=double(zeros([len 5]));
    for j=1:len,
        t1 = abs(s2(j))^2;
        t2 = abs(s1(j))^2;
        s11=0.5*(t1 + t2);
        s12=0.5*(t1 - t2);
        pol=-s12/s11;
        t3 =s2(j)*conj(s1(j));
        s33=real(t3)/s11;
        s34=imag(t3)/s11;
        s11=s11/s11nor;
        ang=dang*(j-1)*57.2958;
        res(j,:)= [ang s11 pol s33 s34];
    % disp(sprintf('%6.2f%13.6f%13.6f%13.6f%13.6f',ang,s11,pol,s33,s34));
    end

```

```

function [iSphere,iMedium,refrel]=computeRefRelPSB3(wavel);
    %im = [1.3231; 0; 3.3e-3; 0; -3.2e-5]; %Mcneil
    im = [1.31279; 15.762e-3; -4.382e-3; 1.1455e-3;0]; %Quan & Fry
    is = [1.5663; 0; 7.85e-3; 0; 3.34e-4]; %From Duke Scientific
    %is = [1.5725; 0; 3.108-3; 0; 3.34e-4]; %From paper
    wl = [1,1/wavel,1/(wavel.^2),1/(wavel.^3),1/(wavel.^4)];
    iSphere = wl * is;
    iMedium = wl * im;
    refrel = iSphere/iMedium;

```

```

function [iSphere,iMedium,refrel]=computeRefRelPSB(wavel);
    im = [1.3236; 0; 3.3418e-3; 0; -3.45e-5];
%is = [1.5663; 0; 7.85e-3; 0; 3.34e-4];
    is = [1.5725; 0; 3.108-3; 0; 3.34e-4];
    wl = [1,1/wavel,1/wavel^2,1/wavel^3,1/wavel^4];
    iSphere = wl * is;
    iMedium = wl * im;
    refrel = iSphere/iMedium;

```

```

function refrel=computeRefRel(wavel);
    im = [1.413; -0.0002968; 3.679e-7; -1.614e-10];
    is = [1.896; -0.001185; 1.544e-6; -7.022e-10];
    wl = [1,wavel,wavel^2,wavel^3];
    iSphere = wl * is;
    iMedium = wl * im;
    refrel = iSphere/iMedium;
%END Original source file build_library6.m
%BEGIN Original source file bhmie.m
%This code was adapted from the original FORTRAN code in
%Bohren & Huffman, "Absorption and Scattering of Light by Small Particles",
%The function name and parameters has been preserved so that
%they are consistent with the original text.

```

```

function [s1,s2,qext,qscat,qback]=bhmie(x,refrel,nang);
    y=x*refrel;
    xstop=x+(4*x^0.3333)+2;
    nstop=xstop;
    ymod=abs(y);
    nmxfloor=floor(max([xstop ymod]))+15;
    dang = 1.570796327/(nang-1);
    for j=1:nang,
        theta(j)=(j-1)*dang;
    end
    amu=cos(theta);
    d(nmxfloor)=0+0i;
    for n=1:(nmxfloor-1);
        rn=nmxfloor-n+1;
        t4=rn/y;
        d(nmxfloor-n)=t4-(1/(d(rn)+t4));
    end
    pi0=zeros([nang 1]);
    pi1=ones([nang 1]);
    s1=complex(zeros([(2*nang-1) 1]));
    s2 = s1;
    psi0=cos(x);

```

```

psi1=sin(x);
chi0=-sin(x);
chi1=cos(x);
xi0=complex(psi0,-chi0);
xi1=complex(psi1,-chi1);
qsca=0.0;
n=1;
P=-1;
for n=1:nstop;
    fn=(2*n+1)/(n*(n+1));
    psi=(2*n-1)*psi1/x-psi0;
    chi = (2*n-1)*chi1/x-chi0;
    xi=complex(psi,-chi);
    t5=d(n)/refrel+n/x;
    an = (t5*psi - psi1)/(t5*xi - xi1);
    t6=d(n)*refrel+n/x;
    bn = (t6*psi - psi1)/(t6*xi - xi1);
%   qsca=qsca+(2*n+1)*( abs(an)^2+abs(bn)^2);
    qsca=qsca+(2*n+1)* ( an *conj(an))+ (bn *conj(bn)));
%angles 0-90 deg
    for j=1:nang;
        pi_(j)=pi1(j);
        tau(j)=n*amu(j)*pi_(j) - (n+1)*pi0(j);
        s1(j)=s1(j)+fn*(an*pi_(j)+bn*tau(j));
        s2(j)=s2(j)+fn*(an*tau(j)+bn*pi_(j));
    end;
%angles 90+
    P=-P;
    for j=1:(nang-1);
        jj=2*nang-j;
        s1(jj)=s1(jj)+fn*P*(an*pi_(j)-bn*tau(j));
        s2(jj)=s2(jj)+fn*P*(bn*pi_(j)-an*tau(j));
    end
    psi0=psi1;
    psi1=psi;
    chi0=chi1;
    chi1=chi;
    xi1=complex(psi1,-chi1);
%update
%   figure(99);
%   clf;
%   plot(1:length(s1),s1 .* conj(s1));
%   title(sprintf('Pass #'%d',n));
%   pause;
%computer pi_n for next value of n
    for j=1:nang,

```

```

        pi1(j) = ( (2*n+1)*amu(j)*pi_(j)-(n+1)*pi0(j) )/n;
        pi0(j)=pi_(j);
    end
end
qsca=(2/(x*x))*qsca;
qext=(4/(x*x))*real(s1(1));
%qback=(4/(x*x))*s1(2*nang-1)*conj(s1(2*nang-1));
qback=((abs(s1(2*nang-1))/x)^2)/pi;
%END Original source file bhmie.m
%BEGIN Original source file curvelib6path.m
%This function is an abstracted version of the library name so that other
%matlab functions can easily figure out what the Mie curve's filename is.

```

```

function path=curvelib6path(ref_med,ref_bead,d);
    path=sprintf('curve-library6-%d-%d-
d%04dmm.mat',floor(ref_med*100),floor(ref_bead*100),floor(d*1000));
%END Original source file curvelib6path.m

```

## BIBLIOGRAPHY

- A' Amar, O M; Ley, R D; Bigio, I J; "Comparison between ultraviolet-visible and near infrared elastic scattering spectroscopy of chemically induced melanomas in an animal model" Journal of Biomedical Optics 9 no. 6 (2004): 1320-1326
- Alfano, R R; Yang, Y; "Stokes Shift Emission Spectroscopy of Human Tissues and Key Biomolecules" IEEE J. of Selected Topics in QE 9 (2003): 148
- Amelink, A; Bard, M P L; Burgers, S A; Sterenberg, H J C M; "Single-scattering spectroscopy for the endoscopic analysis of particle size in superficial layers of turbid media" Applied Optics 42 no. 19 (2003): 4095-4101
- Andersson-Engels, S; Canti, G; Cubeddu, R; Eker, C; Klinteberg, C A; Pifferi, A; Svanberg, K; Svanberg, S; Taroni, P; Valentini, G; Wang, I; "Preliminary Evaluation of Two Fluorescence Imaging Methods for the Detection and the Delineation of Basal Cell Carcinomas of the Skin." Lasers in Surgery and Medicine 26 (2000): 76-82
- Arendt, J T; Levin, H S; Klein, EA; Manoharan, R; Feld, M S; Cothren, R M; "Investigation of Early Cancerous Changes in Bladder Tissue By Autofluorescence." Engineering in Medicine and Biology Society, Proceedings of the 19<sup>th</sup> International Conference (October 30, 1997): 2290-2293
- Backman, V; Gopal, V; Kalashnikov, M; Badizadegan, K; Gurjar, R; Wax, A; Georgakoudi, I; Mueller, M; Boone, C W; Dasari, R R; Feld, M S; "Measuring Cellular Structure at Submicrometer Scale with Light Scattering Spectroscopy." IEEE Journal on Selected Topics in Quantum Electronics 7 no. 6 (November/December 2001)
- Backman, V; Gurjar, R; Badizadegan, K; Itzkan, I; Dasari, R R; Perelman, L T; Feld, M S; "Polarized light scattering Spectroscopy for Quantitative Measurement of Epithelial Cellular Structures *In Situ*." IEEE Journal of Selected Topics in Quantum Electronics 5 no. 4 (1999): 1019-1026
- Betz, C S; Mehlmann, M; Rick, K; Stepp, H; Grevers, G; Baumgartner, R; Leunig, A; "Autofluorescence Imaging and Spectroscopy of Normal and Malignant Mucosa in

- Patients with Head and Neck Cancer.” Lasers in Surgery and Medicine 25 (1999): 323–334
- Bigio, I J; Brown, S G; Kelly, C; Lakhani, S; Pickard, D; Ripley, P; Rose, I; Saunders, C; “Diagnosis of breast cancers using elastic-scattering spectroscopy: preliminary clinical results” Journal of Biomedical Optics 5 no. 2 (2000): 221-228
- Bigio, I J; Mourant, J R; “Ultraviolet and Visible Spectroscopies for Tissue Diagnostics: Fluorescence Spectroscopy and Elastic-Scattering Spectroscopy.” Physics in Medicine and Biology 42 (1997): 803-814
- Bohren, C F; Huffman, D R; “Absorption and Scattering of Light by Small Particles.” Wiley-Interscience (1983)
- Brereton, R G; “Chemometrics: Data Analysis for the Laboratory and Chemical Plant” John Wiley and Sons, Ltd (1999)
- Brewer, M; Utzinger, U; Silva, E; Gershenson, D; Blast, R; Follen, M; Richards-Kortum, R; “Fluorescence Spectroscopy for In vivo Characterization of Ovarian Tissue.” Lasers in Surgery and Medicine 29 (2001): 128–135
- Brookner, C K; Utzinger, U; Staerkel, G; Richards-Kortum, R; and Follen-Mitchell, M; “Cervical Fluorescence of Normal Women” Lasers in Surgery and Medicine 24 (1999): 29–37
- Brooks, J L; Sucheta, A; Einarsdottir, O; “Light-Induced Spectral Changes in Fully Oxidized Cytochrome *c* Oxidase in the Presence of Oxygen.” Biochemistry 36 (1997): 6336-6342
- Campbell, N A; “Biology (3<sup>rd</sup> edition)” The Benjamin/Cummings Publication Company, Inc (1993): 121-145, 515-519
- Campagnola, P J; Loew, L M; “Second-harmonic imaging microscopy for visualizing biomolecular arrays in cells, tissues, and organisms” Nature Biotechnology 21 no 11 (Nov 2003): 1356-1360
- Chwirot, B W; Chwirot, S; Jedrzejczyk, W; Jackowski, M; Raczynska, A M; Winczakiewicz, J; Dobber, J; “Ultraviolet Laser-induced Fluorescence of Human Stomach Tissues: Detection of Cancer Tissues by Imaging Techniques”, Lasers in Surgery and Medicine 21 (1997): 149-158

- Coghlan, L; Utzinger, U; Richards-Kortum, R; Brookner, C; Follen, M; “Fluorescence Spectroscopy of Epithelial Tissue Throughout the Dysplasia-Carcinoma Sequence in an Animal Model: Spectroscopic Changes Precede Morphologic Changes.” Lasers in Surgery and Medicine 29 (2001): 1–10
- Colasanti, A; Kisslinger, A; Fabbrocini, G, Liuzzi, R; Quarto, M; Riccio, P; Roberti, G; Villani, F; “MS-2 Fibrosarcoma Characterization by Laser Induced Autofluorescence.” Lasers in Surgery and Medicine 26 (2001): 441–448
- Dark, M L; Perelman, L T; Itzkan, I; Schaffer, J L; Feld, M S; “Physical properties of hydrated tissue determined by surface interferometry of laser-induced thermoelastic deformation.” Physics in Medicine and Biology 45 (2000): 529-539
- Damjanov, I; Linder, J; “Anderson’s Pathology (10<sup>th</sup> Edition)” Mosby-Year Book, Inc. (1996), pp 1471-1472, 1541-1548
- Gans, P; “Data Fitting In The Chemical Sciences By The Method Of Least Squares” John Wiley and Sons, Ltd (1992)
- Georgakoudi, I; Jacobson, B C; Van Dam, J; Backman, V; Wallace, M B; Mueller, M; Zhang, Q; Badizadegan, K; Sun, D; Thomas, G A; Perelman, L T; Feld, M S; “Fluorescence, Reflectance, and Light-Scattering Spectroscopy for Evaluating Dysplasia in Patients With Barrett’s Esophagus.” Gastroenterology 120 (2001): 1620-1629
- Georgakoudi, I; Sheets, E; Muller, M G; Backman, V; Crum, C P; Badizadegan, K; Dasari, R R; Feld, M S; “Trimodal spectroscopy for the detection and characterization of cervical precancers in vivo” American Journal of Obstetrics and Gynecology 186 no. 3 (2002): 374-382
- Giuffra, E; Zucchelli, G; Sandona, D; Croce, R; Cugini, D; Garlaschi, F M; Bassi, R; Jennings, R; “Analysis of Some Optical Properties of a Native and Reconstituted Photosystem II Antenna Complex, CP29: Pigment Binding Sites Can Be Occupied by Chlorophyll *a* or Chlorophyll *b* and Determine Spectral Forms.” Biochemistry 36 (1997): 12984-12993
- Giuliano, K A; Post, P L; Hahn, K M; Taylor, D L; “Fluorescent protein biosensors: measurement of molecular dynamics in living cells” Annu Rev Biophysics Biomol Struct 24 (1995): 405-434

- Hielscher, A H; Mourant, J R; Bigio, I J; "Biomedical Diagnostics with Elastic Light Scattering in Cell Suspensions and Tissues." Engineering in Medicine and Biology Society, Proceedings of the 19<sup>th</sup> International Conference (October 30, 1997): 2716-2721
- Hielscher, A H; Mourant, J R; Bigio, I J; "Influence of particle size and concentration on the diffuse backscattering of polarized light from tissue phantoms and biological cell suspensions" Applied Optics 36 no. 1 (1997): 125-135
- Hellwig, P; Scheide, D; Bungert, S; Mantele, W; Freidrich, T; "FT-IR Spectroscopic Characterization of NADH:Ubiquinone Oxidoreductase (Complex I) from *Escherichia coli*: Oxidation of FeS Cluster N<sub>2</sub> is Coupled with the Protonation of an Aspartate or Glutamate Side Chain." Biochemistry 39 (2000): 10884-10891
- Hole, J W; "Essentials of Human Anatomy and Physiology, 3rd Ed" William C. Brown Publishers (1989)
- Huang, Z; McWilliams, A; Lui, H; McLean, D I; Lam, S; Zeng, H; "Near-infrared Raman spectroscopy for optical diagnosis of lung cancer" Int J Cancer 107 no 6 (Dec 20, 2003): 1047-52
- Igarashi, M; Gono, K; Obi, T; Yamaguchi, M; Ohyama, N; "Monte Carlo Simulation of reflected Spectra Derived from Tissue Phantom with Double-Peak Particle Size Distribution" Optical Review 11 no. 2 (2004): 61-67
- Johnson, K S; Chicken, D W; Pickard, D C O; Lee, A; Briggs, G; Falzon, M; Bigio, I J; Keshtgar, M R; Brown, S; "Elastic scattering spectroscopy for intraoperative determination of sentinel lymph node status in the breast" Journal of Biomedical Optics 9 no. 6 (2004): 1122-1128
- Kneipp, K; Kneipp, H; Manoharan, R; Itzkan, I; Dasari, R R; Feld, M S; "Surface-enhanced Raman scattering (SERS) – a new tool for single molecule detection and identification." Bioimaging 6 (1998): 104-110
- Kricka, L J; Stanley, P E; "Assays using digital fluorescence: 1985-1998." Luminescence 14 (1999): 272-279
- Kwong, D L W; Nicholls, J; Wei, W I; Chua, D T T; Sham, J S T; Yuen, P W; Cheng, A C K; Yau, C C; Kwong, P W K; Choy, D T K; "Correlation of Endoscopic and Histologic Findings Before and After Treatment For Nasopharyngeal Carcinoma." Head & Neck (January 2001)

- Kolarova, H; Ditrichova, D; Wagner, J; "Penetration of the Laser Light Into the Skin In Vitro." Lasers in Surgery and Medicine 24 (1999): 231–235
- LaCroix, J; Doeberitz, M V K; "Technical Aspects of Minimal Residual Disease Detection in Carcinoma Patients." Seminars in Surgical Oncology 20 (2001): 252-264
- Li, C; Guo, B; Bernabeu, C; Kumar, S; "Angiogenesis in Breast Cancer: The Role of Transforming Growth Factor b and CD105." Microscopy Research And Technique 52 (2001): 437–449
- Massart, D L; Vandeginste, B G M; Buydens, L M C; Jong, S D; Lewi, P J; Smeyers-Verbeke, J; "Handbook of Chemometrics and Qualimetrics, Parts A & B" Elsevier Science B.V. (1997)
- Mie, G; "Beitrage zur Optik truber Meiden speziell kolloidaler Metallosungen" Ann Phys. 25 (1908): 377-445
- Mirabal, Y N; Chang, S K; Atkinson, E N; Malpica, A; Follen, M; Richards-Kortum, R; "Reflectance spectroscopy for *in vivo* detection of cervical precancer" Journal of Biomedical Optics 7 no. 4 (2002): 587-594
- Mourant, J R; Bigio, I J; Boyer, J; Conn, R L; Johnson, T; Shimada, T; "Spectroscopic Diagnosis of Bladder Cancer With Elastic Light Scattering." Lasers in Surgery and Medicine 17 (1995): 350-357
- Mourant, J R; Johnson, T M; Los, G; Bigio, I J; "Non-invasive measurement of chemotherapy drug concentrations in tissue: preliminary demonstrations of *in vivo* measurements." Physics in Medicine and Biology 44 (1999): 1397-1417
- North, J A; Rein, D; Tappel, A L; "Multicomponent Analysis of Heme Protein Spectra in Biological Materials." Analytical Biochemistry 233 (1996): 115–123
- Palmer, G M; Marshek, C L; Vrotsos, K M; Ramanujam, N; "Optimal Methods for Fluorescence and Diffuse Reflectance Measurements of Tissue Biopsy Samples.", Lasers in Surgery and Medicine 30 (2002): 191–200
- Perelman, L T; Backman, V; "Light Scattering Spectroscopy of Epithelial Tissues: Principles and Applications" from "Handbook of Optical Diagnostics" SPIE Press (2002)

- Periasamy, A; Skoglund, P; Noakes, C; Keller, R; “An Evaluation of Two-Photon Excitation Versus Confocal and Digital Deconvolution Fluorescence Microscopy Imaging in *Xenopus* Morphogenesis.”, Microscopy Research And Technique 47 (2001): 172–181
- Prahl, S; “Tabulated Molar Extinction Coefficient for Hemoglobin in Water” <http://omlc.ogi.edu/spectra/hemoglobin/summary.html>
- Qu, J Y; Qing, P; Huang, Z; Kwong, D; Sham, J; Lee, S L; Kuen, W; Wie, W; “Preliminary Study of *In vivo* Autofluorescence of Nasopharyngeal Carcinoma and Normal Tissue.” Lasers in Surgery and Medicine 26 (2000): 432–440
- Rava, R P; Richards-Kortum, R; Petras, R E; Fitzmaurice; Feld, M S; “Laser Induced Fluorescence of Human Colon Tissue.” IEEE Engineering in Medicine and Biology Society 12 no. 3 (1990): 1152
- Seibel, E; Smithwick, Q Y J; “Unique Features of Optical Scanning, Single Fiber Endoscopy” Lasers in Surgery and Medicine 30 (2002): 177-183
- Shibuya, K; Hoshino, H; Chiyo, M; Iyoda, A; Yoshida, S; Sekine, Y; Iizasa, T; Saitoh, Y; Baba, M; Hiroshima, K; Ohwada, H; Fujisawa, T; “High magnification bronchovideoscopy combined with narrow band imaging could detect capillary loops of angiogenic squamous dysplasia in heavy smokers at high risk for lung cancer” Thorax 58 (2003): 989-995
- Sroka, R; Schaffer, M; Fuchs, C; Pongratz, T; Schrader-Reichard, U; Busch, M; Schaffer, P M; Duhmke, E; Baumgartner, R; “Effects on the Mitosis of Normal and Tumor Cells Induced by Light Treatment of Different Wavelengths.” Lasers in Surgery and Medicine 25 (1999): 253-271.
- Szundi, I; Liao, G L; Einarsdottir, O; “Near-Infrared Time-Resolved Optical Absorption Studies of the Reaction of Fully Reduced Cytochrome *c* Oxidase with Dioxygen.” Biochemistry 40 (2001): 2332-2339
- Taatjes, D J; Gaudiano, G; Resing, K; Koch, T H; “Redox Pathway Leading to the Alkylation of DNA by the Anthracycline, Antitumor Drugs Adriamycin and Daunomycin.” Journal of Medicinal Chemistry 40 (1997): 1276-1286
- Tang, J; Zeng, F; Savage, H; Ho, P P; Alfano, R R; “Laser Irradiative Tissue Probed In Situ by Collagen 380-nm Fluorescence Imaging.” Lasers in Surgery and Medicine 27 (2000): 158–164

- Thueller, P; Charvet, I; Bevilacqua, F; Ghislain, M S; Ory, G; Marquet, P; Meda, P; Vermeulen, B; Depeursinge, C; “*In vivo* endoscopic tissue diagnostics based on spectroscopic absorption, scattering, and phase function properties” Journal of Biomedical Optics 8 no. 3 (2003): 495-503
- Uttinger, U; Brewer, M; Silva, E; Gershenson, D; Blast, R; Follen, M; Richards-Kortum, R; “Reflectance Spectroscopy for *In vivo* Characterization of Ovarian Tissue.” Lasers in Surgery and Medicine 28 (2001): 56–66
- Uttinger, U; Richards-Kortum, R R; “Fiber optic probes for biomedical optical spectroscopy” Journal of Biomedical Optics 8 no. 1 (2003): 121-147
- Vaidyanathan, V V; Rastegar, S; Fossum, T W; Flores, P; van der Breggen, E W; Egger, N; Jacques, S L; Motamedi, W; “A Study of Aminolevulinic Acid–Induced Protoporphyrin IX Fluorescence Kinetics in the Canine Oral Cavity.” Lasers in Surgery and Medicine 26 (2000): 405–414
- Van De Hulst, H C; “Light Scattering by Small Particles” John Wiley & Sons, Inc. (1957)
- Vargas, G; Chan, K F; Thomsen, S L; Welch, A J; “Use of Osmotically Active Agents to Alter Optical Properties of Tissue: Effects on the Detected Fluorescence Signal Measured Through Skin.” Lasers in Surgery and Medicine, 29 (2001): 213–220
- Wax, A; Yang, C; Backman, V; Kalashnikov, M; Dasari, R R; Feld, M S; “Determination of particle size by using the angular distribution of backscattered light as measured with low-coherence interferometry” Journal of the Optical Society of America, 19 no.5 (2002): 737-744
- Welch, A J; Gardner, C; Richards-Kortum, R; Chan, E; Criswell, G; Pfefer, J; Warren, S; “Propagation of Fluorescent Light.” Lasers in Surgery and Medicine 21 (1997): 166–178
- Zipfel, W R; Williams, R M; Webb, W W; “Nonlinear magic: multiphoton microscopy in the biosciences” Nature Biotechnology 21 no 11 (Nov 2003): 1369-1377